

AD-A174 683

DENSE-SPRAY STRUCTURE AND PHENOMENA(U) MICHIGAN UNIV

1/1

ANN ARBOR DEPT OF AEROSPACE ENGINEERING

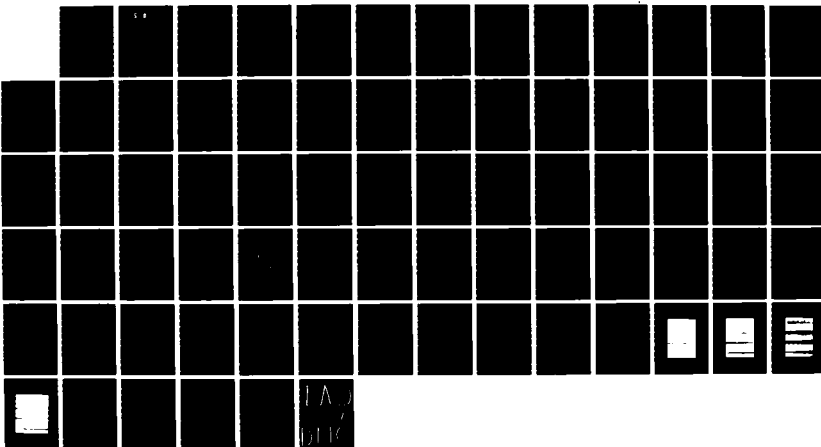
R N PARTHASARATHY ET AL. 15 AUG 86 AFOSR-TR-86-1071

UNCLASSIFIED

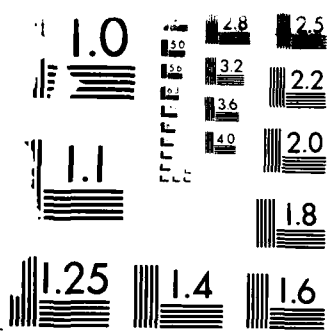
AFOSR-85-0244

F/G 21/2

NL



1 A
014



© 1984 RICOH CO., LTD. (RICOH)

2
classified

CLASSIFICATION OF THIS PAGE

AD-A174 683

REPORT DOCUMENTATION PAGE

Unclassified		1b. RESTRICTIVE MARKINGS None	
2a. SECURITY CLASSIFICATION AUTHORITY ELECTE		3. DISTRIBUTION/AVAILABILITY OF REPORT Distribution unlimited; approved for public release	
2b. DECLASSIFICATION / DOWNGRADING SCHEDULE SCHEDULE 02 1986		4. PERFORMING ORGANIZATION REPORT NUMBER(S) D.	
		5. MONITORING ORGANIZATION REPORT NUMBER(S) AFOSR-TR. 86-1071	
6a. NAME OF PERFORMING ORGANIZATION Department of Aerospace Eng. The University of Michigan		6b. OFFICE SYMBOL (If applicable)	
6c. ADDRESS (City, State, and ZIP Code) 217 Aerospace Engineering Building Ann Arbor, MI 48109-2140		7a. NAME OF MONITORING ORGANIZATION Air Force Office of Scientific Research	
7b. ADDRESS (City, State, and ZIP Code) Building 410 Bolling AFB, DC 20332-6448		8a. NAME OF FUNDING/SPONSORING ORGANIZATION Air Force Office of Sci. Res.	
		8b. OFFICE SYMBOL (If applicable) AFOSR/NA	
8c. ADDRESS (City, State, and ZIP Code) Building 410 Bolling AFB, DC 20332-6448		9. PROCUREMENT INSTRUMENT IDENTIFICATION NUMBER AFOSR-85-0244	
		10. SOURCE OF FUNDING NUMBERS PROGRAM ELEMENT NO. 61102 F PROJECT NO. 2308 TASK NO. A2 WORK UNIT ACCESSION NO.	
11. TITLE (Include Security Classification) Dense-Spray Structure and Phenomena (U)			
12. PERSONAL AUTHOR(S) R.N. Parthasarathy, A. Sagar and G.M. Faeth			
13a. TYPE OF REPORT Annual		13b. TIME COVERED FROM 15 Jul 85 TO 14 Jul 86	
		14. DATE OF REPORT (Year, Month, Day) 15 Aug 1986	
15. PAGE COUNT 65			
16. SUPPLEMENTARY NOTATION			
17. COSATI CODES		18. SUBJECT TERMS (Continue on reverse if necessary and identify by block number) dense sprays atomization turbulent dispersion particle-laden jets multiphase flow	
FIELD GROUP SUB-GROUP			
21	01		
21	02		
19. ABSTRACT (Continue on reverse if necessary and identify by block number) This report describes progress during the first year of a three year theoretical and experimental study of dense sprays. The work was divided into two phases, as follows: (1) an investigation of particle-laden water jets; and (2) an investigation of large-scale liquid jets in the atomization regime. The particle-laden jet experiments involved nearly monodisperse glass particles in water, injected into still water, to simulate phase density ratios typical of high-pressure sprays. Preliminary findings suggest that the locally homogeneous flow approximation, where interphase transport rates are assumed to be infinitely fast, is more successful for this flow than was observed during earlier work with phase density ratios farther from unity. This is encouraging for application of relatively simple locally homogeneous flow analysis to high-pressure combustion processes encountered in power and propulsion systems. Measurements of the atomization of large-scale liquid jets show the presence of an all-liquid core which extends an appreciable distance from the injector (ca. 200 injector			
20. DISTRIBUTION AVAILABILITY OF ABSTRACT <input checked="" type="checkbox"/> UNCLASSIFIED/UNLIMITED <input type="checkbox"/> SAME AS RPT <input type="checkbox"/> DTIC USERS		21. ABSTRACT SECURITY CLASSIFICATION Unclassified	
22a. NAME OF RESPONSIBLE INDIVIDUAL Julian M. Tishkoff		22b. TELEPHONE (Include Area Code) 202-767-4987	
		22c. OFFICE SYMBOL AFOSR/NA	

DD FORM 1473, 84 MAR

83 APR edition may be used until exhausted.

All other editions are obsolete.

SECURITY CLASSIFICATION OF THIS PAGE

Unclassified

DTIC FILE COPY

86 11 25 380

diameters) at atmospheric pressure conditions. The drop containing shear layer adjacent to this core exhibits some properties of a locally homogeneous flow, however, large drops were also formed at the liquid surface which probably depart from this behavior. Measurements of liquid volume fraction suggest relatively slow rates of turbulent mixing for the low pressure conditions of present experiments.

Table of Contents

	Page
Abstract.....	i
List of Tables.....	iv
List of Figures.....	v
Nomenclature.....	vii
1. Introduction.....	1
2. Particle-Laden Jets	2
2.1 Introduction.....	2
2.2 Experimental Methods.....	4
2.2.1 Apparatus.....	4
2.2.2 Instrumentation.....	4
2.2.3 Test Conditions.....	6
2.3 Theoretical Methods	6
2.3.1 Description of Analysis.....	6
2.3.2 Locally Homogeneous Flow Analysis.....	7
2.3.3 Interphase Transport.....	10
2.3.4 Deterministic Separated Flow Analysis.....	12
2.3.5 Stochastic Separated Flow Analysis.....	12
2.3.6 Initial Conditions.....	13
2.4 Results and Discussion	14
2.4.1 Properties Along Axis.....	14
2.4.2 Continuous-Phase Velocities.....	14
2.4.3 Dispersed-Phase Velocities.....	15
2.5 Summary	16
3. Dense Sprays	17
3.1 Introduction	17
3.2 Experimental Methods	20
3.2.1 Apparatus.....	20
3.2.2 Instrumentation.....	21
3.2.3 Test Conditions.....	23
3.3 Theoretical Methods	23
3.3.1 Description of Analysis.....	23
3.3.2 LHF Formulation.....	24
3.3.3 Initial Conditions.....	25
3.4 Results and Discussion	25
3.4.1 Flow Visualization.....	25
3.4.2 Liquid Volume Fraction Distributions.....	27
3.5 Summary.....	29
4. Summary of Investigation	30
4.1 Articles and Papers	30
4.2 Participants	30
4.3 Oral Presentations	30
References.....	31

List of Tables

Table	Page
1. Summary of Particle-Laden Jet Test Conditions	6
2. Source Terms and Empirical Constants in the Continuous-Phase Governing Equations	9
3. Liquid Jet Breakup Criteria	17
4. Summary of Dense-Spray Test Conditions	23
5. Relationship between Mixture Fraction and Liquid Volume Fraction	28

Accession For		
NTIS	CRA&I	<input checked="" type="checkbox"/>
DTIC	TAB	<input type="checkbox"/>
Unannounced		<input type="checkbox"/>
Justification		
By _____		
Distribution / _____		
Availability Codes		
Dist	Avail and/or Special	
A-1		



86 11 25 380

List of Figures

Figure	Page
1. Sketch of particle-laden jet apparatus.....	35
2. Sketch of phase-discriminating LDA.....	36
3. Sketch of the particle-flux measuring system.....	37
4. Mean liquid-phase velocities along axis.....	38
5. Mean particle-phase velocities along axis.....	39
6. Mean and turbulent properties for the single-phase jet at $x/d = 16$	40
7. Mean and turbulent properties for the single-phase jet at $x/d = 24$	41
8. Mean and turbulent properties for the single-phase jet at $x/d = 40$	42
9. Mean and turbulent liquid-phase properties for the case I jet at $x/d = 16$	43
10. Mean and turbulent liquid-phase properties for the case I jet at $x/d = 24$	44
11. Mean and turbulent liquid-phase properties for the case I jet at $x/d = 40$	45
12. Mean and turbulent liquid-phase properties for the case II jet at $x/d = 16$	46
13. Mean and turbulent liquid-phase properties for the case II jet at $x/d = 24$	47
14. Mean and turbulent liquid-phase properties for the case II jet at $x/d = 40$	48
15. Mean and turbulent particle-phase properties for the case I jet at $x/d = 16$	49
16. Mean and turbulent particle-phase properties for the case I jet at $x/d = 24$	50
17. Mean and turbulent particle-phase properties for the case I jet at $x/d = 40$	51
18. Mean and turbulent particle-phase properties for the case II jet at $x/d = 16$	52
19. Mean and turbulent particle-phase properties for the case II jet at $x/d = 24$	53
20. Mean and turbulent particle-phase properties for the case II jet at $x/d = 40$	54
21. Sketch of near-injector region.....	55
22. Sketch of dense-spray apparatus.....	56
23. Sketch of gamma-ray absorption system.....	57
24. Flash photographs of the case 1 liquid jet.....	58
25. Flash photographs of the case 2 liquid jet.....	59

26.	Flash photographs of the case 3 liquid jet.....	60
27.	Light-sheet photographs of the case 3 liquid jet.....	61
28.	Mean liquid volume fractions at $x/d = 1$	62
29.	Mean liquid volume fractions along axis for the liquid jets.....	63
30.	Mean liquid volume fractions for the case 2 liquid jet.....	64
31.	Mean liquid volume fractions for the case 3 liquid jet.....	65

Nomenclature

<u>Symbol</u>	<u>Description</u>
a	acceleration of gravity
c	concentration of particles
C_D	drag coefficient
C_i	empirical constants
d	injector exit diameter
d_p	particle diameter
f	mixture fracture
g	square of mixture fraction fluctuations
k	turbulence kinetic energy
L_e	dissipation length scale of eddy
L_{FC}	length of contiguous liquid core
\dot{m}_o	injector mass flow rate
m_p	particle mass
M_A	acceleration modulus
M_o	injector thrust
\dot{n}_i	number of particles in group i per unit time
Oh	Ohnesorge number, Eq. (33)
P(f)	Favre-averaged probability density function of f
r	radial distance
Re	Reynolds number
S_ϕ	source term
$S_{p\phi}$	source term due to particles
t	time
t_c	eddy lifetime
T	temperature
u	axial velocity
u_r	difference between dispersed and continuous phase velocities
v	radial velocity
V_j	volume of computational cell j
w	tangential velocity
We	Weber number, Eq. (21)
x	streamwise distance
Y_i	mass fraction of species i
∞	void fraction
∞_f	liquid volume fraction
δ_{ij}	Kroneker delta function
Δt_p	residence time of a particle in a computational cell
Δ_A	correction of virtual mass force
Δ_H	correction of Basset history force
ϵ	rate of dissipation of turbulence kinetic energy
μ	viscosity
μ_t	turbulent viscosity
ν	kinematic viscosity

ρ	density
σ	surface tension
σ_i	turbulent Prandtl/Schmidt number
ϕ	generic property
ζ	integration variable, Eq. (14)

Subscripts

a	air
c	centerline value
f	liquid value
g	gas value
in	start of particle path in computational cell
out	end of particle path in computational cell
p	particle property
r	relative value
w	water
o	initial condition
∞	ambient condition

Superscripts

(-)	time-averaged quantity
(~)	Favre-averaged quantity
(- ')	time-averaged root-mean-square fluctuating quantity
(~ ")	Favre-averaged root-mean-square fluctuating quantity

1. INTRODUCTION

The potential value of rational design procedures for liquid-fueled combustors has motivated numerous efforts to develop methods for analyzing spray evaporation and combustion processes. The goal is to reduce the time and cost of cut-and-try combustor development. This investigation seeks to contribute to the development of this methodology, by studying several fundamental phenomena associated with sprays -- particularly the dense-spray region near the exit of the fuel injector passage. The research has application to airbreathing propulsion systems, e.g., liquid-fueled primary combustors and afterburners. The results of the research are also relevant to other spray combustion processes, e.g., fuel-injected internal-combustion engines, diesel engines, furnaces, etc.

The present investigation specifically considers three problems concerning sprays, as follows:

1. Processes in dilute sprays (dispersed-phase volume fractions less than five percent) where the densities of the dispersed and continuous phases are comparable.
2. Mechanisms which control mixing and drop formation in the near-injector dense-spray region of a pressure atomizing injector.
3. Mechanisms which control the production and damping of continuous-phase turbulence by the dispersed phase.

These issues are being investigated both theoretically and experimentally.

The research is planned for a three-year period. This report describes activities during the first year of the study. In the period, the research was confined to the first two phases of the study, namely, dilute spray processes and near-injector phenomena of pressure-atomizing injectors. Dilute sprays were studied by considering a particle-laden liquid jet in a liquid environment (glass/water). The dense-spray study involved a large-scale water jet in still air. Findings for both phases of the research are considered, in turn, in the following. The report concludes with a summary of articles, participants and papers associated with the investigation.

2. PARTICLE-LADEN JETS

2.1 Introduction

Several earlier studies concerning the structure of turbulent multiphase jets have been carried out in this laboratory. This work was limited to dilute dispersed flows (volume fraction of the dispersed phase less than one percent), in order to simplify both measurements and analysis. Key issues with respect to turbulent dilute multiphase flows involve interphase transport of mass, momentum and energy; turbulent dispersion of the dispersed phase (the effect of turbulent fluctuations on the cross-stream motion of the dispersed phase); effects of turbulent fluctuations on interphase transport properties; and effects of the dispersed phase on the turbulence properties of the continuous phase (called turbulence modulation, cf. Al Taweel and Landau, 1977). The last three items are all elements of turbulence/dispersed-phase interactions, and represent major areas of uncertainty for both dilute and dense sprays. These issues are of prime interest for the present study.

In addition to studying turbulence/dispersed-phase interactions, an objective of past work was to develop and evaluate models of sprays which could be used as predictive tools. In order to highlight various aspects of turbulence/dispersed-phase interactions, and to systematically develop the theory, a wide variety of flows were considered, as follows:

- (i) Single-phase constant density, variable density and combusting jets (Shearer et al., 1979; Mao et al., 1980; and Jeng et al., 1982, 1984, 1984a).
- (ii) Particle-laden gas jets (Shuen et al., 1983, 1983a, 1985; and Zhang et al., 1985).
- (iii) Nonevaporating sprays (Solomon et al., 1985, 1985a).
- (iv) Evaporating sprays (Shearer et al., 1979; Solomon et al., 1985b).
- (v) Combusting sprays (Mao et al., 1980, 1981; and Shuen et al., 1986).
- (vi) Noncondensing gas jets in liquids (Sun and Faeth, 1985, 1985a).
- (vii) Condensing gas jets in liquids (Chen and Faeth, 1982; and Sun et al., 1986b).
- (viii) Reacting gas jets in liquids (Chen and Faeth, 1983).

Several recent reviews summarize aspects of this work (Faeth, 1977, 1983, 1983a, 1986).

Aside from essential differences required to treat interphase transport properties, methods of analysis were similar for all these flows. Wherever possible, predictions were evaluated by comparison with measurements, considering well-defined initial and boundary conditions. By limiting attention to jet-like flows, both measurements and analysis were simplified, providing sufficient experimental data and high levels of numerical closure to assure definitive evaluation of analysis.

Three theoretical models of turbulent dispersed flows were considered: (1) locally homogeneous flow (LHF), where interphase transport rates are assumed to be infinitely fast so that there is no slip between the phases and the flow is in local thermodynamic equilibrium; (2) deterministic separated flow (DSF), where interphase transport rates are finite but effects of turbulence/dispersed-phase interactions are ignored by basing

interphase transport rates on the mean properties of the continuous phase; and (3) stochastic separated flow (SSF) where effects of finite interphase transport rates and turbulence/dispersed-phase interactions are considered using random-sampling for turbulence properties in conjunction with random-walk computations for the motion of elements of the dispersed phase. Full resolution of all aspects of dispersed multiphase flow by complete numerical simulation is hopeless in spite of remarkable advances in computer technology. Therefore, continuous-phase properties were analyzed using widely-adopted methods of $k-\epsilon-g$ turbulence models. All empirical factors in these models, however, were fixed on the basis of early work with constant-density shear flows and subsequently verified by comparison with measurements in constant- and variable-density single-phase jets (Shearer et al., 1979; Mao et al., 1980; and Jeng et al., 1984, 1984a).

Original sources and related review articles (Faeth, 1977, 1983, 1983a, 1986) should be consulted for detailed comparisons between predictions and measurements. The general conclusions were that effects of finite interphase transport rates and turbulence/dispersed-phase interactions were important for these flows, and probably for most practical sprays as well. The SSF approach was found to yield encouraging predictions, since it accounts for both of these effects. The LHF approach was found to be a useful limit, capable of treating very complex multiphase flows with minimal empiricism, however, this method invariably overestimates the rate of development of dispersed jets since finite interphase transport rates are ignored. Finally, notwithstanding its widespread use at present, DSF analysis was found to yield poor performance for all the flows tested (Faeth, 1986).

These findings represent an advance in our understanding of dilute dispersed jets (like dilute sprays), however, many deficiencies remain. First of all, the flows considered represented either dense particles in gases or bubbles in liquids, e.g., very large and very small phase density ratios. This leaves a significant gap in information for conditions where the densities of the two phases are comparable. This is unfortunate since the near-unity range is representative of conditions in high-pressure combusting sprays relevant to many practical applications.

A second limitation of this work involved the approach used to measure continuous-phase mean and fluctuating velocities. Laser Doppler anemometry (LDA) was used, but only with amplitude discrimination to separate signals from the dispersed and continuous phases. The approach was based on the fact that dispersed phase elements had diameters of 10 - 300 μm , yielding large amplitude signals in comparison to the ca 1 μm diameter seeding particles used to measure continuous-phase velocities. Modarress et al. (1984), however, point out that this approach does not provide a reliable phase-discrimination system, since grazing collisions of large particles with the LDA measuring volume generate small-amplitude signals which can be interpreted as originating from the continuous phase.

The objective of the present study was to eliminate these deficiencies. The system chosen for study involved dilute particle-laden water jets in still water, using nearly monodisperse glass beads as the dispersed phase. The density ratio of this system (2.45:1) provides needed measurements for conditions where phase densities are comparable and is representative of portions of high-pressure combusting sprays. Furthermore, for this density ratio region, all effects of interphase momentum transfer are important providing a good test of theory, e.g., particle inertia, virtual mass, drag, and the Basset history force. In addition, the measurements involved development and use of a phase-discriminating LDA, in order to eliminate biasing of continuous-phase turbulence properties by grazing collisions between particles and the LDA measuring volume.

Work on this phase of the study is not yet complete; therefore, the following is only a progress report. The report begins with a description of experimental and theoretical methods and concludes with a discussion of results found thus far. Final conclusions are deferred pending completion of this phase of the study.

2.2 Experimental Methods

2.2.1 Apparatus

A sketch of the particle-laden jet apparatus appears in Fig. 1. The flow is observed within a windowed test tank (410 x 534 x 913 mm high) used during earlier studies of bubbly jets (Sun and Faeth, 1986, 1986a; Sun et al., 1986). Filtered water is supplied to the injector using a rotary gear pump (Oberdorfer, Model 991R). A valve and bypass in the pump exhaust line was used to adjust the water flow rate. A 1300 ml surge tank (half-filled with water) was used to smooth pump-induced flow oscillations. The water flow rate was monitored with a rotameter (Schutte and Koerting, Model 3HCFB) which was calibrated by collecting water for timed intervals. The water inflow to the test tank was removed by an overflow pipe and returned to the reservoir.

The jet was produced by a constant area passage, 5 mm in diameter, injecting vertically downward. The passage was 70 diameters long, to insure fully-developed flow. Dried particles were fed to a standpipe, located directly-above the injector, where they mixed with the water and entered the jet flow while falling under the influence of gravity. Particle loading in the jet was controlled by adjusting the rate of particle feeding (an Accu-Rate, Model 310, particle feeder with a 25 mm center rod was used). After passing through the jet, the particles collected naturally at the bottom of the tank, where they could be removed from time to time using a suction system. The particles were then dried and reused, since they experienced no damage in the present flow system. The particles were reasonably monodisperse (0.5 mm nominal diameter with 73 percent between 0.455 and 0.545 mm diameter).

2.2.2 Instrumentation

Phase Velocities. The instrumentation was all nonintrusive, involving a phase-discriminating LDA, for mean and fluctuating phase velocities; and a Mie scattering system for measurements of particle number fluxes. The phase-discriminating LDA is illustrated in Fig. 2. The LDA is a conventional dual-beam system, using the 514 nm line of an argon-ion laser operated at ca. 200 mW. Forward scatter was used for measurements of continuous-phase velocities, while off-axis collection was used for measurements of particle-velocities, the latter to avoid unusual pedestal signals seen in forward scatter for larger particles, cf. Sun and Faeth (1986). A Bragg-cell frequency shifter was used to eliminate directional bias and ambiguity. Signal levels from the naturally-seeded water are much smaller than for particles crossing the measuring volume; thus, simple amplitude-discrimination serves to identify velocity signals from particles. This involves reducing the gain of the detector circuit until only signals from particles were recorded. This procedure was checked by terminating the flow of particles, which invariably resulted in no further signals being processed by the detector system. A burst-counter signal processor (TSI, Model 1990C) was used to find particle velocities from the Doppler signal. The output of the burst counter was stored on a minicomputer (IBM 9002) and subsequently processed to yield particle-averaged mean and fluctuating velocities. Use of particle averaged velocities represents no difficulties for the present study, since the output of the analysis could be summarized in the same way. Mean and fluctuating streamwise and radial particle velocities were measured, simply by orienting the plane of the LDA beams appropriately.

As noted earlier, grazing collisions of particles with the measuring volume can generate low-amplitude signals which appear to originate from natural seeding in the water and could bias continuous-phase velocity measurements. The phase-discrimination system pictured in Fig. 2 eliminates this problem. The method involves a third beam at 632.8 nm from a small HeNe laser (5 mW). A detector views light scattered from this beam through a laser-line filter, with the beam waist and collecting optics adjusted so that all grazing collisions are detected (the region viewed has a diameter greater than the sum of the largest particle and measuring volume diameters). The data processing system records the discriminator signal and eliminates all records where a pulse on this beam indicates the presence of a particle near the measuring volume. The normal signal from the continuous phase is a high data-density signal from a d/a conversion of a sample-and-hold circuit at the output of the burst counter (the time between valid velocity measurements is small in comparison to the integral time scale of the flow). Thus, this signal is time-averaged (ignoring periods where particles are present) to obtain unbiased time-averaged mean and fluctuating continuous-phase velocities. Various velocity components and the Reynolds stress were obtained by rotating the LDA beam plane, similar to past work (Shuen et al. 1986; Solomon et al. 1985 a,b; Sun and Faeth, 1986; Sun et al., 1986; among others).

The size of the LDA measuring volume was 0.10 mm diameter and 1.00 mm long for continuous-phase velocity measurements. Gradient broadening was negligible for present test conditions and experimental uncertainties were largely due to finite sampling times. Experimental uncertainties (95 percent confidence) are estimated as follows: mean streamwise velocities, 5 percent; fluctuating streamwise and radial velocities, 5 percent; turbulence kinetic energy, 10 percent; and Reynolds stress, 20 percent at its maximum and proportionately higher elsewhere.

The size of the LDA measuring volume was 0.75 mm diameter and 1.00 mm long for dispersed-phase velocity measurements, increased since grazing collisions of particles were recorded. Experimental uncertainties were largely due to finite sampling times for these measurements as well. Experimental uncertainties (95 percent confidence) are estimated as follows: mean streamwise velocities, 5 percent; fluctuating streamwise and radial velocities, 5 percent; and mean radial velocities, 50 percent. The uncertainty of the mean radial velocity was very high due to its small magnitude.

Particle Number Fluxes. The Mie-scattering system for measurements of particle number fluxes was similar to that of Sun et al. (1986). A sketch of this system appears in Fig. 3. The beam from a HeNe laser is passed through an aperture, to provide a beam having a nearly uniform intensity, and then directed toward the measuring volume by a first-surface mirror. The beam is observed, in a normal direction, by a detector. The output of the detector was displayed on an oscilloscope and recorded with a pulse counter having an adjustable threshold. As particles pass through the measuring volume, they generate a light pulse by Mie scattering. This signal is detected by the pulse counter, using the threshold to control spurious background signals. The region observed is approximately the sum of the optical area and an outer annular region having a width equal to the particle radius. The actual area of observation, however, was calibrated by collecting particles from a relatively uniform flow.

Experimental uncertainties for the particle number flux system are due to variable particle diameters, gradient broadening, and finite sampling times. The uncertainty (95 percent confidence) at the maximum particle number flux conditions (at the axis) is estimated to be less than 10 percent, with proportionally higher values elsewhere.

2.2.3 Test Conditions

Test conditions are summarized in Table 1. Three flows were considered, a pure water jet (as a baseline) and two particle-laden jets having initial particle volume flow rate fractions of 2.4 and 4.8 percent. The flows were reasonably turbulent, with initial Reynolds number of 8530. Initial flow velocities, ~ 1.6 m/s, were relatively low in comparison to particle terminal velocities, ~ 0.08 m/s; therefore, effects of buoyancy were significant, particularly far from the injector.

Table 1 Summary of Particle-Laden Jet Test Conditions^a

Flow	Water Jet	<u>Particle-Laden Jets</u>	
		I	II
Mass Loading Ratio (%) ^b	0	5.4	10.8
Particle Volume Fraction (%)	0	2.4	4.8
Initial Average Velocity (m/s)	1.61	1.61	1.61
Reynolds Number	8530	8530	8530

^a Initial conditions for a particle-laden water jet injected vertically downward in still water. Injector is a constant area passage (diameter of 5.08 mm) with a length of 350 mm.

^b Mass of particles/unit mass of water. Particles are round glass beads having 0.5-mm nominal diameter (73 percent in range 0.455 - 0.545 mm with a density of 2450 kg/m³).

2.3 Theoretical Methods

2.3.1 Description of Analysis

Theoretical methods follow the approach developed by Shuen et al. (1983, 1983a, 1985, 1986), Sun and Faeth (1986, 1986a) and Sun et al. (1986). The analysis considers a steady (in the mean), two-phase round turbulent isothermal particle-laden jet injected

vertically downward in a stagnant water bath at atmospheric pressure. Both particle and liquid densities are essentially constant, although in models neglecting slip between the phases, the flow exhibits overall variable density effects due to changes in the concentration of particles. Effects of buoyancy are important near the edge of the flow and far from the injector due to the density difference between water and the glass particles. Since the flows were dilute (the maximum particle volume fraction was less than 5 percent), the volume of the dispersed phase is ignored when formulating the equations governing the properties of the continuous phase. Particles are assumed to be monodisperse and interphase transport is based on the properties of the continuous phase at the center of each particle. Furthermore, particles are assumed to have uniform properties throughout their volume. Flow velocities were small; therefore, kinetic energy and viscous dissipation of the mean flow can be neglected with little error. Since the present flows spread similar to single-phase jets, the boundary layer assumptions are adopted for the continuous phase.

Three methods of treating multiphase flow, typical of current practice are examined: (1) locally homogeneous flow (LHF); (2) deterministic separated flow (DSF); and (3) stochastic separated flow (SSF). These methods, as applied in the present investigation, are described in detail in the following.

2.3.2 Locally Homogeneous Flow Analysis

The formulation of the LHF analysis corresponds to the general treatment of the continuous phase for all three analyses; therefore, this approach will be considered first. The LHF approximation implies that all phases have the same velocity and are in thermodynamic equilibrium at each point in the flow. Therefore, the flow corresponds to a variable-density single-phase flow, due to changes of particle concentration, even though the density of each phase is constant. Following Lockwood and Naguib (1975), and Bilger (1976, 1977), among others, we assume that the exchange coefficients of both phases is the same. Along with the other assumptions of the analysis, this implies that, f , the mixture fraction (defined as the fraction of mass at a point which originated from the injector) is a conserved scalar and that all scalar properties are only a function of f .

The turbulent flow analysis is based on an approach proposed by Lockwood and Naguib (1975), but modified to use mass-weighted or Favre-averaged quantities following Bilger (1976). Methods used here employ the specific formulation and empirical constants of Jeng and coworkers (1982, 1984, 1984a) as described by Sun and Faeth (1986, 1986a).

The general form of the governing equations is as follows:

$$\partial/\partial x (\bar{\rho}\tilde{u}\phi) + 1/r \partial/\partial r (r\bar{\rho}\tilde{v}\phi) = 1/r \partial/\partial r (r\mu_t/\sigma_\phi \partial\phi/\partial r) + S_\phi + S_{p\phi} \quad (1)$$

where

$$\tilde{\phi} = \bar{\rho}\phi/\bar{\rho} \quad (2)$$

denotes a Favre (mass-weighted)-average while an overbar denotes a conventional Reynolds (time)-average. Conservation equations are solved for mass ($\phi = 1$), momentum ($\phi = \tilde{u}$), mixture fraction ($\phi = \tilde{\phi}$), turbulent kinetic energy ($\phi = k$), rate of dissipation of turbulent kinetic energy ($\phi = \epsilon$), and the square of the mixture fraction fluctuations, ($\phi = g$). The expressions for the S_ϕ appearing in Eq. (1), along with the appropriate empirical constants, are summarized in Table 2. In the LHF formulation, source terms involving the dispersed phase ($S_{p\phi}$) do not appear, since the continuous phase and the dispersed phase

are in local equilibrium. The effect of buoyancy only appears in the governing equation for conservation of momentum, since buoyancy/turbulence interactions have been ignored in order to minimize the empiricism of the analyses. Jeng et al. (1982) find that buoyancy/turbulence interactions have little influence on predictions of mean properties even in flames, where the effect is greater than for the present flows; therefore, this approximation is justified. Empirical constants listed in Table 2 were all established using measurements in constant- and variable-density single phase jets (Jeng and Faeth, 1984) and have not been subsequently changed.

The Reynolds numbers of the test flows are on the order of 10^4 and effects of molecular viscosity are not very significant. Therefore, the turbulent viscosity, μ_t , appearing in Eq. (1) was calculated from k and ϵ as follows:

$$\mu_t = C_\mu \bar{\rho} k^2/\epsilon \quad (3)$$

Ambient values of \tilde{u} , \tilde{f} , k and ϵ and g are all zero for the flows treated here. Downstream of the potential core, gradients of these quantities are also zero at the axis. Initial conditions for LHF calculations were prescribed following past practice (Sun and Faeth, 1986, 1986a). Slug flow was assumed at the injector exit and all properties are taken to be constant, except for a shear layer having a thickness equal to 1 percent of the injector radius at the passage wall. The constant property portion of the flow is specified as follows:

$$x = 0, r < 0.99 d/2;$$

$$\tilde{u}_o = \dot{M}_o / \dot{m}_o, \tilde{f}_o = 1, k_o = (0.02 \bar{u}_o)^2 \quad (4)$$

$$\epsilon_o = 1.274 \times 10^{-4} \bar{u}_o^3 / d; g_o = 0$$

Equation (4) provides the inner boundary conditions until the shear layer reaches the jet axis. The initial variation of \tilde{u} and \tilde{f} is taken to be linear in the shear layer. Initial values of k and ϵ in the shear layer were found by solving their transport equations while neglecting convection and diffusion terms.

Under the assumption that the exchange coefficients of both phases are the same, the instantaneous particle concentration and fluid density are only functions of mixture fraction for the LHF analysis and can be found by adiabatic mixing calculations (Faeth, 1983). This yields the following expressions for mixture density, particle concentrations and particle volume fraction:

$$\rho = (f / \rho_o + (1 - f) / \rho_\infty)^{-1} \quad (5)$$

$$c / c_o = f \quad (6)$$

$$\alpha = f \alpha_o / [f + (1-f)(\rho_o / \rho_\infty)] \quad (7)$$

where ρ_o is the fluid density at the injector exit under the LHF approximation. When deriving Eqs. (5) - (7), use has been made of the fact that $\rho_f = \rho_\infty$ for present test conditions.

Table 2 Source Terms and Empirical Constants in the Continuous-Phase Governing Equations

ϕ	S_ϕ	$S_{\phi\phi}$
1	0	0
\tilde{u}	$+ a (\rho_\infty - \rho)$ $\mu_t (\partial \bar{u} / \partial r)^2 - \bar{\rho} \epsilon$	$V_j^{-1} \sum_{i=1}^n i_i m_p [u_{pin} - u_{pout} + a (\rho / \rho_p - 1) \Delta t_p]^*$ $\bar{u} S_{pu} - \bar{u} \bar{S}_{pu}$ (T.M. only)
k	0	0
\tilde{f}	$C_{\varepsilon 1} \mu_t \epsilon / k (\partial \bar{u} / \partial r)^2 - C_{\varepsilon 2} \bar{\rho} \epsilon^2 / k$	$-2 C_{\varepsilon 3} \mu_t \epsilon / k \partial \bar{S}_{pu} / \partial r$ (T.M. only)
ε	$C_{g1} \mu_t (\partial \bar{f} / \partial r)^2 - C_{g2} \bar{\rho} \epsilon g / k$	0
g	C_μ	$C_{\varepsilon 1}$
		$C_{\varepsilon 2} = C_{g2}$
		C_{g3}
		σ_k
		σ_ϵ
		$\sigma_f = \sigma_g$
0.09	1.44	2.8
		1.8
		0.015
		1.0
		1.3
		0.7

* Δt_p is the residence time of a bubble in a computational cell.

All Favre-averaged scalar properties can be determined by defining a Favre-averaged PDF of mixture fraction, $P(f)$, whose properties can be found from the solution of the governing equations. Given $P(f)$, the Favre-averaged mean value of any scalar property becomes:

$$\tilde{\phi} = \int_0^1 \phi(f) P(f) df \quad (8)$$

where $\phi(f)$ is the state relationship for the property, e.g., Eqs. (5) - (7). Following Bilger (1976), time-averaged properties are found from:

$$\bar{\phi} = \bar{\rho} \int_0^1 (\phi(f) / \rho(f)) P(f) df \quad (9)$$

where ρ can be found by setting $\phi = 1$ in Eq. (8). Also, the time-averaged PDF, $P(f)$ can be found from the following expression from Bilger (1976);

$$\bar{P}(f) = \bar{\rho} / \rho(f) P(f) \quad (10)$$

Following Lockwood and Naguib (1976), a clipped Gaussian probability density function was assumed for the Favre-averaged PDF, although the specific form used has little effect on predictions. $P(f)$ depends on the most probable value and the standard deviation of the distribution. Both these quantities can be found from the local values of \tilde{f} and g (given by solution of the governing equations) as follows:

$$\tilde{f} = \int_0^1 f P(f) df \quad (11)$$

$$g = \int_0^1 (f - \tilde{f})^2 P(f) df \quad (12)$$

Equations (11) and (12) provide two implicit equations for the unknown most probable value and variance of $P(f)$. Solution for these parameters was obtained from the table developed by Shearer et al. (1979). This completes the specifications of the probability density function.

The calculations were performed using a modified version of GENMIX (Spalding, 1977). The computational grid was similar to past work (Sun and Faeth, 1986, 1986a), thirty-three cross-stream grid nodes; streamwise step sizes limited to 6 percent of the current flow width or an entrainment increase of 5 percent -- whichever was smaller.

2.3.3 Interphase Transport

The treatment of the continuous phase in the separated flow models is similar to the LHF model, except that new source terms, S_{pi} , appear in the governing equations due to interphase transport. The test flows were very dilute; therefore, effects of the dispersed phase on turbulent quantities are ignored for the present. Furthermore, since the density of the continuous phase is constant and its volume fraction is nearly unity, Favre- and Reynolds-averaged quantities are identical. Therefore, equations for \tilde{f} and g , as well as the PDF procedure, are no longer needed.

Both separated flow models involve dividing the dispersed phase into n groups near the injector and determining the trajectory of each group in the flow field. The momentum exchange source term for grid node j (only one designation being required since the calculations are parabolic) is then given by:

$$S_{puj} = V_j^{-1} \sum_{i=1}^n \dot{n}_i m_p [u_{piin} - u_{piout} + a (\rho / \rho_p - 1) \Delta t_p] \quad (13)$$

where \dot{n}_i is the number of particles per unit time in group i, while "in" and "out" denote conditions entering and leaving computational cell j (having a cell volume V_j). The flow rate of particles along a given trajectory is conserved, since particles are neither created nor destroyed; therefore, \dot{n}_i is a constant specified near the injector to satisfy total particle volume flow rate requirements. The last term, $a (\rho / \rho_p - 1) \Delta t_p$, denotes the momentum increase due to the effect of buoyancy forces on the flow (where Δt_p is the time period between a particle entering and leaving the computational cell).

Particle transport is treated the same in both separated-flow models. Both involve solving the Lagrangian equations of motion and transport for the n particle groups to find particle trajectories -- given the initial conditions.

Initial conditions for separated-flow analysis were specified at $x/d = 8$, which was the position nearest the injector where all needed measurements could be made with acceptable spatial resolution and accuracy. Downstream of this position, particle volume fractions were less than 3 percent; therefore, particle collisions and effects of adjacent particles on particle transport properties were negligible. Particle dimensions were less than 10 percent of the flow width; therefore, particles were assumed to have a locally-uniform environment, based on liquid properties at their center. Similar to earlier particle-laden jet analysis (Shuen et al., 1985), particles were assumed to be spherical while Magnus forces and Saffman-lift forces were neglected.

Under these assumptions, the motion of the dispersed phase was obtained using the formulation of Odar and Hamilton (1964), reviewed by Clift et al. (1978), as follows:

$$(\rho_p / \rho + \Delta_A / 2) d u_{ri} / dt = a (\rho_p / \rho - 1) \delta_{li} - 3/4 C_D / d_p |\vec{u}_r| u_{ri} - \Delta_H \frac{(81 \nu)^{1/2}}{\pi \cdot d_p^2} \int_{t_0}^t (t - \xi)^{-1/2} \frac{du_{ri}}{d\xi} d\xi \quad (14)$$

where u_{ri} is the difference between bubble and fluid velocities and δ_{li} denotes the Kronecker delta function (u_r being vertical). The term on the left-hand side of the equation represents the acceleration due to the particle and virtual mass, while the terms on the right-hand side represent buoyancy, drag and Basset-history forces. The parameters Δ_A and Δ_H were empirically correlated by Odar and Hamilton (1964) as follows:

$$\Delta_A = 2.1 - 0.123 M_A^2 / (1 + 0.12 M_A^2) \quad (15)$$

and

$$\Delta_H = 0.48 + 0.52 M_A^3 / (1 + M_A)^3 \quad (16)$$

where the acceleration modulus, $M_A = (d u_r / dt) d_p / u_r^2$. The values of Δ_A and Δ_H vary between 1.0 - 2.1 and 1.00 - 0.48; the former values being the correct limit for the Basset-Boussinesq-Oseen (B-B-O) formulation of Eq. (14).

Particle Reynolds numbers did not reach the supercritical flow regime; therefore, the standard drag coefficient for solid spheres were approximated as follows (Faeth, 1977):

$$\begin{aligned} C_D &= 24 (1 + Re^{2/3} / 6) / Re, \quad Re \leq 1000 \\ &= 0.44, \quad Re > 1000 \end{aligned} \quad (17)$$

Integration of the equations for both the continuous and dispersed phases proceeded downstream from $x/d = 8$. Final results will involve calibration of particle drag by experimental results found using single particles, in order to minimize uncertainties. However, preliminary results reported in the following involve a priori estimates of drag using Eq. (17) and the mean particle diameter.

2.3.4 Deterministic Separated Flow Analysis

With the DSF approach, drop transport and motion is computed using local mean properties, estimated from the continuous-phase analysis. Thus, particle/turbulence interactions are ignored and particles follow deterministic paths, fixed by the location and velocity where initial conditions were specified. With this approach, only the particle source term in the mean momentum equation is considered, e.g., all particle/turbulence interactions are ignored.

First, the continuous-phase equation, Eq. (1) is solved to get mean properties at each point. The dispersed-phase equation of motion, Eq. (14), is then solved, using the local mean velocity to represent the ambient velocity of each particle. The particle motion then gives the source term for the continuous phase from Eq. (13), requiring iterative solution to close the properties of both phases.

The computational grid for the continuous-phase solution was the same as the LHF model. Trajectories of 1200 particles were computed in order to obtain statistically-significant results.

2.3.5 Stochastic Separated Flow Analysis

The SSF approach involves finding the motion of a statistically-significant sample of particles as they move away from the injector and encounter a succession of turbulent eddies. Thus, particle/turbulence interactions are taken into account and the particles interact with the instantaneous liquid properties; as opposed to the DSF model, where they only interact with mean-liquid properties. Treatment of the continuous phase is the same as for the DSF model.

The effects of turbulent fluctuations on interphase momentum transport are treated using a technique proposed by Gosman and Ioannides (1981) and subsequently developed in this laboratory for turbulent dispersed flows, cf., Faeth (1983). Trajectory calculations are the same as the DSF model, except that instantaneous eddy properties replace mean-liquid properties. Properties within each eddy are assumed to be uniform, but to change in a random fashion from eddy to eddy. Eddy properties are found by making random selections from the velocity probability density function. Isotropic turbulence was assumed, with a Gaussian PDF for each velocity component. All PDF's are fully defined by their means and variances, which are known from the k- ϵ -g analysis.

Particle groups are assumed to interact with a particular eddy as long as they do not traverse the eddy and the lifetime of the eddy is not exceeded. Evaluation of these conditions requires specification of a characteristic size and lifetime, following Shuen et al. (1983a, 1985):

$$L_e = C_\mu^{3/4} k^{3/2} / \epsilon \quad (18)$$

$$t_e = L_e / (2k/3)^{1/2} \quad (19)$$

Particles and eddies are assumed to interact as long as the time of interaction and the relative displacement of the particle and the eddy (from the start of interaction) are both less than t_e and L_e . When the interaction ends by the L_e criterion, the particles have traversed the eddy. Ending the interaction by t_e being exceeded implies that the eddy has captured the particle.

The remaining computations are similar to the DSF model. The random-walk calculations, however, required a larger number of particle groups to obtain statistically significant results e.g., 2000 groups. Due to the low particle volume fractions of present tests, effects of particle source terms in the governing equations for turbulence quantities, called turbulence modulation by Al Tawee and Landau (1977), were not large. Therefore, these terms were ignored for the present preliminary computations.

2.3. 6 Initial Conditions

Initial conditions for both phases must be known for separated-flow calculations. These measurements were undertaken at $x/d = 8$. It was very difficult to measure particle velocities closer to the injector because high particle densities tended to block the LDA signal. The measurements included: mean and fluctuating velocities, turbulent kinetic energy and Reynolds stress of the continuous phase; and mean and fluctuating velocities and number fluxes of the particle phase.

These measurements specify all needed particle properties at the initial condition, however, some continuous-phase properties must still be estimated. The tangential component of the mean continuous phase velocity was taken to be zero, $\bar{w} = 0$, since the particles gave no indication of swirling motion. The turbulence kinetic energy was computed, assuming that radial and tangential velocity fluctuations were the same, similar to past practice (Sun and Faeth, 1986, 1986a). Given profiles of \bar{u} , $u'v'$ and k , initial profiles of ϵ were estimated from the definition of the turbulent viscosity in the turbulence model, e.g.,

$$\varepsilon = C_\mu k^2 \frac{\partial \bar{u}}{\partial r} / \bar{u} \bar{V}' \quad (20)$$

2.4 Results and Discussion

Measurements completed thus far have been limited to phase velocities. Particle number flux measurements are currently in progress while calibration tests for particle drag properties are yet to be done, as noted earlier. Therefore, computations in the following have been carried out using estimated particle drag properties and the assumption of uniform particle number fluxes over the region where particles were observed at the initial condition position ($x/d = 8$). Furthermore, Basset forces have been neglected for the present. Thus, theoretical results in the following are only preliminary, and are presented here to provide an indication of results obtained to date.

2.4.1 Properties Along Axis

Predicted and measured profiles of mean continuous-phase velocities along the axis are illustrated in Fig. 4. Results are shown for the single-phase jet as well as for the two particle-laden jets. Predictions of all three analyses are shown, although the DSF and SSF approaches yield virtually the same results and are represented by a single line on the figure.

Even though the flow at the exit of the injector is a fully developed pipe flow, results in Fig. 4 suggest a potential core of usual dimensions. This is probably an effect of the particles in the injector flow, which generally causes a rather square velocity profiles in the tube -- more like a slug flow. Predictions of all three analyses are similar for present flow conditions, and are in reasonably good agreement with the measurements. However, past work has shown that continuous-phase properties are not a very sensitive indicator of the performance of analysis for dilute dispersed flows.

The variation of mean particle velocities along the axis of the two particle-laden jets is illustrated in Fig. 5. Predictions of all three analyses are shown on the figure. As before, predictions of the two separated-flow analyses are nearly identical, and are in reasonably good agreement with the measurements. The LHF analysis corresponds to continuous phase velocities, cf. Fig. 4, and tends to underestimate particle velocities far from the injector. This is largely an effect of buoyancy, which becomes more pronounced when liquid velocities become small in comparison to the terminal velocities of particles.

2.4.2 Continuous-Phase Velocities

Predictions and measurements of \bar{u} , \bar{u}' , \bar{v}' , k and $\bar{u}\bar{v}'$ will be compared for the continuous phase. The present turbulence model does not yield separate predictions of velocity fluctuations; therefore, predictions were obtained by assuming $\bar{u}'^2 : \bar{v}'^2 = k : k/2$, which are the ratios usually observed near the axis of single-phase jets (Wygnanski and Fiedler, 1969). Turbulence kinetic energy, k , was not measured completely, and was found by assuming $\bar{v}' = \bar{w}'$. In the following, flow variables are plotted as a function of r/x , which is the similarity variable for fully-developed jets and plumes (Wygnanski and Fiedler, 1969).

Predictions and measurements for the single-phase jet are illustrated in Figs. 6-8 for $x/d = 16, 24$ and 40 . The comparison between predictions and measurements is quite good for most properties, suggesting reasonable baseline behavior of the turbulence model for present test conditions. Exceptions are k , and to a lesser degree \bar{u} and \bar{v} , near the axis at $x/d = 24$. Repeated checking of the measurements, since they seem unusual based on past experience, yielded the same results. Thus, the difficulty at this position is not resolved as yet. The error appears largest for k , since it is a quadratic quantity. Discrepancies between predictions and measurements also are somewhat larger for the Reynolds stress, since experimental uncertainties are larger for this quantity and it is also quadratic in the velocity fluctuations.

Continuous-phase properties for the Case I and II particle laden jets are illustrated in Figs. 9-14, for the same three axial stations. LHF and SSF predictions are shown on the plots, however, DSF predictions were nearly identical to SSF predictions of continuous-phase properties. Predictions of mean and fluctuating velocities for all the models are in reasonably good agreement with the measurements in view of experimental uncertainties. Predictions of k and the Reynolds stress show greater discrepancies, largely because these quantities are quadratic. In general, the findings for the continuous-phase properties of the particle-laden jets are similar to earlier results for bubbly jets using the same apparatus (Sun and Faeth, 1986, 1986a; Sun et al., 1986).

2.4.3 Dispersed-Phase Properties

Predicted and measured particle velocities at $x/d = 16, 24$ and 40 are illustrated for the Case I and II particle-laden jets in Figs. 15-20. Predictions of LHF and SSF analyses are shown, although LHF predictions essentially correspond to results for a single-phase liquid. LHF predictions of fluctuating velocities were found using the ratios employed earlier for continuous-phase fluctuating velocities.

In general, the LHF analysis provides the best predictions of particle velocities, when plotted in the manner of Figs. 15-20. This is somewhat fortuitous, since the centerline velocity used to normalize the results is underestimated by the LHF approach, cf. Fig. 5; therefore, the SSF method actually provides better predictions of the unnormalized particle velocities.

Predictions of mean velocities are overestimated and velocity fluctuations underestimated using the SSF approach. Such results could be due to underestimation of the particle drag coefficient. Whether this is the case will be established when particle drag is calibrated. Underestimation of particle velocity fluctuations is also partly due to the assumption of monodisperse particles during predictions. Subsequent calculations will establish the degree of this effect by considering the actual particle size distribution. Another factor in underestimation of streamwise velocity fluctuations is the assumption of isotropic turbulence, even though present measurements indicate levels of anisotropy typical of single-phase jets, cf. Figs. 8-14. We also plan to evaluate this effect by using measured anisotropy levels during subsequent calculations.

2.5 Summary

Both analysis and measurements are incomplete at this point; therefore, it is premature to draw firm conclusions. Results considered thus far, however, suggest much improved performance for the LHF approach when phase density ratios are near unity than was the case for particle-laden jets in gases (Shuen et al., 1983, 1983a, 1985), sprays (Solomon et al., 1985, 1985a, 1985b) and bubbles in liquids (Sun and Faeth, 1986, 1986a; Sun et al., 1986). In particular, LHF results are reasonably good in the near-injector region where slip velocities are small in comparison to flow velocities. This is encouraging for one of the hypotheses of the present investigation, namely that LHF analysis may provide reasonable estimates of the structure of high pressure sprays (where phase density ratios also approach unity) in the dense near-injection region.

At this point, the separated flow methods have been less successful than in the past. However, this observation may change once calibrated particle drag values are used, and Basset forces and polydisperse effects considered. Particle number flux measurements, which are very sensitive to predictions of turbulent dispersion, will also provide a more definitive test of the relative value of the various methods.

Remaining experimental work on this phase of the study involves measurements of particle number fluxes and calibration of particle drag properties. More complete computations allowing for polydisperse particle sizes, Basset history forces, and anisotropic continuous-phase properties must also be completed. Finally, sensitivity of predictions to various parameters of the analyses and uncertainties of initial conditions must also be evaluated. It is anticipated that this work will be completed early in the second year of the investigation. Subsequent work will consider effects of turbulence modulation and collisions, using a different experimental arrangement.

3. DENSE SPRAYS

3.1 Introduction

The present investigation of dense-spray phenomena is considering the near-injector region of a round liquid jet in still air under atomization conditions. In order to define this flow, it is necessary to consider the breakup regimes of round liquid jets in gases and the flow regimes within the spray.

Ranz (1958) prescribed four regimes of liquid jet breakup, based on the liquid and gas Weber numbers of the flow, which are defined as follows:

$$We_f \text{ or } g = \rho_f \text{ or } g u^2_0 d / \sigma \quad (21)$$

The four regimes are called drip, Rayleigh breakup, wind-induced breakup and atomization. Drip involves the slow formation of large drops immediately at the jet exit, which then fall as a single stream. Rayleigh jet breakup is induced by surface tension effects; breakup occurs many jet diameters from the injector exit and yields a stream of drops having diameters larger than the jet diameter. Wind-induced breakup is due to instabilities caused by the relative motion of gas and liquid, stabilized to some extent by surface tension; breakup occurs many jet diameters from the jet exit and yields drop diameters ranging from the jet diameter to about one-order-of-magnitude smaller. The atomization regime is characterized by jet breakup immediately at the jet exit (at least at the surface which is the only visible region of the flow) yielding drops whose average diameter is much smaller than the jet diameter. The breakup mechanism of this last regime is unknown. Ranz (1958) proposed the Weber number criteria for these regimes listed in Table 3. These assessments, however, are only an approximate guide for flow transitions (Reitz, 1978).

Table 3. Liquid Jet Breakup Criteria

	Liquid Properties	Gas Properties
Drip	$We_f < 8$	$We_g < 0.4$
Rayleigh	$We_f > 8$	$0.4 < We_g < 0.8$
Wind-Induced	$We_f > 8$	$0.8 < We_g < 13$
Atomization	$We_f > 8$	$13 < We_g$

The present investigation is concentrating on processes associated with the atomization regime. Most practical spray systems require rapid interphase transport, which is promoted by the small drop sizes of the atomization regime. In fact, aside from start-up and shut-down conditions, the range of operating conditions for the other breakup regimes is relatively small. For example, a hydrocarbon liquid injected into a combustor at 10 bar with a 500 μm injector diameter would exceed atomization regime requirements for all liquid velocities greater than 5-10 m/s (with corresponding injector pressure drops on the order of 0.2 bar). Thus, a better understanding of the atomization regime serves the broadest range of applications.

There are several flow regions within a spray when it is operating in the atomization regime, as illustrated in Fig. 21. Within the injector passage, and far downstream (if the liquid is evaporating) we have single-phase flows. Near the injector, there is a dense-spray region, which generally contains an irregularly-shaped all-liquid core (Hiroyasu et al., 1982). This region is characterized by a variety of liquid configurations (drops, ligaments, globules, etc.), frequent collisions of the dispersed phase, significant effects of liquid volume fraction on interphase transport rates, and significant effects of the dispersed phase on the turbulence properties of the continuous phase. The dense-spray region extends an appreciable distance from the injector exit, ca. 200 injector diameters at atmospheric pressure conditions.

As mixing proceeds, the liquid volume fraction declines and the flow becomes a dilute spray. Dilute sprays are characterized by more-or-less spherical drops, infrequent drop collisions and little effect of liquid volume fraction on interphase transport rates and the turbulence properties of the continuous phase. The presence of the dispersed phase, however, still exerts a significant influence on the mean properties of the flow.

Past work on the dense spray region is relatively limited. Recent efforts in this area involve studies by Bracco and coworkers, at Princeton, and Hiroyasu and coworkers in Japan. Both these groups only considered round liquid jets, generally in the atomization regime, injected into a still or slowly moving gas having various densities.

The earliest Princeton work emphasized criteria for atomization and liquid breakup (Bracco, 1983; Reitz, 1978; and Reitz & Bracco, 1982, 1984). Measurements were limited to global quantities, such as visible spray angle, penetration of transient sprays, and injector discharge coefficients. It was proposed that the drop size expression developed by Taylor (1940) was appropriate for initial drop size estimates -- upon breakup. Reitz (1978), however, was vague concerning the actual region of the flow where this estimate applies. Several empirical expressions for initial spray angle, in the atomization regime, were also developed. The measurements showed that breakup, and the onset of atomization, was influenced by flow properties of the injector passage, e.g., length-to-diameter ratio, inlet design, etc. Estimates from Taylor's formula indicated very small initial drop diameters, ca. 1 μm , which are at least an order of magnitude smaller than drop sizes normally measured in sprays. It was suggested that the larger sizes resulted from drop collisions in the dense-spray region downstream of the breakup location.

The next study involved development of a model of dense sprays (O'Rourke & Bracco, 1980; O'Rourke, 1981). This is probably the most complete model of dense sprays currently available, however, most of its features are necessarily ad hoc and untested by comparison with measurements. The model considers drop collisions, following methods proposed for processes in rain clouds (Adam et al., 1968; Brazier-Smith et al., 1972; Delichateos and Probstein, 1976; Gunn, 1965; Langmuir, 1948; Ogura and Takahashi, 1973; Saffman and Turner, 1956; Srivastava, 1971; and Swinbank, 1947).

Effects of turbulent dispersion of drops were treated using an empirical turbulent drop diffusivity, a difficult approach since such diffusivities depend on both local turbulence and drop properties, implying substantial data bases to fully define the property. The SSF method of Shuen et al. (1983, 1983a, 1985, 1986) was designed to avoid this difficulty by providing a direct prediction of the diffusivity. Effects of high liquid fraction on drop transport rates were treated using empirical rate expressions developed for fluidized beds. Finally, the governing equations for the continuous phase allowed for the volume occupied by liquid -- which is straightforward. Specification of initial conditions was ad hoc, however, the results yield some general findings which are helpful. It was shown that drop collisions could cause transition in drop sizes from values estimated by Taylor's equation near the injector to more typical values downstream, e.g., to the levels measured by Hiroyasu and Kadota (1974). Furthermore, it was found that effects of liquid volume fraction on drop transport rates were not large for liquid volume fractions less than 10 percent.

The most recent work of this group has been devoted to examining whether the LHF approximations could be applied to sprays (Martinelli et al., 1983; and Wu et al., 1983, 1984). Since LHF analysis is not concerned with details, e.g., drop size distributions, separate phase velocities, etc., measurements have been confined to global quantities. This includes visible spray angle for particular photographic conditions, and flow velocities using laser Doppler anemometry. The LDA measurements used spray drops as seeding particles and are biased toward the smallest drops in a spray, since these have the highest number densities. These measurements were actually in the dilute-spray region. Similarly, spray photographs tend to emphasize the region containing small drops. Based on these measurements, the authors conclude that sprays at elevated pressures, typical of practical combustion processes, satisfy LHF approximations. In particular, they find that initial spread rates of sprays in the atomization regime are typical of those observed in single-phase jets. Cases where spread rates in the dense spray region are unusually large were observed (Reitz, 1978) but are not considered by this explanation, which was limited to high-pressure conditions.

The conclusions reached by the Princeton group (Martinelli et al., 1983; and Wu et al., 1983, 1984) are controversial. Their measurements are probably biased toward the smallest spray drops which are most likely to satisfy LHF approximations. Certainly, the evidence of existing detailed spray structure measurements supports significant effects of finite interphase transport rates in sprays (Faeth, 1983, 1986). The fact that the Princeton group only considers noncombusting flows also contributes to their conclusions, since such flows do not have a drop-containing region of finite length. Consideration of high pressure combusting sprays by the author and his associates (Mao et al., 1981) suggests that the LHF approximation improves at high pressures, but that finite interphase transport rates are still important since the spray-containing region is shorter due to the faster entrainment rates of high pressure sprays.

Hiroyasu and coworkers (1974, 1982) have also examined dense sprays. The objective of their most recent work was to determine the extent of the liquid core in the dense-spray region, cf. Fig. 21. They did this by spraying a somewhat conductive liquid through a metal screen placed at various distances from the injector. Indications of a conductive path between the injector and the screen then were interpreted as the presence of a continuous liquid core. They found that the liquid core could extend substantial distances into the flow field, e.g., on the order of 100's of injector diameters.

Other global studies of dense sprays, yielding parameters like visible spray angle and drop sizes, are legion, cf. Giffen and Muraszew (1953). The problem with this work is that spray angle is a poorly defined quantity, varying with distances from the injector and

photographic conditions, while drop size distributions also vary continuously throughout the flow. Attempting to characterize an entire spray by single properties of this nature is simply not a very useful idea. One concludes that existing knowledge of even the topography of the near injector region of sprays is surprisingly limited.

The objective of the present investigation is to study the near-injector dense-spray region of round liquid jets in still air in order to remove some of the deficiencies of existing knowledge concerning this flow. Of particular interest was to determine whether this region approximates locally homogeneous flow -- particularly those regions where liquid fractions are large. Both theory and experiment are being employed to carry out the objectives of the research. The experiments employ large diameter (5 - 20 mm) water jets, in order to provide adequate spatial resolution; and nonintrusive diagnostics, which reduces the uncertainties of probe measurements in this complex multiphase flow. Analysis follows procedures described earlier with respect to the particle-laden jet study, in order to achieve a unified methodology for spray predictions.

Work on this phase is also not yet complete; therefore, the following is only a progress report. The report begins with a description of experimental and theoretical methods and concludes with a discussion of results found thus far. Final conclusions are deferred pending completion of this phase of the study.

3.2 Experimental Methods

3.2.1 Apparatus

Figure 22 is a sketch of the water-jet apparatus. The main objective of these tests is to study the inertially dominated atomization regime; therefore, jet scale is chosen to obtain good spatial resolution while still being representative of practical sprays, e.g., injector diameters are in the range 5-20 mm. The injector consists of a honeycomb flow straightener (1.6 mm cells, 25 mm long), a smooth converging section from the 35 mm diameter water supply tube, and finally, a stainless steel constant area passage having a length-to-diameter ratio of 50. This insures a well-defined liquid flow with no swirl at the jet exit, while minimizing problems of cavitation in the passage. Measurements to date have been limited to a 9.5 mm diameter passage.

City water is supplied to the nozzle using a Pennsylvania Pump and Compressor Co., Type 2 1/2" 2-S OMSR centrifugal water pump (12.6 l/s at 2.1 MPa delivery pressure). The rate of flow is adjusted by a bypass system and measured with an Oilgear Co. PV meter (Type PL 15C-2A1s-15TD2/UNO-AC15N-25-0100-005-003) with a digital readout. The flow meter was calibrated by collecting water for timed intervals. The water is collected in a tub at the downstream end of the spray and discharged to a drain. A baffle at the top of the tub, prevents mist from rising into the test area. Water temperature is monitored with a submerged thermocouple.

Instrumentation is mounted rigidly; therefore, the injector is traversed (1 m horizontally and 2m vertically) to measure flow structure. The injector is mounted on a plate which traverses horizontally on a linear bearing assembly (25 mm diameter) whose position is adjusted by a computer-controlled Velmex, Inc. Unislide lead screw and stepping motor (Models B4036Q1J, M092-FD08 and 4-8311). The horizontal position is recorded using a Velmex, Inc. Digital Position Readout (4-8518), readable to 5 μm . The vertical traverse uses 25 mm diameter linear bearings as well, mounted on two I beams which are attached at the ceiling and the floor. The vertical position is set with a cable and

winch since only fixed axial stations are considered. Vertical position is measured with a ruler, accurate to 0.5 mm.

3.2.2 Instrumentation

Measurements include flow visualization, using flash and continuous photography; liquid volume fraction distributions, using gamma-ray absorption; and initial liquid velocity distributions and air entrainment rates, using laser Doppler anemometry. All systems will be described, although measurements to date have been limited to flow visualization and liquid volume fraction distributions.

Flash photography was based on a Xenon Corp., Pulsar Flashlamp System (Model 457) which can provide a 10 J light pulse with a 1 μ s duration. These photographs were obtained in a darkened room using an open camera shutter, with the flash lamp controlling the time of exposure. These photographs were obtained with a 4 x 5 Speed Graphic camera using Polaroid, Type 57, 3000ASA black and white film.

Continuous photographs were used to observe the general appearance of the flow, with no attempt to stop the motion. This employed a bank of flood lights to illuminate the spray along with the camera system used for the flash photographs.

The light sheet photographs were obtained by rapidly sweeping a laser beam in a vertical plane through the axis of the spray. An argon-ion laser (4W, Coherent, INNOVA 90-4), operating in the all-lines mode, was used for the light source. The laser beam was directed to a rotating mirror assembly which provided the sweep of the unfocussed laser beam (ca. 1 mm in diameter) through the spray. The rotary speed and position of the rotating mirror were adjusted to provide a short exposure time (ca. 1 μ s for the beam to move a distance equal to its diameter) for each element of the flow. Photographs were obtained in a darkened room with the camera adjusted so that the shutter was open for a time comparable to one rotation of the mirror -- capturing one sweep of the laser beam through the flow. A Pentax ME super camera, fitted with an Albinon F.3.9 (80 - 200 mm focal length) Zoom lens, was used for these photographs. Best results were obtained using Fujicolor 1600 ASA color film.

Figure 23 is a sketch of the gamma-ray absorption system. The general design of the system followed Gomi and Hasegawa (1984), Ohba (1979) and Schrock (1969). An Iodine 125 isotope source (2 mCi, emitting primarily at 27.47 keV) provided a soft gamma-ray source yielding optimum absorption levels in order to minimize experimental uncertainties for the absorption measurements. The source was placed in a lead casket with a 1.6 mm diameter x 13 mm long collimating aperture. The front of the casket was fitted with a 12 mm thick removable lead shield to cover the source during periods when it was not in use. Gamma rays passing through the flow were detected and counted using a Bicron Model 1 x M.040/1.54 X-ray probe. A lead aperture (1.5 - 6 mm in diameter, depending on position, and 12 mm long) was placed in front of the detector to define the path observed through the flow. The data acquisition system involved an EG&G Ortec single-channel analyzer and counter/timer (Models 556, 590A, 974). The energy window of the analyzer was centered at 27.5 keV to minimize spurious counts due to background radiation and Compton scattering (the latter effects is not large, however, in the present energy range). Detector output was stored and processed using an IBM 9002 microcomputer.

Absorption measurements were made for 30-60 parallel paths through the flow. These measurements were found to be very symmetric; therefore, measurements on both sides of the axis were averaged and smoothed to provide a single set of absorption

measurements for a given cross-section of the flow. These line-of-sight measurements were then deconvoluted, following the procedure of Santoro et al. (1981), to yield radial distributions of void fraction. Schrock (1969) and Gomi and Hasegawa (1984) point out that this method has a fundamental uncertainty depending on whether parallel or normal liquid laminae are assumed. However, the narrow absorption paths used during present experiments reduced this effect to less than 5 percent.

The gamma-ray absorption system was calibrated, using water-filled cells to measure the linear absorption coefficient. The liquid jet itself was also used to develop the method, based on nonatomization conditions where the flow formed a smooth liquid column near the exit of the injector. The latter arrangement was used to select the number of absorption measurements and the number of counts for each absorption measurement, trading off test time and experimental uncertainty. Specifications were set at 30-60 absorption measurements (varying with the width of the flow) and ca. 25000 counts at each position. Richardson extrapolation of these results to their limits indicated experimental uncertainties of centerline void fraction less than 5 percent, with proportionately higher values elsewhere.

Laser Doppler anemometry is used to measure flow properties at the exit of the injector and the gas entrainment rate of the spray. Knowledge of injector exit conditions is important for analyzing the flow, particularly due to the large inertia of the water which causes initial conditions to have a significant effect on the entire flow field. The entrainment rate measurements provide an accessible result, amenable to nonintrusive measurements, which will be useful for evaluating the mixing predictions of the analysis.

The arrangement of the LDA for both measurements is similar to recent work in this laboratory (Lai et al., 1985, 1985a). The LDA operates with an argon-ion laser (4W, Coherent, INNOVA 90-4) using the 514.5 nm line at powers up to 800 mW. A dual-beam frequency-shifted (40 MHz Bragg cell, TSI Model 9180-12, downshifted as necessary) arrangement is used to control the output frequency range and eliminate effects of directional ambiguity and bias. Collecting optics and a photomultiplier (TSI Model 9160) are used for signal detection. Data is obtained using a burst counter signal processor (TSI Model 1990 C). Low burst density (one seeding particle in the measuring volume at all times) and high data density (the time between validated signals is small in comparison to the integral time scale of the flow) signals are obtained; therefore, the filtered analog output of the processor is time averaged to yield unbiased results. Averaging is accomplished using an IBM 9002 microcomputer.

The LDA configuration differs somewhat for measurements of exit conditions and entrainment. Exit conditions are measured with the injector submerged in water, since refraction effects preclude direct measurements in air. This represents no problem, since flow properties at the end of the injector are not influenced by the surroundings of the spray. To carry out these measurements, a windowed cell is placed over the injector, with a slightly-restricted exit at the bottom which allows the cell to fill with water above the exit of the injector, while still allowing the water to flow out. The optical arrangement in this case differs from most dual-beam configurations, since one beam is directed along the optical axis while the other intersects it at an angle. However, this arrangement allows measurements within 1 mm of the jet exit, minimizing uncertainties in initial conditions. Various velocity components and turbulence quantities (\bar{u} , u' , v' , $\bar{u}\bar{v}'$) are measured by orienting the beams in various planes. The local water supply contains adequate natural seeding for these measurements. Uncertainties in u are less than 3 percent; in u' and v' less than 7 percent; and $u\bar{v}'$ less than 15 percent at the maximum position and proportionately higher elsewhere.

A conventional forward-scatter LDA arrangement is used for entrainment measurements. In this case, a horizontal beam plane is used, directly providing \bar{v} at a given radial location. These measurements can be directly correlated with entrainment predictions of the analysis. Seeding particles are provided by a bay-oil smoke generator in the ambient air, yielding particles on the order of 1 μm in diameter.

3.2.3 Test Conditions

Thus far, tests have been limited to one injector, having a passage diameter of 9.5 mm, and three flow rates. These test conditions are summarized in Table 4. Reynolds numbers for these tests are quite high, ca. 10^5 . The determination of the breakup regime will be discussed later, in conjunction with flash photographs of the sprays, however, the highest flow rate condition (case 3) was clearly in the atomization regime.

Table 4. Summary of Dense Spray Test Conditions^a

Case	Injector Pressure (kPa)	Flow Rate (kg/s)	$Re_f \times 10^5$	Breakup Regime
1	230	0.39	0.52	1st Wind-Induced
2	576	1.55	2.07	2nd Wind-Induced
3	2690	3.99	5.34	Atomization

Injector diameter of 9.5 mm with a length-to-diameter ratio of 50. Ambient temperature 25° C. Ohnesorge number of 1.21×10^{-3} . $Re_f = 1.54 \times 10^5$ for atomization from Miesse (1955) at these conditions.

3.3 Theoretical Methods

3.3.1 Description of Analysis

Present analysis of dense sprays is limited to the LHF approach, since applicability of LHF methods in this region is one of the main theoretical issues of the investigation. Furthermore, the complex topography of the near-injector region implies that separated flow analysis would be premature at this time. The main features of the LHF analysis are identical to the analysis of particle-laden jets, described in Section 2.3.3, and will not be repeated here. However, the character of the state relationships differ for the present flows; therefore, this aspect of the analysis will be discussed in the following.

3.3.2 LHF Formulation

Under present assumptions, the scalar properties of the dense spray are only a function of the mixture fraction. These properties can be found by straightforward thermodynamic computations for adiabatic mixing and equilibrium of various mixtures of injected and ambient fluid. For present experimental conditions two limits for state relationship computations can be defined, as follows: (1) the ambient environment is fully saturated with water vapor; and (2) the ambient relative humidity is less than 100 percent. The second condition is of importance for present conditions since finely-atomized drops near the edge of the dense spray tend to evaporate, in order to saturate their surroundings, which modifies liquid volume fractions in this region.

When the ambient air is fully saturated with water vapor, there is no tendency for the injected water to evaporate and we have a simple isothermal mixing process. Of particular interest are the density of the mixture, which is needed for solutions of the governing equations; and the liquid volume fraction, which is measured. The expressions for these quantities are as follows:

$$\rho = (f / \rho_o + (1-f) / \rho_\infty)^{-1} \quad (22)$$

$$\alpha_f = 1 - \alpha = (1 + (\rho_o / \rho_\infty)(1-f) / f)^{-1} \quad (23)$$

where Eq. (22) is the same as Eq. (5) for the particle-laden jet. It is also helpful to have an expression for f in terms of α_f , since the latter quantity is measured. This expression is

$$f = (1 + (\rho_\infty / \rho_o)(1 - \alpha_f) / \alpha_f)^{-1} \quad (24)$$

When the ambient air is not saturated with water vapor, the requirements for thermodynamic equilibrium imply that water evaporates until equilibrium is achieved in an adiabatic saturation process. This gives rise to a region at small, but finite, mixture fractions where no liquid is present; and there is a slight reduction in the temperature of the flow, due to absorption of sensible energy by the enthalpy of vaporization. Analysis of this situation follows Shearer et al. (1979) and Solomon et al. (1985b) for the state relationships of evaporating sprays under the LHF approximation.

We consider the flow to contain two species, air and water, and two phases, gas and liquid. The solubility of air in the water is neglected; therefore, the liquid phase is pure water while the gas is a mixture of air and water vapor. The expression for the composition of the mixture is:

$$Y_i = Y_{io} f + Y_{i\infty} (1 - f), i = a, w \quad (25)$$

Water may exist in both the gaseous or liquid state; therefore,

$$Y_w = Y_{wf} + Y_{wg} \quad (26)$$

The total enthalpy of the flow during the mixing process can be expressed as

$$h = h_o f + h_\infty (1 - f); \text{ where } h = Y_{wf} h_{wf} + Y_{wg} h_{wg} + Y_{ag} h_{ag} \quad (27)$$

Finally, requirements for equilibrium imply that the vapor pressure relationship of water must be satisfied for the gas phase,

$$Y_{wg} = f(p, T) \quad (28)$$

where $f(p, T)$ represents the Clausius-Clapeyron equation, or a more precise empirical equivalent, for water vapor. Given f and expressions for $f(p, T)$ and the h_i , Eqs. (25) - (28) can be solved to find the Y_i and T . The density and liquid fraction of the mixture can then be found from the following expressions

$$\rho = (Y_{wg}/\rho_{wg} + Y_{wf}/\rho_{wf} + Y_{ag}/\rho_{ag})^{-1} \quad (29)$$

$$\alpha_f = Y_{wf}(\rho/\rho_{wf}) \quad (30)$$

These computations are readily carried out for a range temperatures and ambient humidities.

3.3.3 Initial Conditions

For these computations, initial conditions can be obtained at the injector exit, where \bar{u} , \bar{u}' , \bar{v} and $\bar{u}'\bar{v}'$ are measured. Assuming that $\bar{v} = \bar{w} = 0$, which is appropriate for nonswirling, fully-developed pipe flow; and using existing relationships for \bar{w}' as a function of \bar{u}' , \bar{v}' for fully developed pipe flow; all initial conditions needed for the computations can be found similar to the approach described in Section 2.3.7.

3.4 Results and Discussion

3.4.1 Flow Visualization

Flash photographs for the three liquid jet test conditions appear in Figs. 24 - 26. Four pictures are shown for each test condition, near the exit and centered at $x/d = 50, 100$ and 150 . The lowest position appearing in the photographs is nearly $2m$ from the injector exit.

The case 1 and 2 sprays, illustrated in Figs. 24 and 25, correspond to the wind-induced breakup regime, while the case 3 spray, illustrated in Fig. 26, corresponds to the atomization regime. The case 1 jet corresponds to the first wind-induced breakup regime, defined by Reitz (1978). Breakup occurs far from the injector, yielding drops whose diameters are comparable to the initial jet diameter. Breakup is attributed to surface tension, augmented by the motion of the surrounding gas.

An interesting feature of the results illustrated for the case 1 jet in Fig. 24 is that the liquid surface exhibits fine-grained roughness near the injector but becomes smoother (with large-scale irregularities appearing) far from the injector. A shift in the turbulence spectra of both phases toward lower wave numbers is probably involved in this phenomena. Liquid-phase turbulence properties near the injector exit are governed by the tube flow. However, once the flow leaves the injector, liquid velocities become more uniform since the gas cannot retard the surface velocity as effectively as the wall of the passage. This reduces turbulence production in the liquid, causing the turbulence to decay with the large wave-number end of the spectrum disappearing first. The developing flow in the gas phase also favors the smallest scales near the injector exit. If liquid velocities were higher, so that drops formed at the surface, smaller asperities would lead to smaller drops. This suggests smaller drops forming from the liquid column near the injector, with drop sizes at

formation progressively increasing with increasing distance from the injector. This would yield a drop size distribution with the largest drops near the axis at the end of the dense-spray region, which is generally observed. The extent to which initial jet turbulence influences drops sizes for typical injectors is still open to question, however, since most pressure-atomizing injectors have short passages with little time for turbulence to develop (Bracco, 1983).

Higher velocities yield conditions for the second wind-induced breakup regime, illustrated in Fig. 25. Breakup occurs far from the injector and yields drops having diameters much smaller than the jet diameter. Decay of liquid surface roughness also evident here, with large-scale disturbances, reminiscent of Fig. 24, appearing in the all-liquid core far from the injector.

With an additional increase in the jet velocity, the flow enters the atomization regime pictured in Fig. 26. The atomization regime is defined by breakup of the liquid surface immediately at the tube exit, thus all higher flow rates have the same appearance. Drops near the injector exit are probably small. The wispy appearance of the drop-containing region, similar to a single-phase flow containing tracer particles, is evidence for this. Clear areas of drops intermittency penetrate the drop-containing region. However, near the jet exit, the extent of penetration is quite small, suggesting an underlying all-liquid core similar to Figs. 24 and 25. The depth of penetration increases with distance from the injector, but drop intermittency is not seen at the axis until $x/d \sim 150 - 200$.

The results illustrated in Figs. 24-26 provide an opportunity to check existing criteria for the onset of atomization and the length of the liquid core in the atomization breakup regime. The criterion for the onset of atomization proposed by Ranz (1958), from Table 3, is as follows:

$$\rho_g u_o^2 d / \sigma > 13 \quad (31)$$

Miesse (1955), citing Littaye (1943), recommends the same criterion for the onset of atomization, except with the RHS having a value of 40.3 instead of 13. Following Reitz (1978), Eq. (31) can be rearranged to yield the boundary between the wind-induced and atomization regimes, as follows:

$$R_{ef} = (3.6 - 6.4) (\rho_f / \rho_g)^{1/2} / Oh \quad (32)$$

where the Ohnesorge number, Oh , is defined as follows:

$$Oh = \mu_f / (\rho_f d \sigma)^{1/2} \quad (33)$$

and

$$Re_f = \rho_f u_o d / \mu_f \quad (34)$$

The range of the constant appearing in Eq. (32) follows from the Ranz (1958) and Miesse (1955) recommendations.

For present test conditions, using the Miesse criterion, the value of Re_f at the onset of atomization is 1.54×10^5 . Referring to Table 4, the case 3 jet has a Reynolds number of 5.34×10^5 and is in the atomization regime, satisfying the criterion of Miesse (1955). The case 2 jet, however, is slightly above the limit but still appears to be in the wind-induced breakup regime. A discrepancy of this type is not unusual for a flow regime transition, due to uncorrelated secondary properties which influence transition and differences in the interpretation of the appearance of a multiphase flow by various observers.

Hiroyasee et al. (1982) and Chehroudi et al. (1985) have studied the length of all-liquid core for the atomization regime of pressure atomized sprays. Chehroudi et al. (1985) correlate the length of the contiguous liquid core, L_{FC} , as follows:

$$L_{FC} / d = C_c (\rho_f / \rho_\infty)^{1/2} \quad (35)$$

where C_c is a constant in the range 7-16. The lower value of the constant is from their measurements while the higher value is from the results of Hiroyasu et al. (1982). Use of Eq. (35) places the length of the contiguous liquid core in the range $L_{FC} / d = 200 - 430$ for the conditions of the case 3 jet. The flash photographs illustrated in Fig. 26 for this flow suggest that the lower value is quite reasonable.

Light sheet photographs for the case 3 spray are illustrated in Fig. 27. Four photographs are shown, one near the injector exit and the others centered at $x/d = 50, 100$ and 150 . Each photograph covers a region roughly 20 injector diameters long. The laser beam illuminated the flow from the left; therefore, the right side of the flow is obscured by blocking of the beam due to refractive effects associated with the all-liquid core.

The light sheet photographs of Fig. 27 also support the presence of an all-liquid core extending well into the flow. Liquid appears to be torn from the surface as drops, irregular liquid elements and ligaments. The ligaments subsequently break up into streams of drops with a backward relative deflection as the outermost drops slow in the low speed gas near the edge of the flow. The density of resolvable large drops is surprisingly low in the drop-containing region, thus, it may prove possible to use optical diagnostics in this region, to gain information of drop sizes and relative velocities between the phases. We hope to explore this possibility in the future. The presence of large drops and ligaments near the all-liquid core suggests that large drops appear upon formation. This differs from the opinion of Bracco (1983) and Chatwani and Bracco (1985), who attribute the presence of large drops to coalescence of small drops formed by aerodynamic breakup into small drops at the liquid surface.

3.4.2 Liquid Volume Fraction Distributions

Measurements of liquid volume fraction distributions for the liquid jets will be considered in the following. While our prime interest is properties in the atomization breakup regime, consideration of the other cases is useful for fixing bounds of analysis. Analysis is being deferred until testing is completed for the 9.5 mm diameter injector; therefore only experimental results are considered in the following.

Figure 28 is an illustration of liquid volume fraction distributions near the injector ($x/d = 1$) for the liquid jets. The deconvoluted results are plotted at points where absorption measurements were made, deleting some of the data points in order to avoid overlapping the symbols. At this condition, the liquid volume fraction should be unity over the central portion of the flow, since mixing of the ambient gas has just begun. The measurements

yielded values within 5 percent of unity (within 2 percent on the average) which provides a satisfactory check of the test procedure. The largest departures from unity were due to alias signals which develop near the axis of the flow when there are abrupt changes in the liquid volume fraction in the region traversed. This behavior is due to the finite spatial frequency response of absorption measurements (made with a finite spacing) and is invariably encountered with deconvolution results (Santoro et al., 1981). Departures of this type did not appear in critical regions of the flow and were not large in any event; therefore, they are easily removed by smoothing the final results with a digital filter.

The flows illustrated in Fig. 28 appear to have spread significantly, e.g., the liquid volume fraction transitions from unity to zero in a region roughly 2mm wide. While some mixing occurs at this position, the present measurements overestimate the effect due to gradient broadening, e.g., the aperture of the radiation detector was roughly 1.5 mm. This effect could be eliminated by correcting the absorption measurements first with a detector slit function before final deconvolution to yield radial distribution of liquid volume fraction. However, spatial resolution is adequate with minimal gradient broadening over most of the flow; therefore, this step has not been taken for the present.

The variation of liquid volume fraction along the axis of the liquid jets is illustrated in Fig. 29. The near-injector region, $x/d < 10$, exhibits a liquid volume fraction of unity. However, the liquid volume fraction drops precipitously for $x/d > 10$, reaching values on the order of 0.2 at $x/d = 150$. Predictably, the well-atomized case 3 jet exhibits a faster decay rate of liquid volume fraction than the others. Much of the reduction in liquid volume fraction for the case 1 and 2 jets is due to flapping (or liquid intermittency) of the contiguous liquid core (cf. Fig. 25) since these flows exhibited little liquid breakup in the region where observations were made.

When interpreting these results, it should be recognized that the liquid volume fraction is a very sensitive function of f due to the large phase density ratio of the present flow. This can be seen from the results summarized in Table 5. Liquid volume fraction is tabulated as a function of mixture fraction, assuming LHF flow and using Eq. (23). A phase density ratio of 846 was used in the calculations, which is comparable to present test conditions. It can be seen that mixture fraction decreases only 1 percent as the liquid volume fraction varies by a factor of ten, from 1 to 0.1. Thus, all the results illustrated in Fig. 29 represent mixture fractions greater than 0.99. If the LHF approximation is not valid, with liquid velocities greater than gas velocities, the reduction of f would be even smaller. These findings suggest that mixing is much slower for liquid injection, at present conditions, than would be observed for single-phase flows where $f_c \sim 0.03$ at $x/d = 150$ (Shearer et al., 1979).

Table 5. Relationship Between Mixture Fraction and Liquid Volume Fraction^a

f	α_f
1.000	1.000
0.9999	0.922
0.9990	0.541
0.9900	0.105
0.9000	0.011

^a Under the LHF approximation with $\rho_0 / \rho_\infty = 846$.

Another factor that should be considered when interpreting these results is the effect of turbulent fluctuations. Time-averaged absorption measurements are processed to yield apparent time-averaged liquid volume fractions. However, due to the nonlinearity of radiation absorption, this estimate is biased, yielding a lower value of mean liquid volume fraction than the actual value. Preliminary assessment of this effect for our test conditions suggests potential effects of bias only on the order of 5 percent. Computations using a stochastic radiation absorption analysis, similar to Gore and Faeth (1986), will be undertaken subsequently to provide a more definitive evaluation of effects of turbulent fluctuations on estimates of liquid volume fractions.

Figures 30 and 31 are illustrations of radial profiles of liquid volume fractions for the case 2 and 3 jets. Profiles are illustrated for $x/d = 25, 50, 100$ and 150 . The measurements are normalized by the centerline values and plotted as a function of r/x , which is the usual similarity variable for turbulent jets (Wyganski and Fiedler, 1969). The main feature of these results is the relative narrowness of the profiles, which only extend to r/x on the order of 0.02. Most scalar properties in single-phase jets would spread to values of r/x more than an order of magnitude larger than this. The sensitivity of liquid volume fraction to mixture fraction, mentioned earlier, is a major factor in this observation, e.g., profiles of mixture fraction are much wider based on Eq. (23). The extended penetration of the liquid core is another factor. The implications of these findings will be better understood once LHF computations have been completed for present test conditions.

3.5 Summary

Similar to the particle-laden jet study, it is premature to draw any firm conclusions concerning results obtained to date. The Littaye (1943) criterion for the atomization regime boundary was reasonably effective thus far, and should be helpful for selecting test conditions for other injector sizes. Present results also suggest an extended all-liquid core in the atomization breakup regime, similar to the findings of Hiroyasu et al. (1982) and Chehroudi et al. (1985). The radiation absorption system has been satisfactorily developed.

Remaining experimental work for the first phase of the liquid-jet study involves completion of absorption measurements as well as LDA measurements of initial conditions and gas entrainment rates, for the 9.5 mm injector. All these measurements must also be completed, along with flow visualization, for a 20 mm injector (which is currently being fabricated) in order to examine effects of scale. Based on these results, we may also carry out additional tests with a smaller diameter injector, in order to resolve the far field of the flow.

Predictions using the LHF approximation are relatively straight-forward for these flows, once initial conditions are known. The main problem anticipated for these calculations is the large density ratio of the present flows, which is likely to cause difficulties in obtaining stable and converged computations.

Subsequent theoretical and experimental work will involve measurements with higher gas densities. We will also evaluate the potential optical accessibility of the drop-containing shear layer, when LDA measurements of entrainment are made, to see if phase-Doppler measurements of drop size and velocity distributions are feasible.

4. SUMMARY OF INVESTIGATION

4.1 Articles and Papers

- Faeth, G.M. (1986) Spray atomization and combustion. AIAA Paper No. 86-0136.
- Faeth, G.M. (1986) Turbulence/drop interactions in sprays. Central States Section of the Combustion Institute, Pittsburgh.
- Faeth, G.M. (1986) Heat and mass transfer in flames. Eighth Internal Heat Transfer Conference, Vol. 1, pp. 151-160, Hemisphere Publishing Corp., New York, 1986.
- Faeth, G.M. (1986) Mixing, transport and combustion in sprays. Prog. Energy Combust. Sci., submitted.
- Parthasarathy, R.N. and Faeth, G.M. (1986) Structure of particle-laden water jets in still water. Int. J. Multiphase Flow, in preparation.

4.2 Participants

G.M. Faeth, Principal Investigator

R.N. Parthasarathy, Graduate Assistant, Doctoral Candidate, University of Michigan

A. Sagar, Graduate Assistant, M.S., University of Michigan, September 1986

G. Ruff, Graduate Assistant, pre Ph.D., University of Michigan.

4.3 Oral Presentations

G.M. Faeth, "Dilute Noncombusting and Combusting Sprays," invited presentation, U.S. Army Workshop on Two-Phase Flows, Imperial College, London, October 1985.

G.M. Faeth, "Spray Atomization and Combustion," invited paper, AIAA Aerospace Sciences Meeting, Reno, NV, January 1986.

G.M. Faeth, "Spray Combustion," invited presentation, NASA Marshall Space Flight Center, Huntsville, AL, February 1986.

G.M. Faeth, "Turbulent Dispersion in Dispersed Multiphase Flows," invited seminar, Department of Mechanical Engineering, University of Illinois at Chicago, Chicago, IL, April 1986.

R.N. Parthasarathy, "Turbulent Condensing Bubbly Jets," seminar, Department of Aerospace Engineering, The University of Michigan, Ann Arbor, MI, April 1986.

G.M. Faeth, "Turbulence/Drop Interactions in Sprays," invited paper, Technical Meeting, Central States Section of the Combustion Institute, NASA-LERC, Cleveland, OH, May 1986.

G.M. Faeth, "Heat and Mass Transfer in Flames," invited keynote lecture, Eighth International Heat Transfer Conference, San Francisco, CA, August 1986.

REFERENCES

- Adam, J.R., Linblad, N.R. and Hendricks, C.D. (1968) The collision, coalescence, and disruption of water droplets. J. Appl. Phys. 39, 5173-5180.
- Al Tawee, A.M. and Landau, J. (1977) Turbulence modulation in two-phase jets. Int. J. Multiphase Flow 3, 341-351.
- Bilger, R.W. (1976) Turbulent jet diffusion flames. Prog. Energy Combust. Sci. 1, 87-109.
- Bilger, R.W. (1977) Reaction rates in diffusion flames. Comb. Flame 30, 277-284.
- Bracco, F.V. (1983) Structure of high-speed full-cone sprays. Recent Advances in Gas Dynamics (C. Casci, ed.), Plenum Publishing Corp., New York.
- Brazier-Smith, P.R., Jennings, S.G. and Latham, J. (1972) The interaction of falling water drops: coalescence. Proc. Roy. Soc. London A 326, 393-408.
- Chatwani, A.V. and Bracco, F.V. (1985) Computation of dense spray jets. Third International Conference on Liquid Atomization and Spray Systems, Imperial College, London.
- Chehroudi, B., Onuma, Y., Chen, S.-H. and Bracco, F.V. (1985) On the intact core of full-cone sprays. SAE Paper 850126.
- Chen, L-D. and Faeth, G.M. (1982) Condensation of submerged vapor jets in subcooled liquids. J. Heat Transfer 104, 774-780.
- Chen, L-D. and Faeth, G.M. (1983) Structure of turbulent reacting gas jets submerged in liquid metals. Comb. Sci. Tech. 31, 277-296.
- Clift, R., Grace, J.R. and Weber, M.E. (1978) Bubbles, Drops and Particles, Academic Press, New York, 185-319.
- Delichatios, M.A. and Probstein, R.F. (1976) The effect of coalescence on the average drop size in liquid-liquid dispersions. Ind. Engr. Chem. Fundam. 15, 134-138.
- Faeth, G.M. (1977) Current status of droplet and liquid combustion. Prog. Energy Combust. Sci. 3, 191-224.
- Faeth, G.M. (1983) Evaporation and combustion in sprays. Prog. Energy Combust. Sci. 9, 1-76.
- Faeth, G.M. (1983a) Recent advances in modeling particle transport properties and dispersion in turbulent flow. Proc. ASME-JSME Thermal Engr. Joint Conf., Vol. II, 517-534.
- Faeth, G.M. (1986) Spray atomization and combustion. AIAA Paper No. 86-0136.
- Giffin, E. and Muraszew, A. (1953) The Atomization of Liquid Fuels, John Wiley and Sons, New York.

- Gomi, H. and Hasegawa, K.-I. (1984) Measurement of the liquid phase mass in gas-liquid sprays by X-ray attenuation. Int. J. Multiphase Flow 10, 653-662.
- Gore, J.P. and Faeth, G.M. (1986) Structure and spectral radiation properties of turbulent ethylene/air diffusion flames. Twenty-First Symposium (International) on Combustion, The Combustion Institute, Pittsburgh, in press.
- Gosman, A.D. and Ioannides, E. (1981) Aspects of computer simulation of liquid-fueled combustors, AIAA Paper No. 81-0323.
- Gunn, R. (1965) Collision characteristics of freely falling water drops. Science 150, 695-701.
- Hiroyasu, H. and Kadota, T. (1974) Fuel droplet size distribution in diesel combustion chamber. SAE Paper 740715.
- Hiroyasu, H., Shimizu, M. and Arai, M. (1982) The breakup of a high speed jet in a high pressure gaseous atmosphere. Proceedings of the 2nd International Conference on Liquid Atomization and Spray Systems, Madison, Wisconsin.
- Jeng, S.-M., Chen, L.-D. and Faeth, G.M. (1982) The structure of buoyant methane and propane diffusion flames. Nineteenth Symposium (International) on Combustion, The Combustion Institute, Pittsburgh, 349-358.
- Jeng, S.-M. and Faeth, G.M. (1984) Species concentrations and turbulence properties of buoyant methane diffusion flames. J. Heat Transfer 106, 771-727.
- Jeng, S.-M. and Faeth, G.M. (1984a) Predictions of mean and scalar properties in turbulent propane diffusion flames. J. Heat Transfer 106, 891-893.
- Lai, M.-C., Jeng, S.-M. and Faeth, G.M. (1985) An Investigation of turbulent fires on vertical walls: wall plume structure. Report to National Bureau of Standards, The Pennsylvania State University, University Park, Pennsylvania.
- Lai, M.-C., Jeng, S.-M. and Faeth, G.M. (1985a) Structure of turbulent adiabatic wall plumes. National Heat Transfer Conference, Denver.
- Langmuir, I. (1948) The production of rain by a chain reaction in cumulus clouds at temperatures above freezing. J. Meteor. 5, 175-192.
- Littaye, G. (1943) Sur une theorie de la pulverisation des jets liquides. Compt. Rend. 217, 99.
- Lockwood, F.C. and Naguib, A.S. (1975) The prediction of the fluctuations of properties of free, round jet, turbulent diffusion flames. Comb. Flame 24, 109-124.
- Mao, C.-P., Szekely, G.A., Jr. and Faeth, G.M. (1980) Evaluation of a locally homogeneous flow model of spray combustion. J. Energy 4, 78-87.
- Mao, C.-P., Wakamatsu, Y. and Faeth, G.M. (1981) A simplified model of high pressure spray combustion. Eighteenth Symposium (International) on Combustion, The Combustion Institute, Pittsburgh, 337-347.

- Martinelli, L., Reitz, R.D. and Bracco, F.V. (1983) Comparisons of computed and measured dense spray jets. AIAA Progress in Astronautics and Aeronautics Vol. 85.
- Miesse, C.C. (1955) Correlation of experimental data on disintegration of liquid jets. Ind. Engr. Chem. 470, 1690-1697.
- Modarress, D., Tan, H. and Elghobashi, S. (1984) Two-component LDA measurement in a two-phase turbulent jet. AIAA J. 22, 624-630.
- Odar, F. and Hamilton, W.S. (1964) Force on a sphere accelerating in a viscous fluid. J. Fluid Mech. 23, 749-766.
- Ogura, Y. and Takahashi, T. (1973) The development of warm rain in a cumulus model. J. Atmos. Sci. 30, 262-277.
- Ohba, K. (1979) Relationships between radiation transmissivity and void fraction in two-phase/dispersed flow. Tech. Rept. Osaka University 29, 245-254.
- O'Rourke, P.J. (1981) Collective drop effects on vaporizing liquid sprays. Ph.D. dissertation No. 1532-T, Princeton University.
- O'Rourke, P.J. and Bracco, F.V. (1980) Modeling of drop interactions in thick sprays and comparison with experiments. Inst. Mech. Engrs., Pub. ISBN 0 852984693, 101-116.
- Ranz, W.E. (1958) Some experiments on orifice sprays. Can. J. Chem. Engr. 36, 175-181.
- Reitz, R.D. (1978) Atomization and other breakup regimes of a liquid jet. Ph.D. Dissertation No. 1375-T, Princeton University.
- Reitz, R.D. and Bracco, F.V. (1982) Mechanism of atomization of a liquid jet. Phys. Fluids 25, 1730-1742.
- Reitz, R.D. and Bracco, F.V. (1984) Mechanisms of breakup of round liquid jets. Encyclopedia of Fluid Mechanics (N.P. Cheremisinoff, ed.), Vol. III, Chap. 11.
- Saffman, P.G. and Turner, J.S. (1956) On the collision of drops in turbulent clouds. J. Fluid Mech. 1, 16-30.
- Santoro, R.J., Semerjian, J.H., Emmerman, P.J. and Goulard, R. (1981) Optical tomography for flow field diagnostics. Int. J. Heat Mass Trans. 24, 1139-1150.
- Schrock, V.E. (1969) Two-Phase Flow Instrumentation. ASME, New York, 24-35.
- Shearer, A.J., Tamura, H. and Faeth, G.M. (1979) Evaluation of a locally homogeneous flow model of spray evaporation. J. Energy 3, 271-278.
- Shuen, J.-S., Chen, L.-D. and Faeth, G.M. (1983) Evaluation of a stochastic model of particle dispersion in a turbulent round jet. AIChE J. 29, 167-170.
- Shuen, J.-S., Chen, L.-D. and Faeth, G.M. (1983a) Predictions of the structure of turbulent, particle-laden, round jets. AIAA J. 21, 1483-1484.

- Shuen, J.-S., Solomon, A.S.P., Zhang, Q.-F. and Faeth, G.M. (1985) Structure of particle-laden jets: measurements and predictions. AIAA J. 23, 396-404.
- Shuen, J.-S., Solomon, A.S.P. and Faeth, G.M. (1986) Drop-turbulence interactions in a diffusion flame. AIAA J. 24, 101-108.
- Solomon, A.S.P., Shuen, J.-S., Zhang, Q.-F. and Faeth, G.M. (1985) Structure of nonevaporating sprays: I. near-injector conditions and mean properties. AIAA J. 23, 1548-1555.
- Solomon, A.S.P., Shuen, J.-S., Zhang, Q.-F. and Faeth, G.M. (1985a) Structure of nonevaporating sprays: II. drop and turbulence properties. AIAA J. 23, 1724-1730.
- Solomon, A.S.P., Shuen, J.-S., Zhang, Q.-F. and Faeth, G.M. (1985b) Measurements and predictions of the structure of evaporating sprays. J. Heat Transfer 107, 679-686.
- Spalding, D.B. (1977) GENMIX: A General Computer Program for Two-Dimensional Parabolic Phenomena, Pergamon Press, Oxford.
- Srivastava, R.C. (1971) Size distribution of raindrops generated by their breakup and coalescence. J. Atmos. Sci. 28, 410-415.
- Sun, T.-Y. and Faeth, G.M. (1986) Structure of turbulent bubbly-jets -- I. methods and centerline properties. Int. J. Multiphase Flow 12, 99-114.
- Sun, T.-Y. and Faeth, G.M. (1986a) Structure of turbulent bubbly jets -- II. phase property profiles. Int. J. Multiphase Flow 12, 115-124.
- Sun, T.-Y., Parthasarathy, R. and Faeth, G.M. (1986) Structure of bubbly round condensing jets. J. Heat Transfer, in press.
- Swinbank, W.C. (1947) Collisions of cloud droplets. Nature 4051, 849-850.
- Taylor, G.I. (1940) Generation of ripples by wind blowing over a viscous fluid. Collected Works of G.I. Taylor, Vol. 3, 244-ff.
- Wu, K.-J., Su, C.-C., Steinberger, R.L., Santavicca, D.A. and Bracco, F.V. (1983) Measurements of the spray angle of atomizing jets. J. Fluids Engr. 105, 406-415.
- Wu, K.-J., Coghe, A., Santavicca, D.A. and Bracco, F.V. (1984) LDV measurements of drop velocity in diesel-type sprays. AIAA J. 22, 1263-1270.
- Wygnanski, I. and Fielder, H.E. (1969) Some measurements in the self-preserving jet. J. Fluid Mech. 38, 577-612.
- Zhang, Q.-F., Shuen, J.-S., Solomon, A.S.P. and Faeth, G.M. (1985) Structure of ducted particle-laden turbulent jets. AIAA J. 23, 1123-1125.

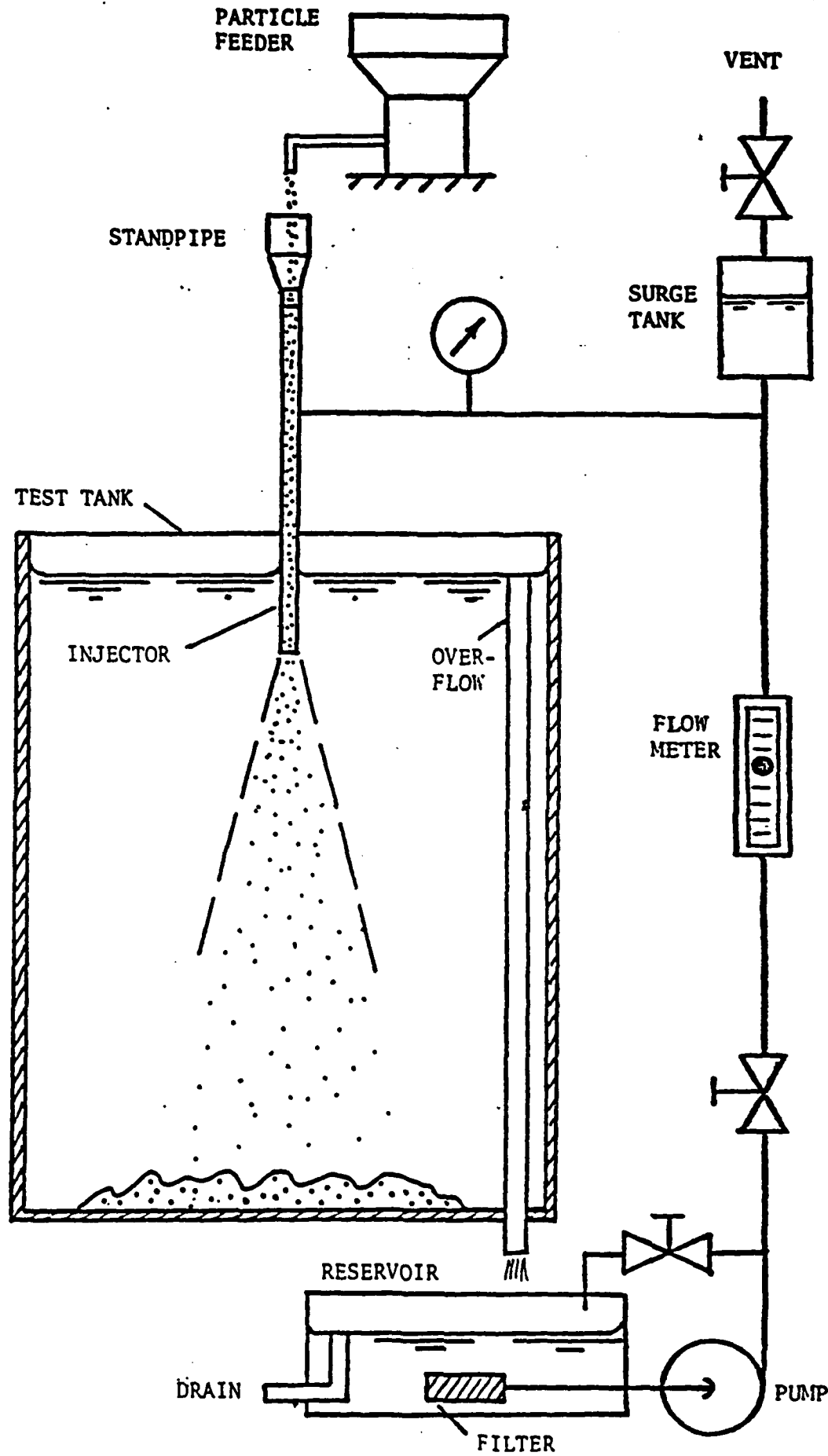


FIGURE 1. Sketch of particle-laden jet apparatus

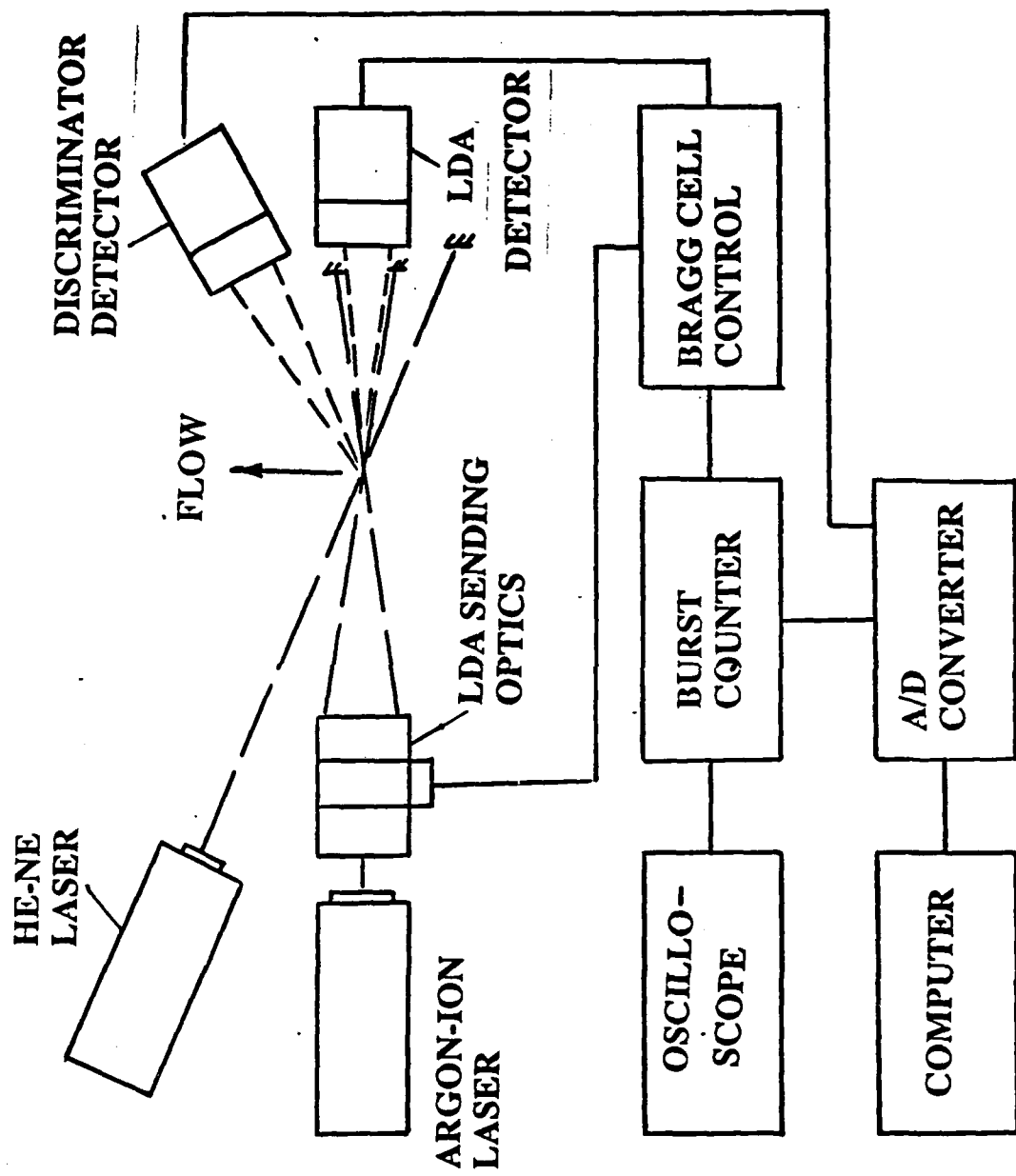


FIGURE 2. Sketch of phase-discriminating LDA

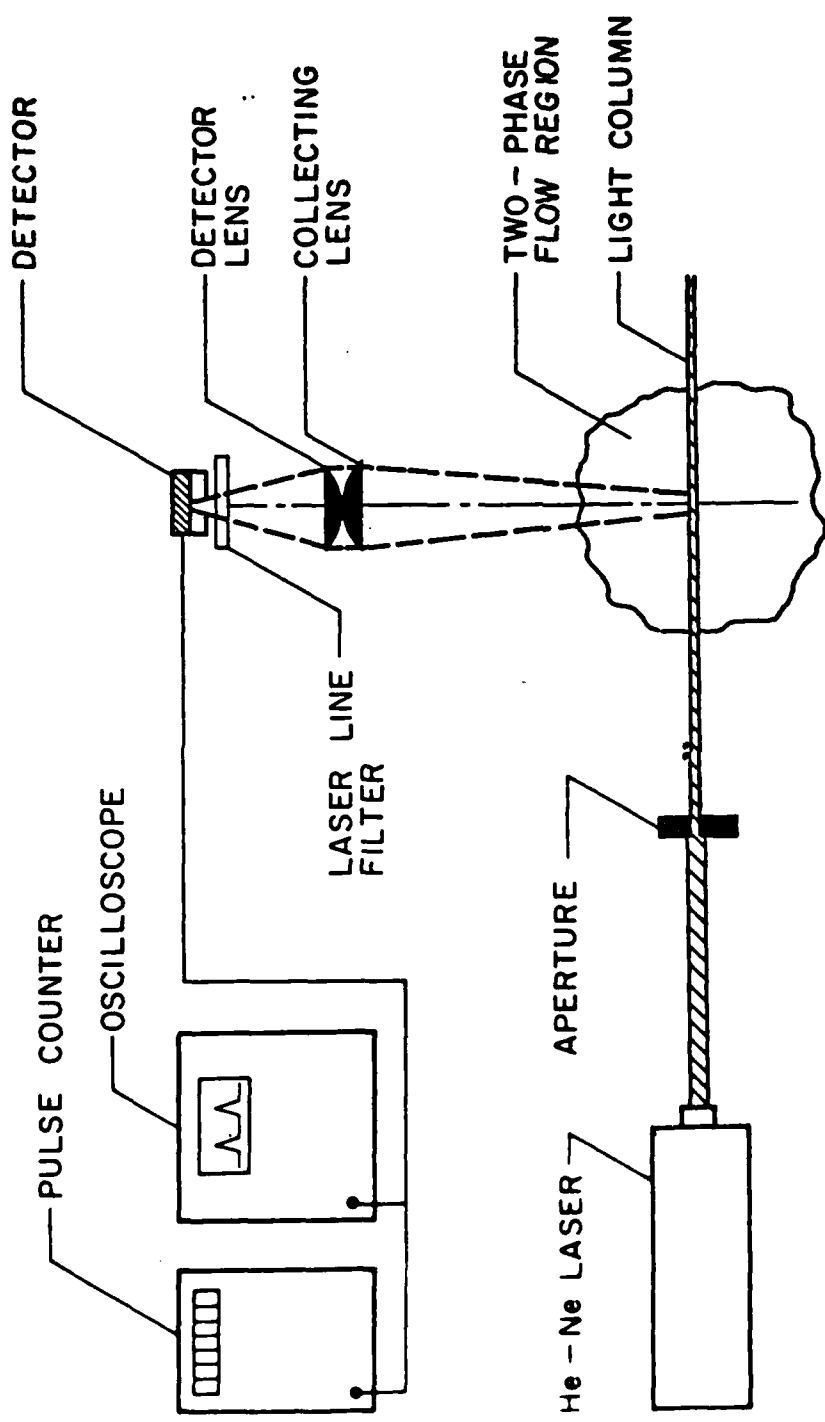


FIGURE 3. Sketch of the particle-flux measuring system

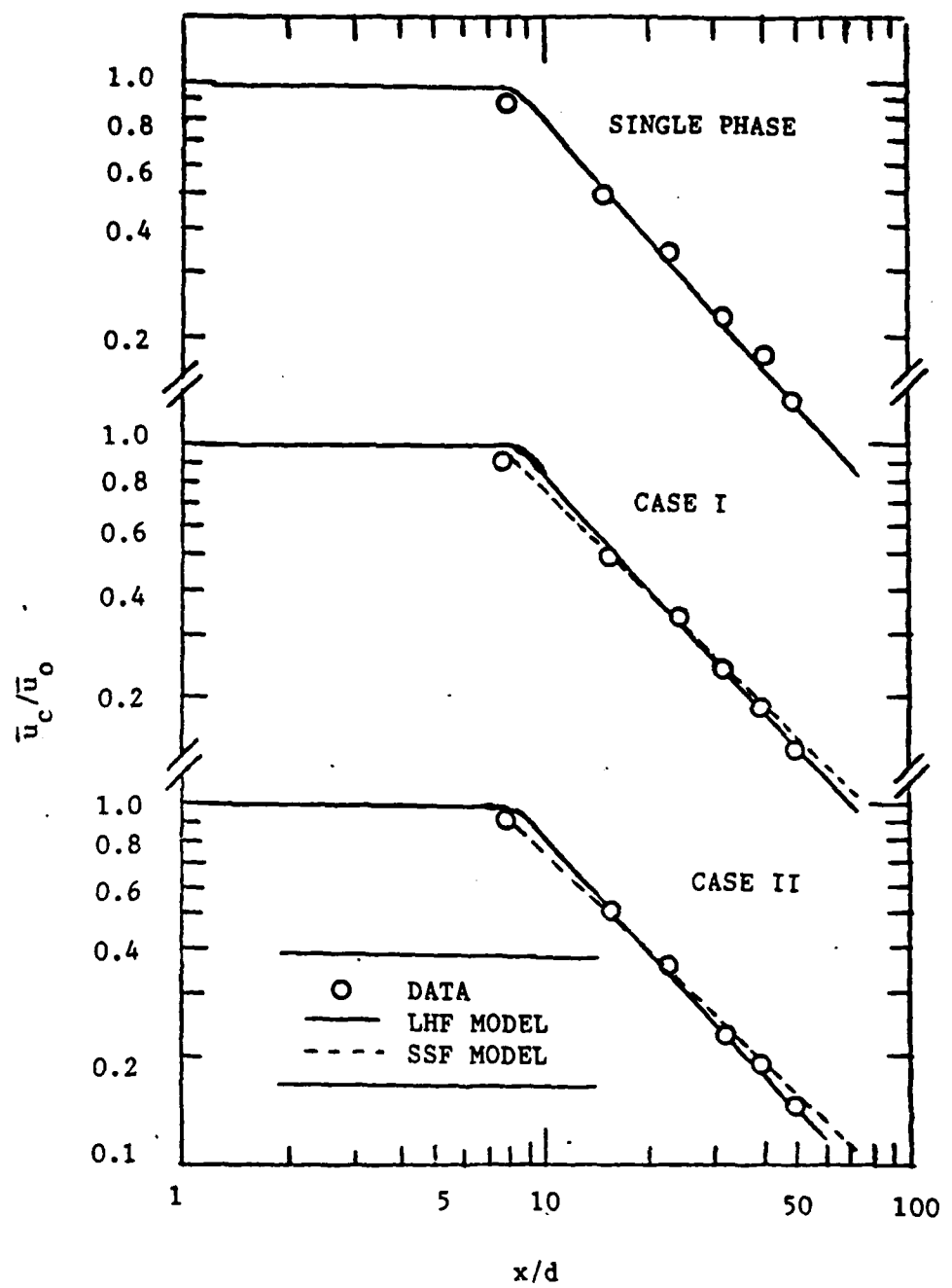


FIGURE 4. Mean liquid-phase velocities along axis

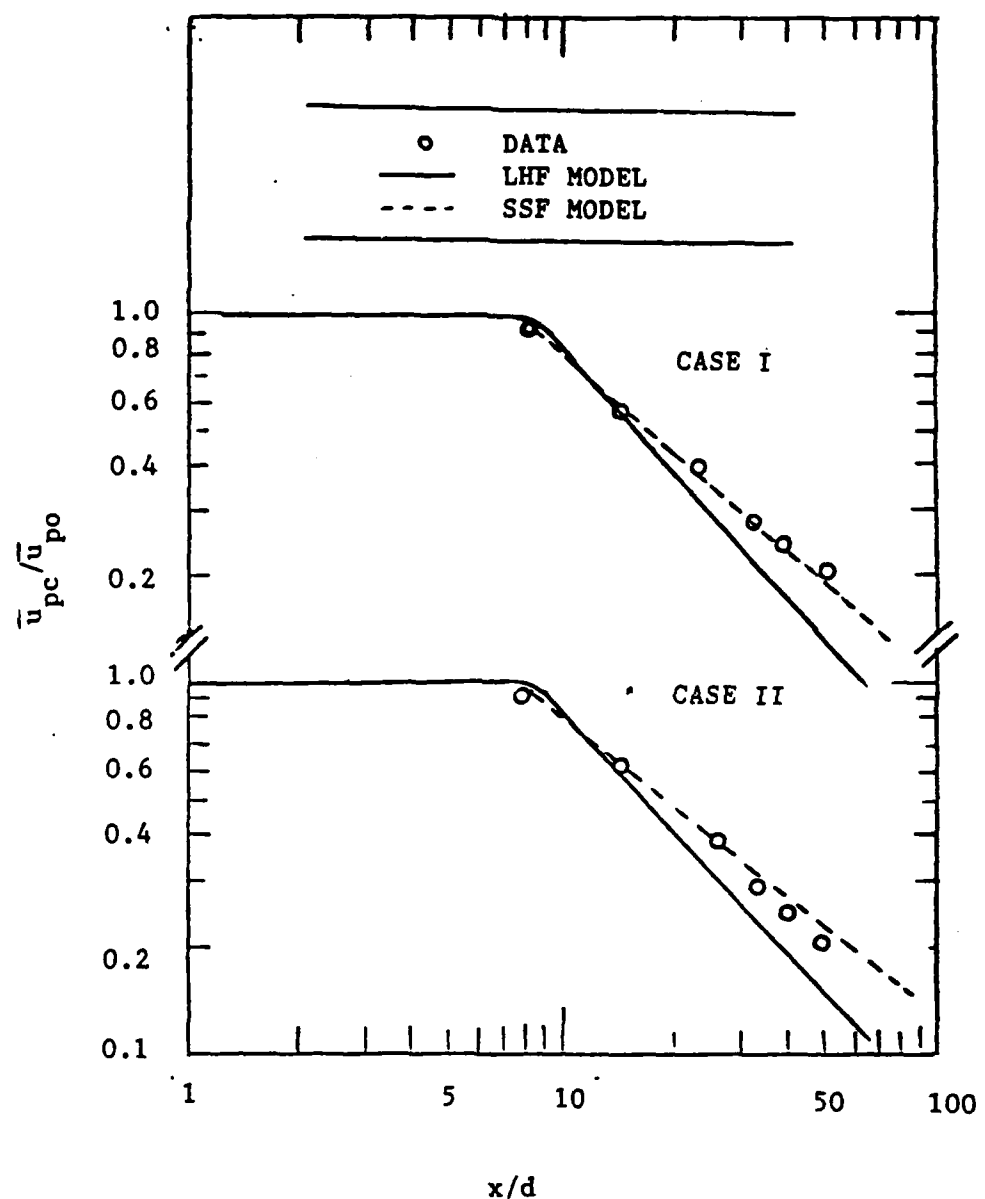


FIGURE 5. Mean particle-phase velocities along axis

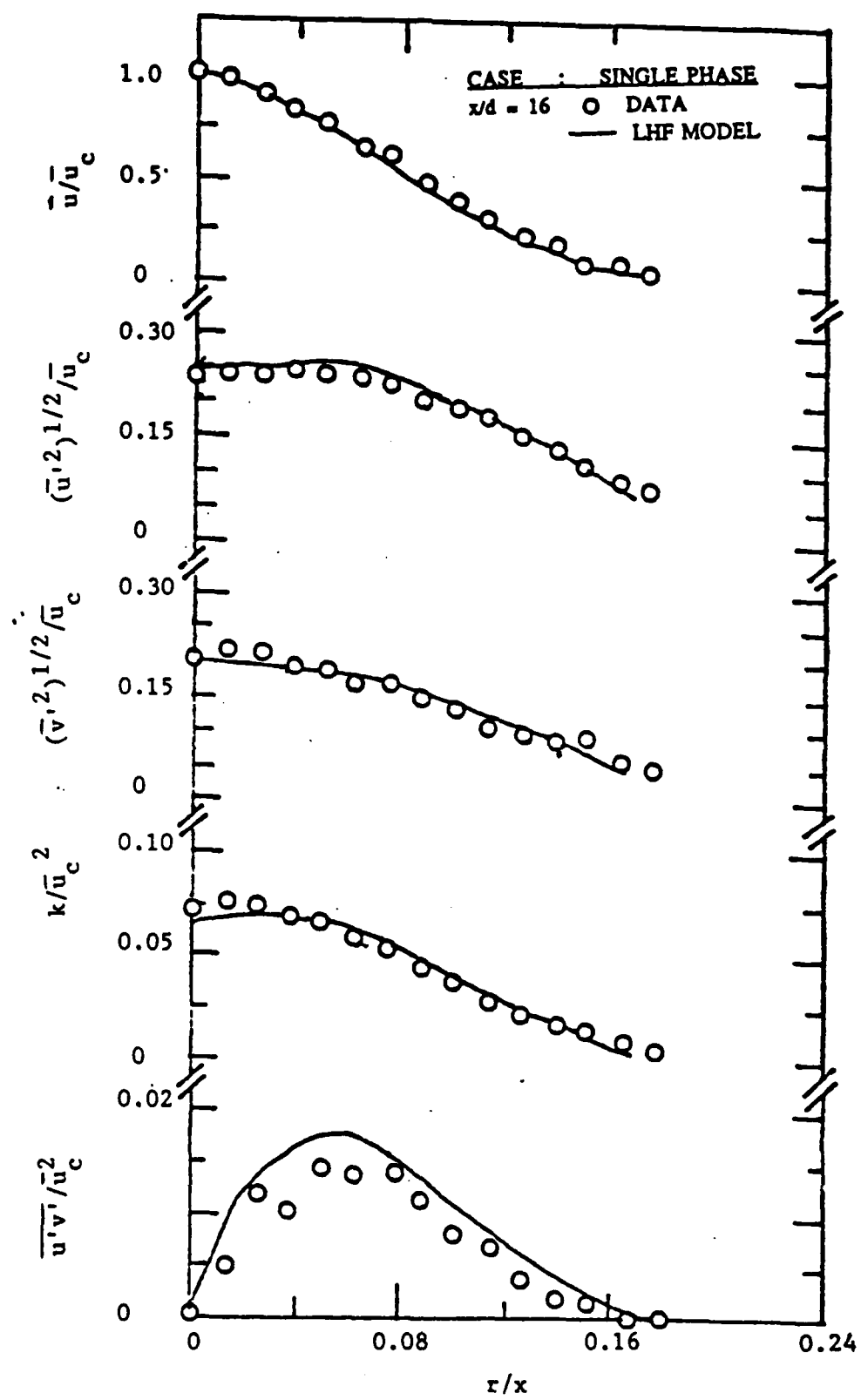


FIGURE 6. Mean and turbulent properties for the single-phase jet at $x/d = 16$

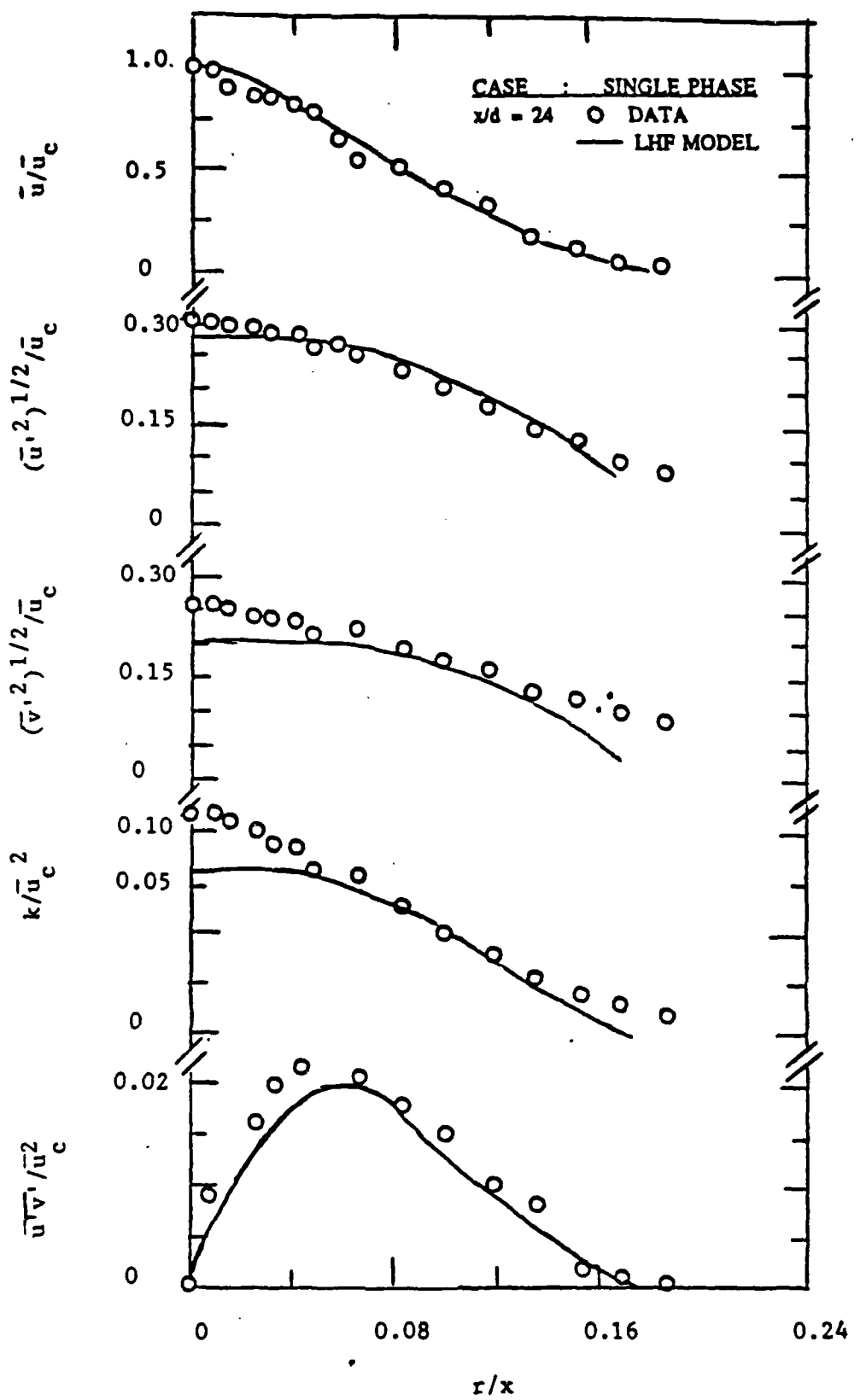


FIGURE 7. Mean and turbulent properties for the single-phase jet at $x/d = 24$

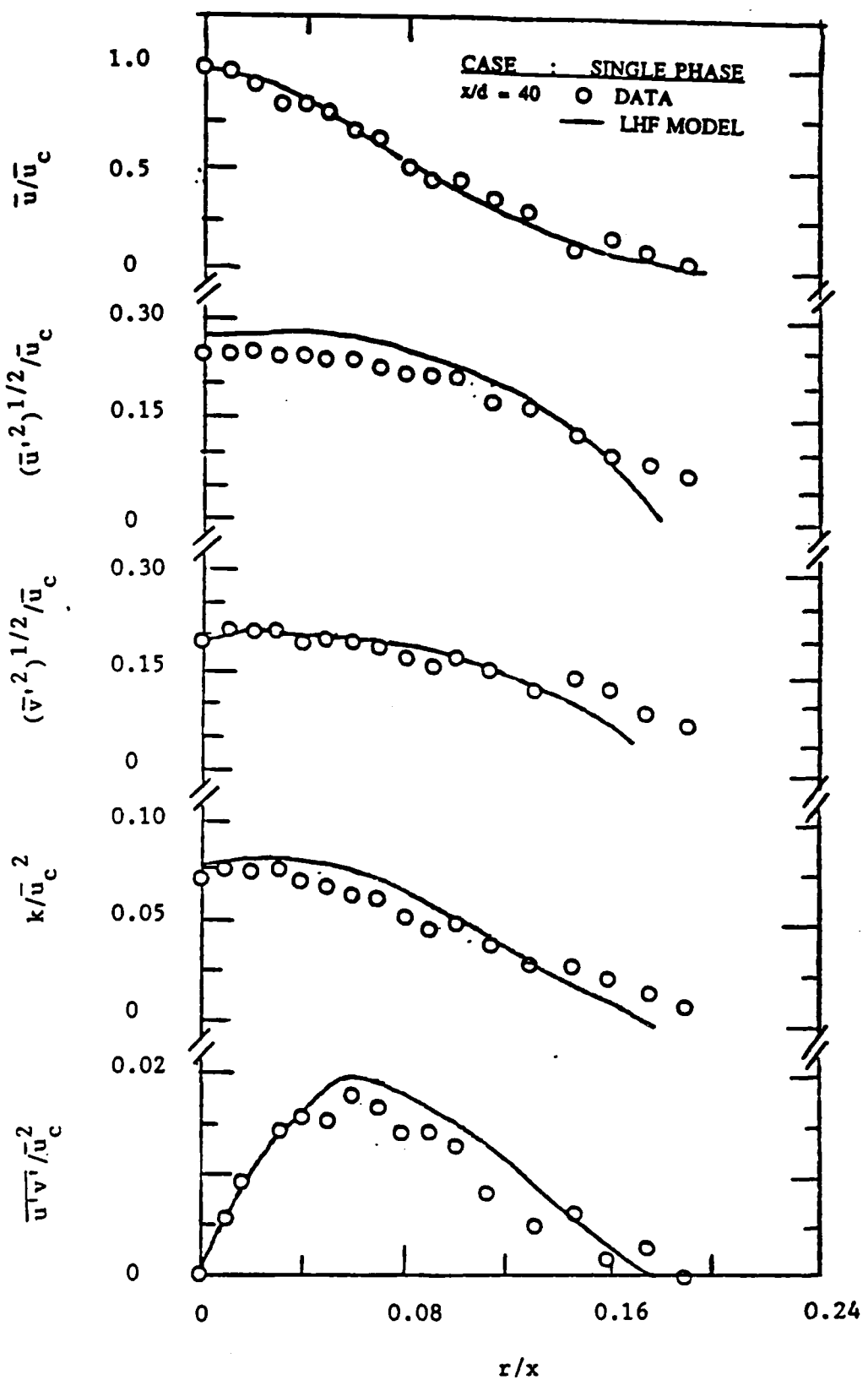


FIGURE 8. Mean and turbulent properties for the single-phase jet at $x/d = 40$

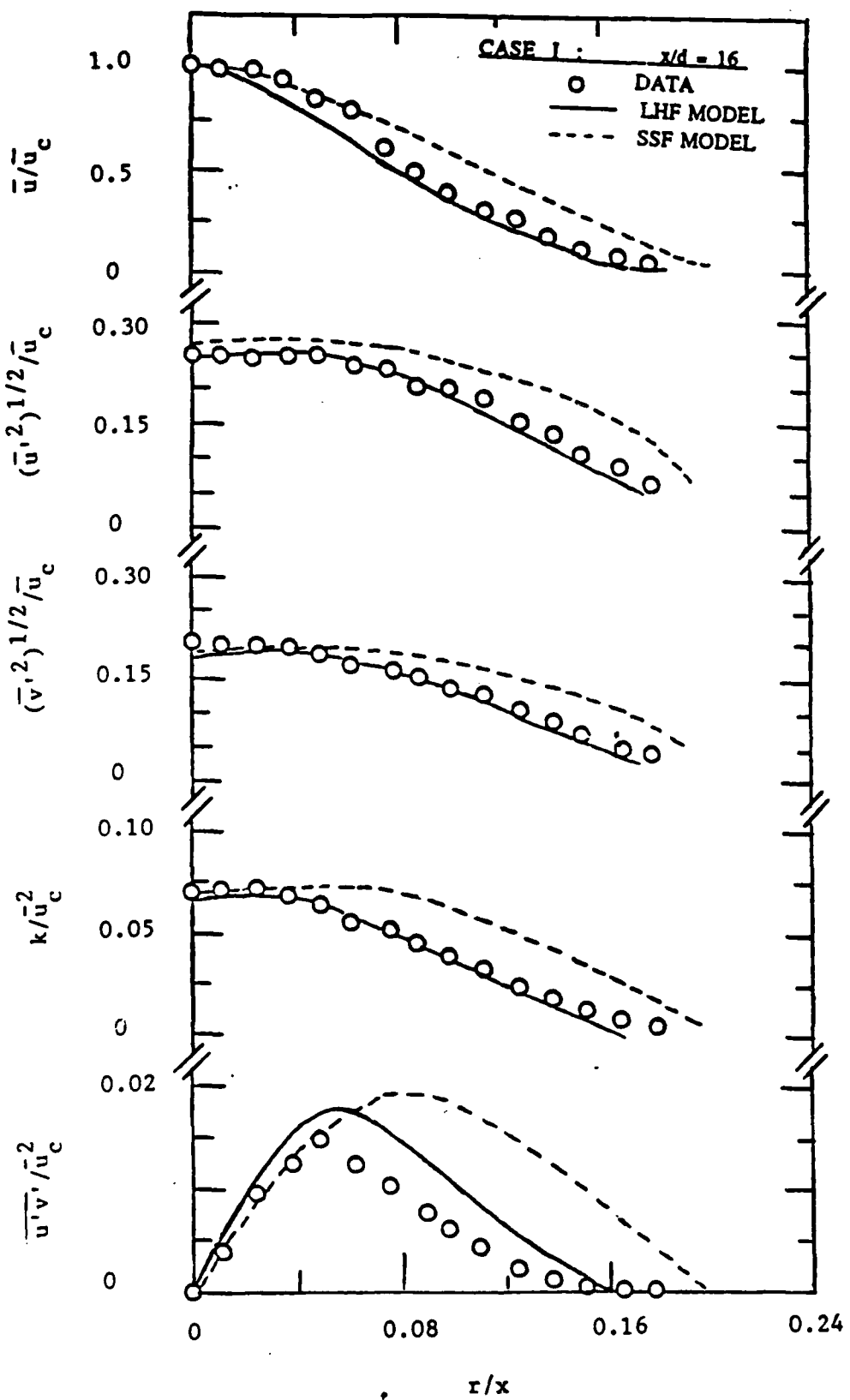


FIGURE 9. Mean and turbulent liquid-phase properties for the case I jet at $x/d = 16$

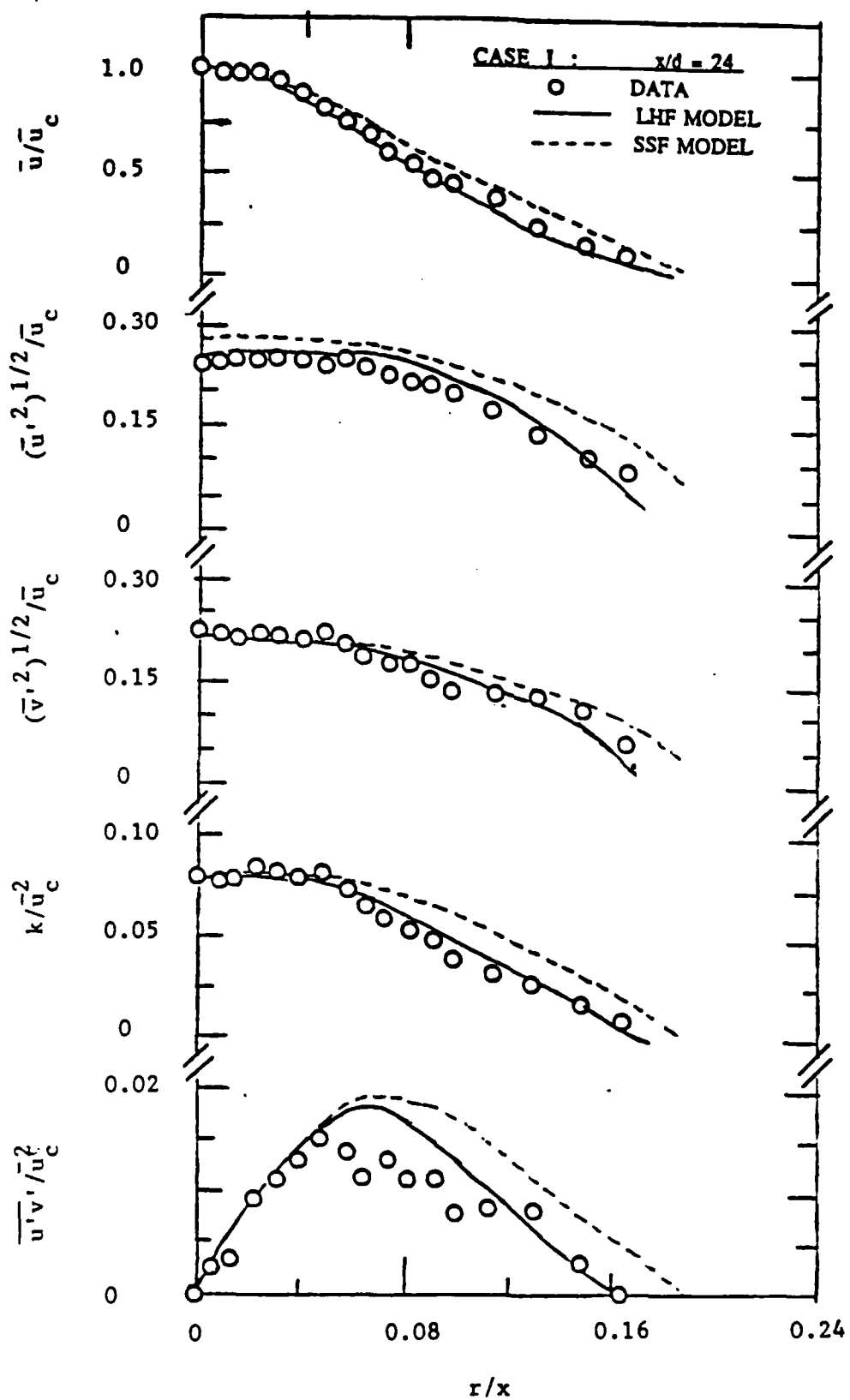


FIGURE 10. Mean and turbulent liquid-phase properties for the case I jet at $x/d = 24$

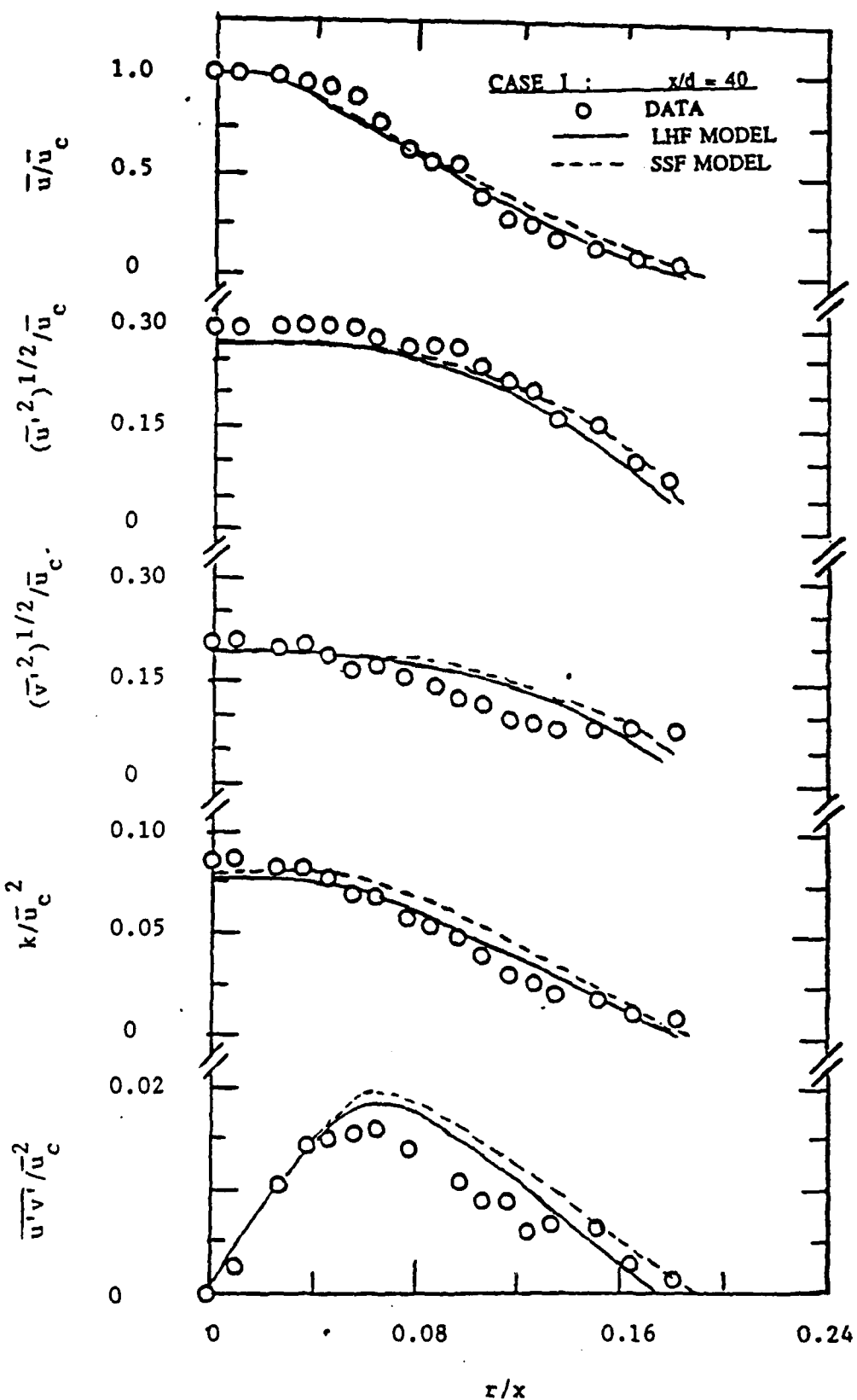


FIGURE 11. Mean and turbulent liquid-phase properties for the case I jet at $x/d = 40$

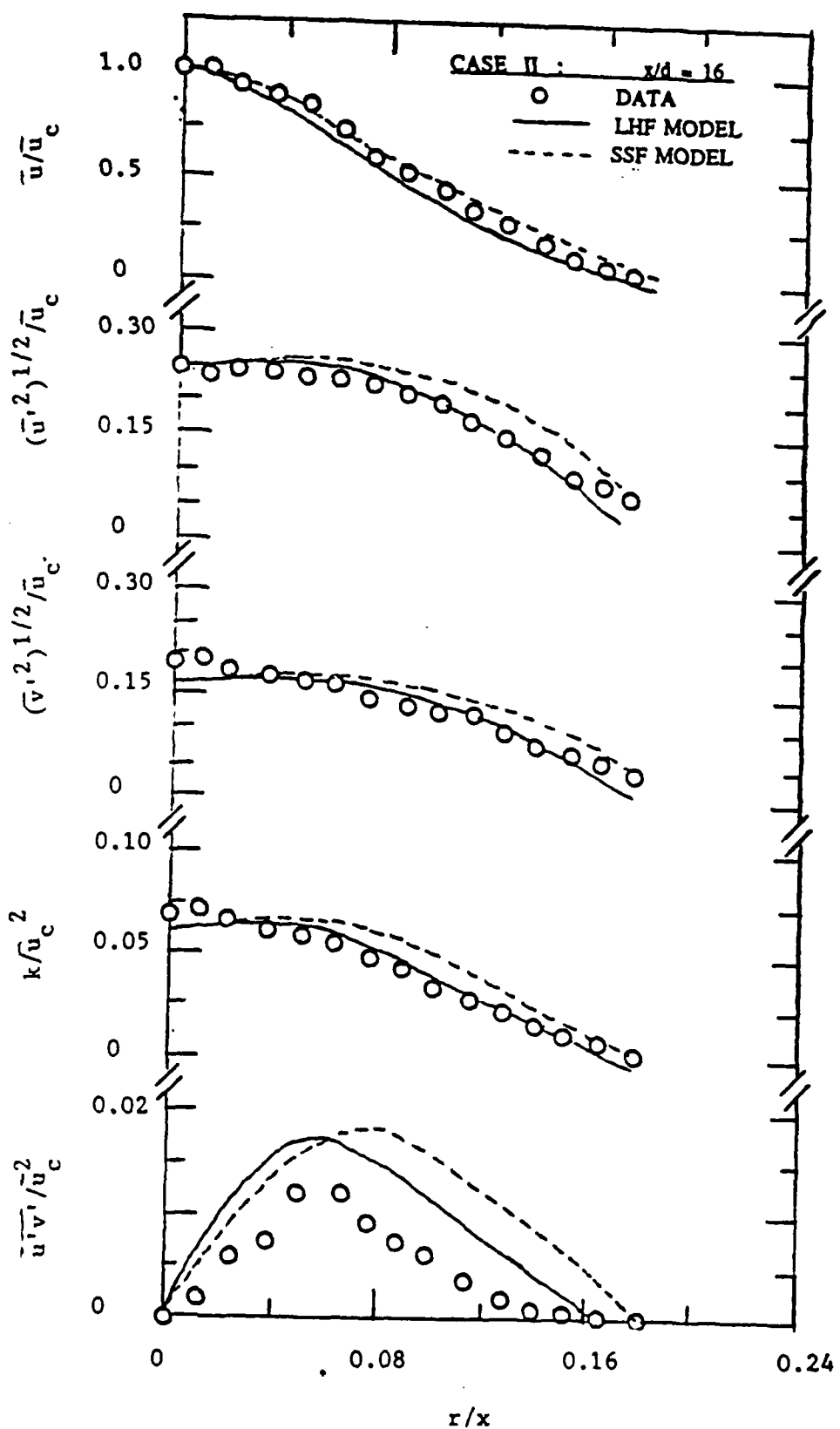


FIGURE 12. Mean and turbulent liquid-phase properties for the case II jet at $x/d = 16$

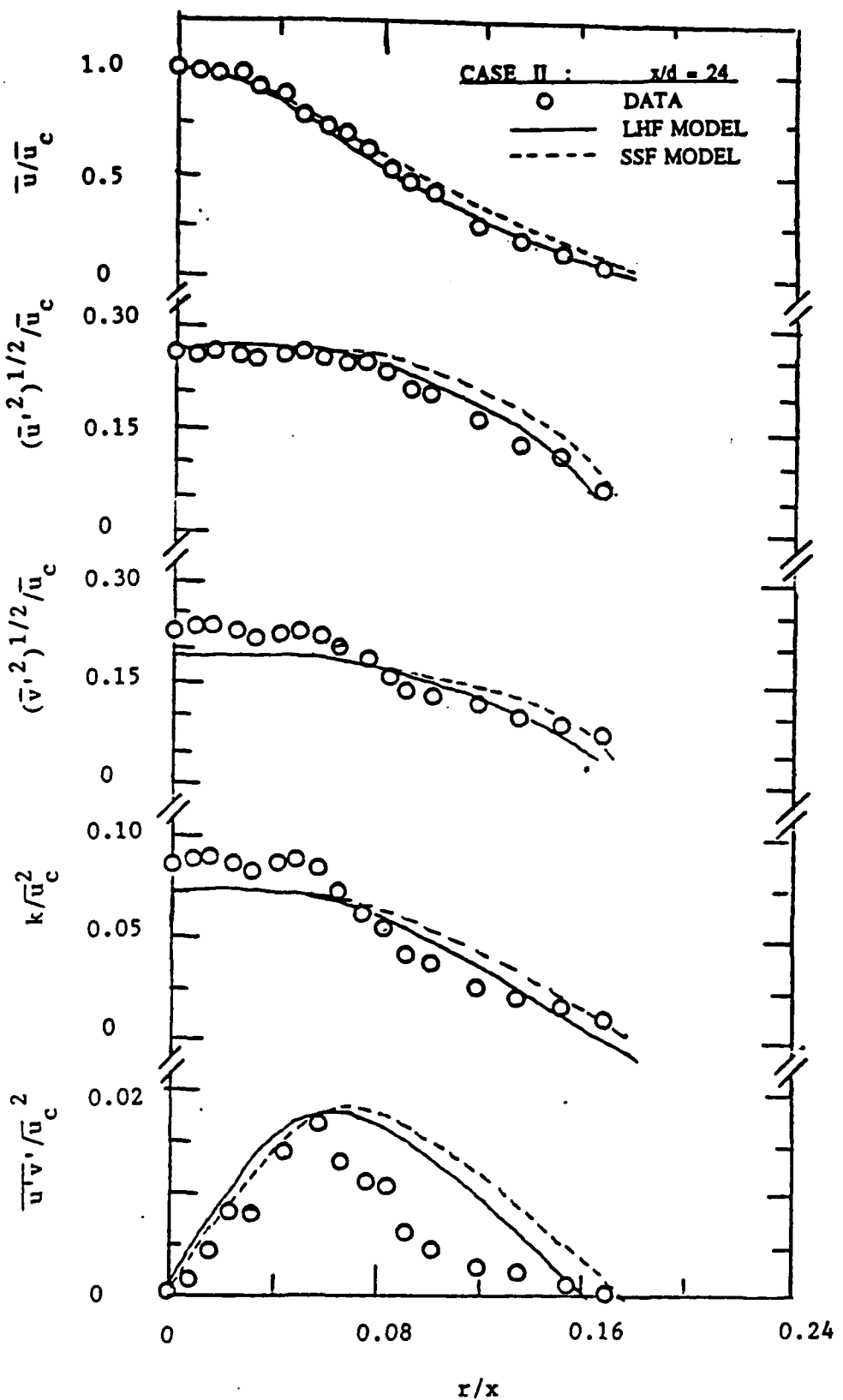


FIGURE 13. Mean and turbulent liquid-phase properties for the case II jet at $x/d = 24$

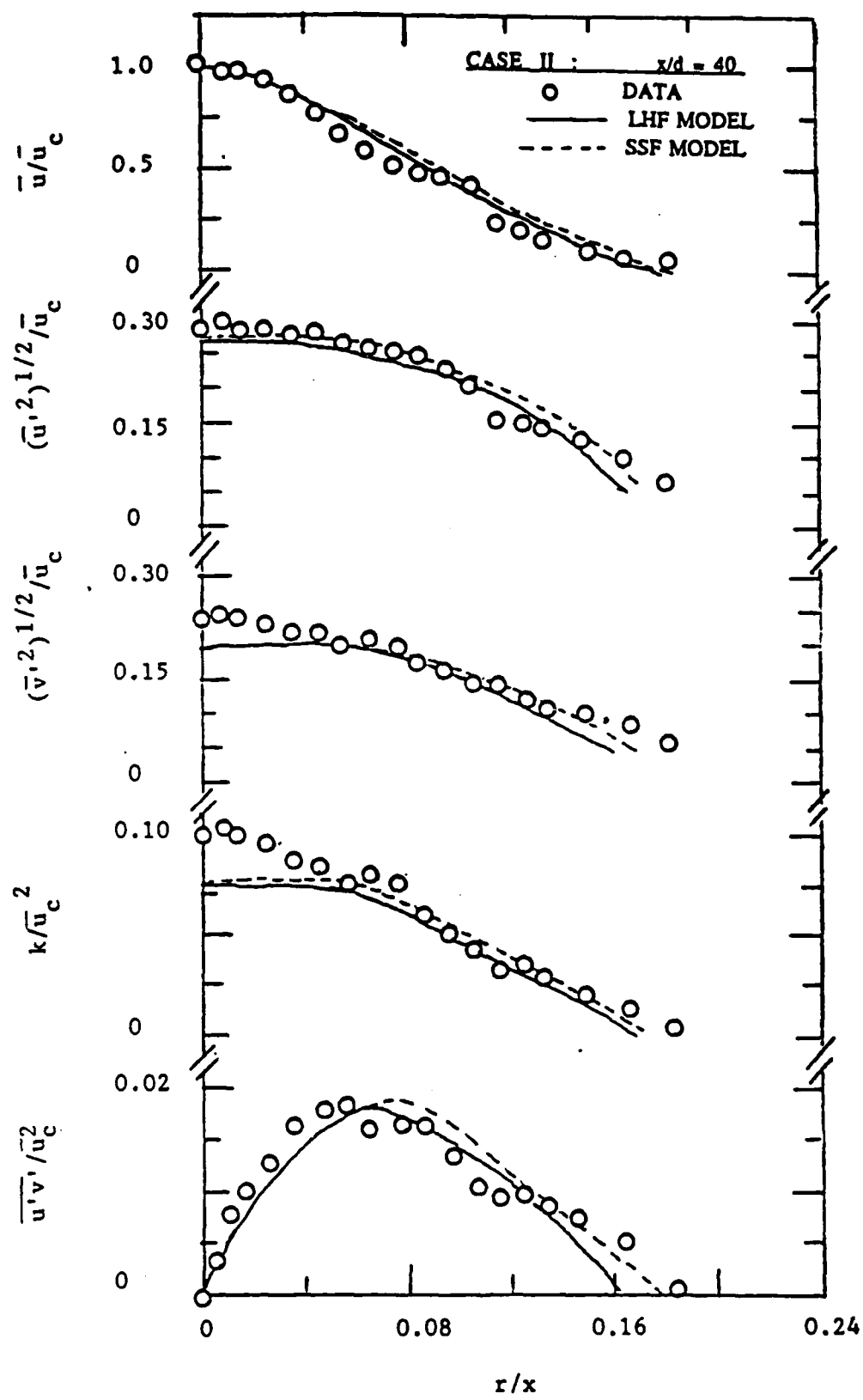


FIGURE 14. Mean and turbulent liquid-phase properties for the case II jet at $x/d = 40$

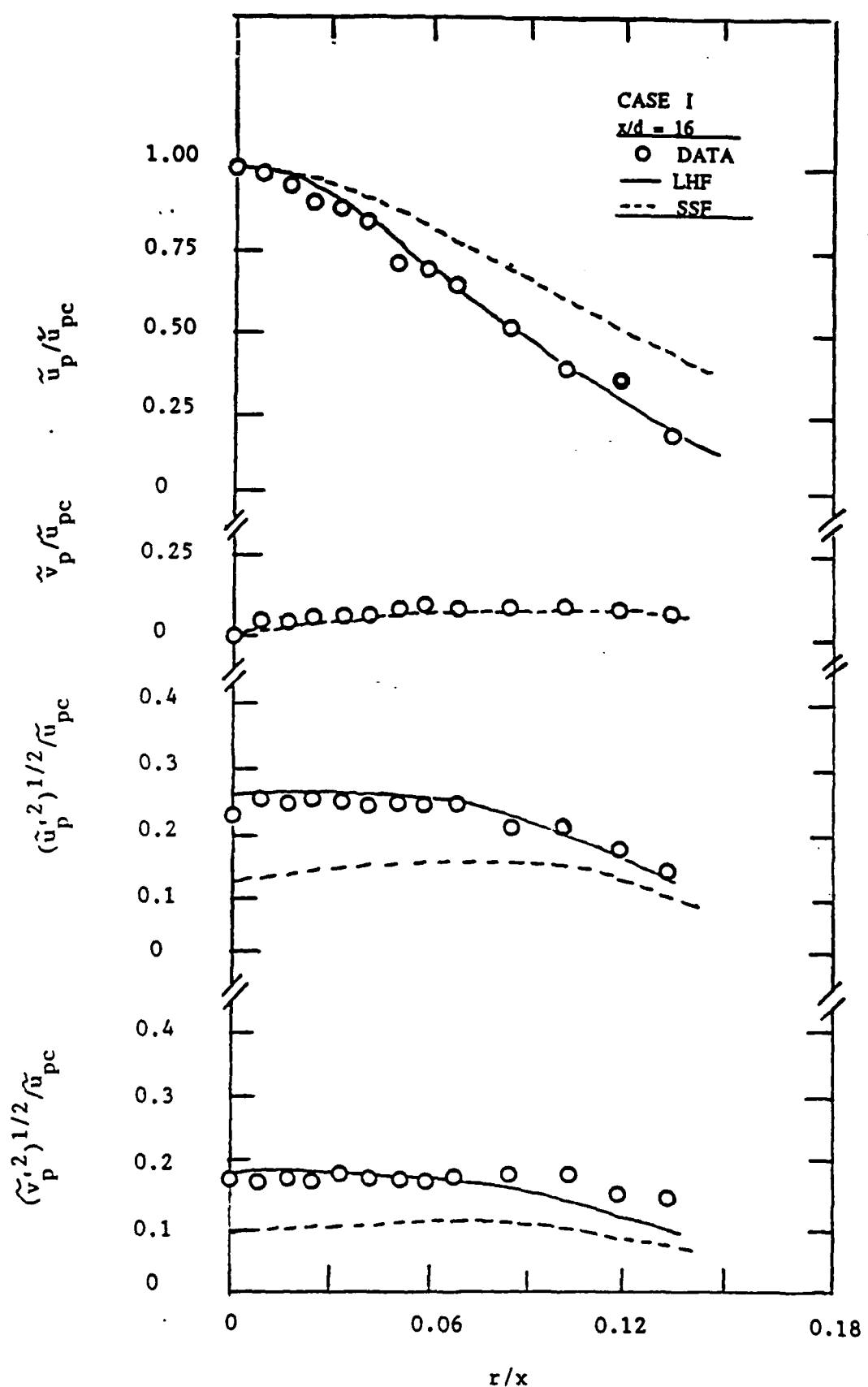


FIGURE 15. Mean and turbulent particle-phase properties for the case I jet at $x/d = 16$

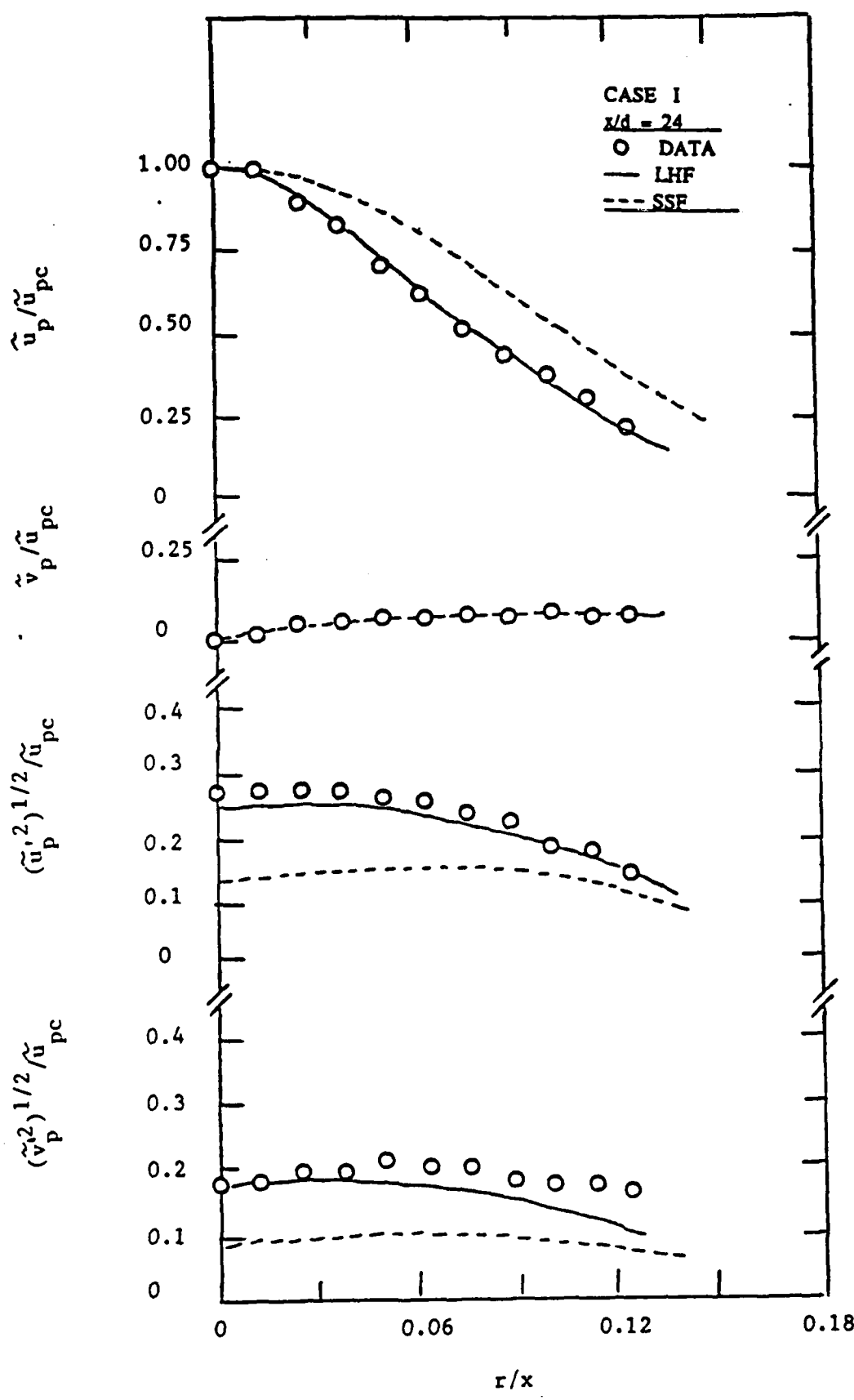


FIGURE 16. Mean and turbulent particle-phase properties for the case I jet at $x/d = 24$

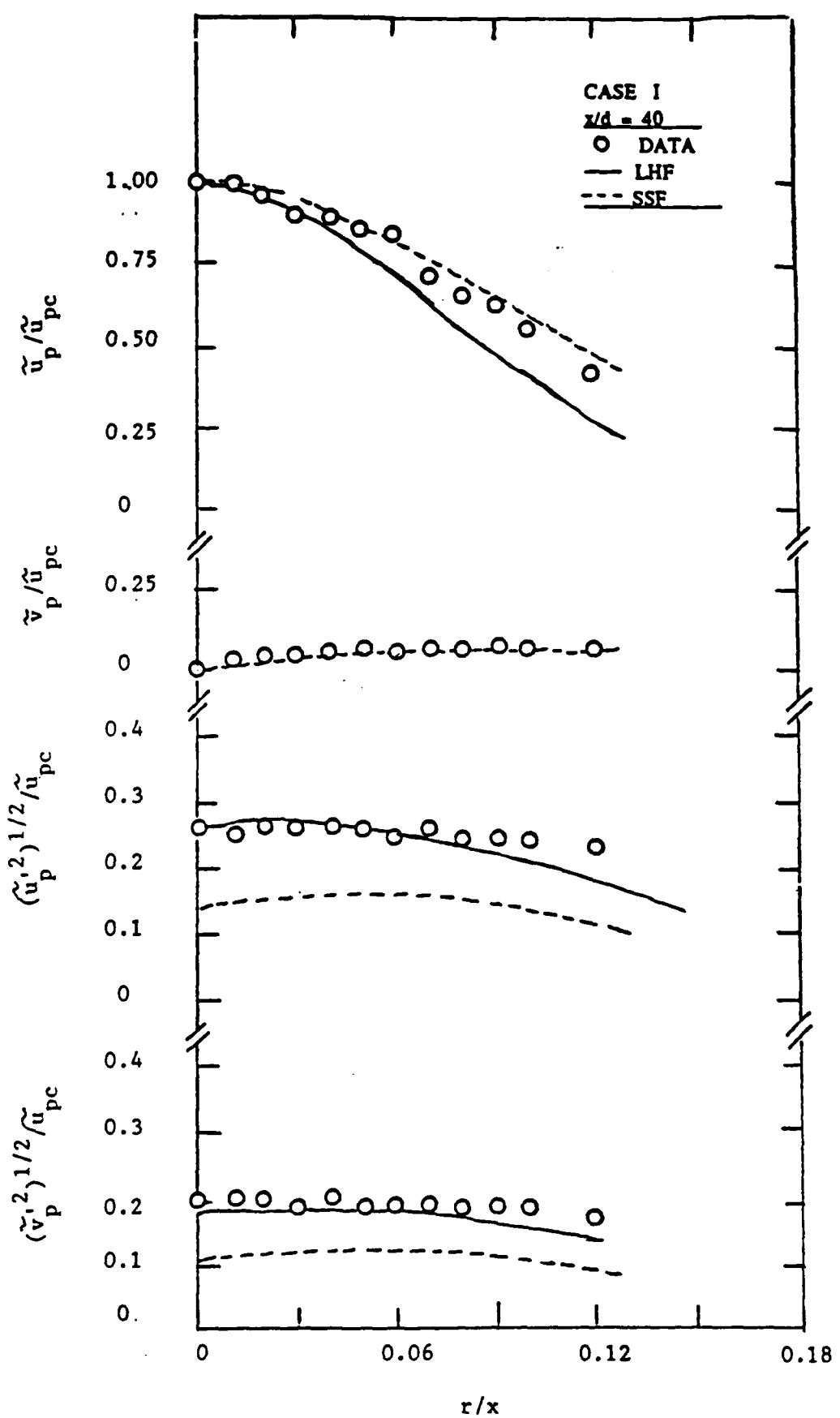


FIGURE 17. Mean and turbulent particle-phase properties for the case I jet at $x/d = 40$

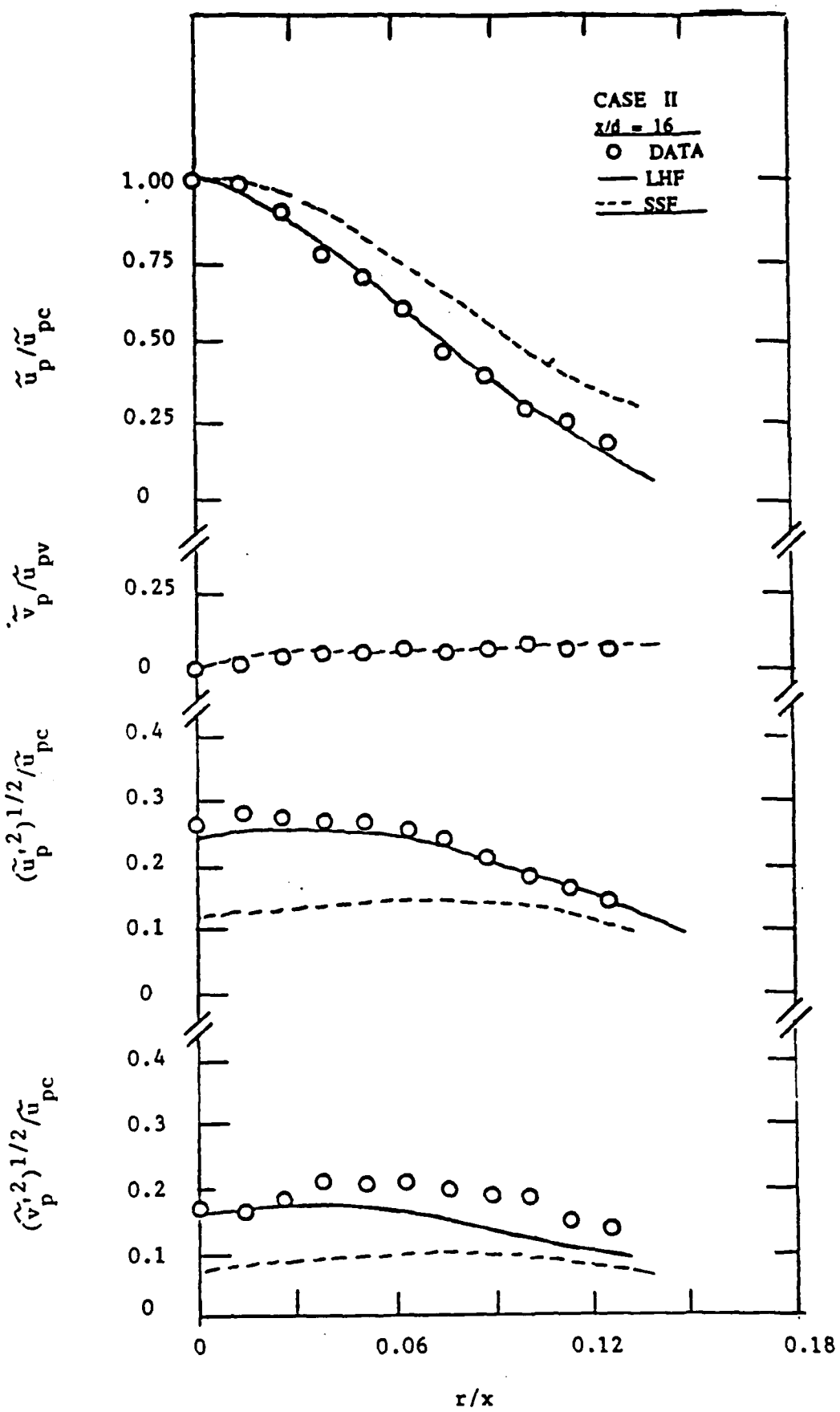


FIGURE 18. Mean and turbulent particle-phase properties for the case II jet at $x/d = 16$

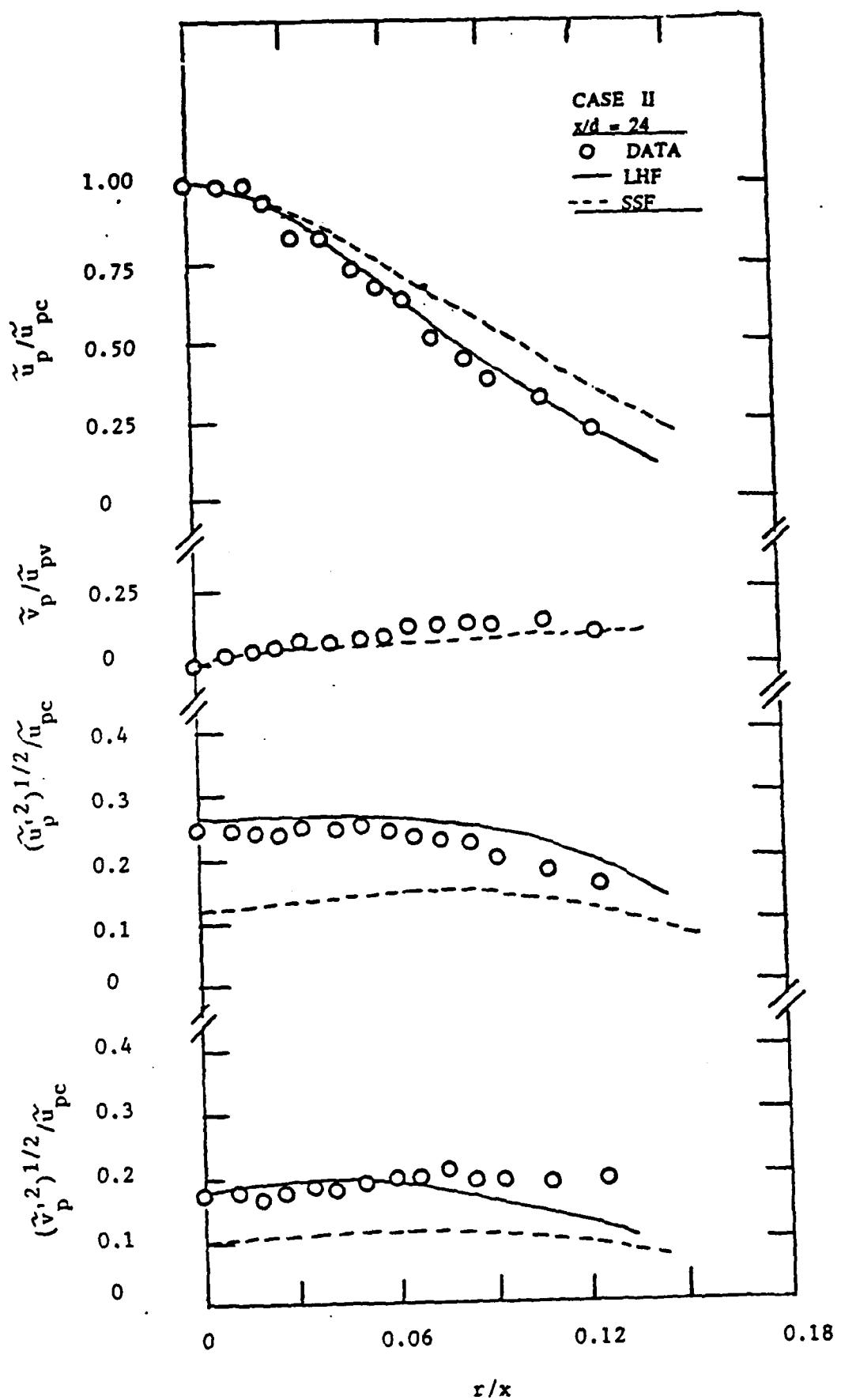


FIGURE 19. Mean and turbulent particle-phase properties for the case II jet at $x/d = 24$

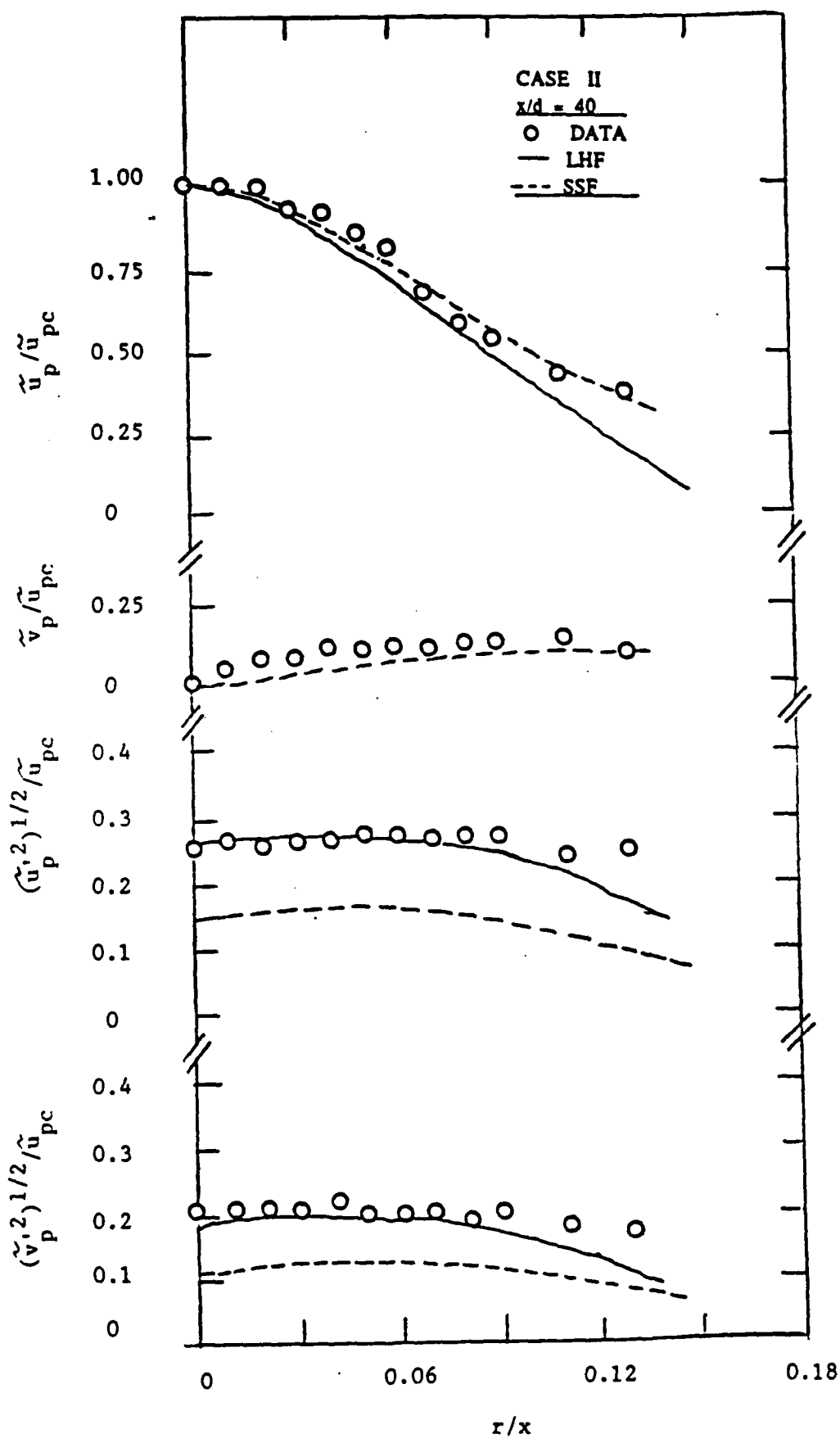


FIGURE 20. Mean and turbulent particle-phase properties for the case II jet at $x/d = 40$

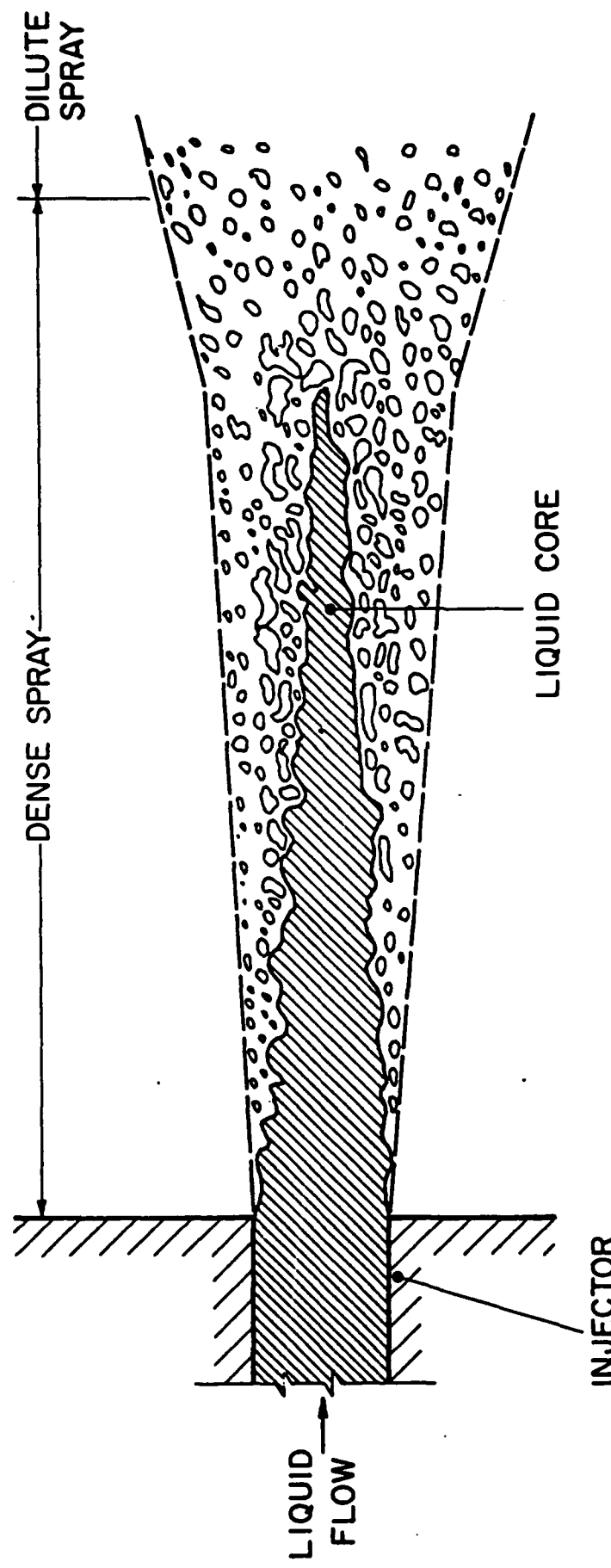


FIGURE 21. Sketch of near-injector region

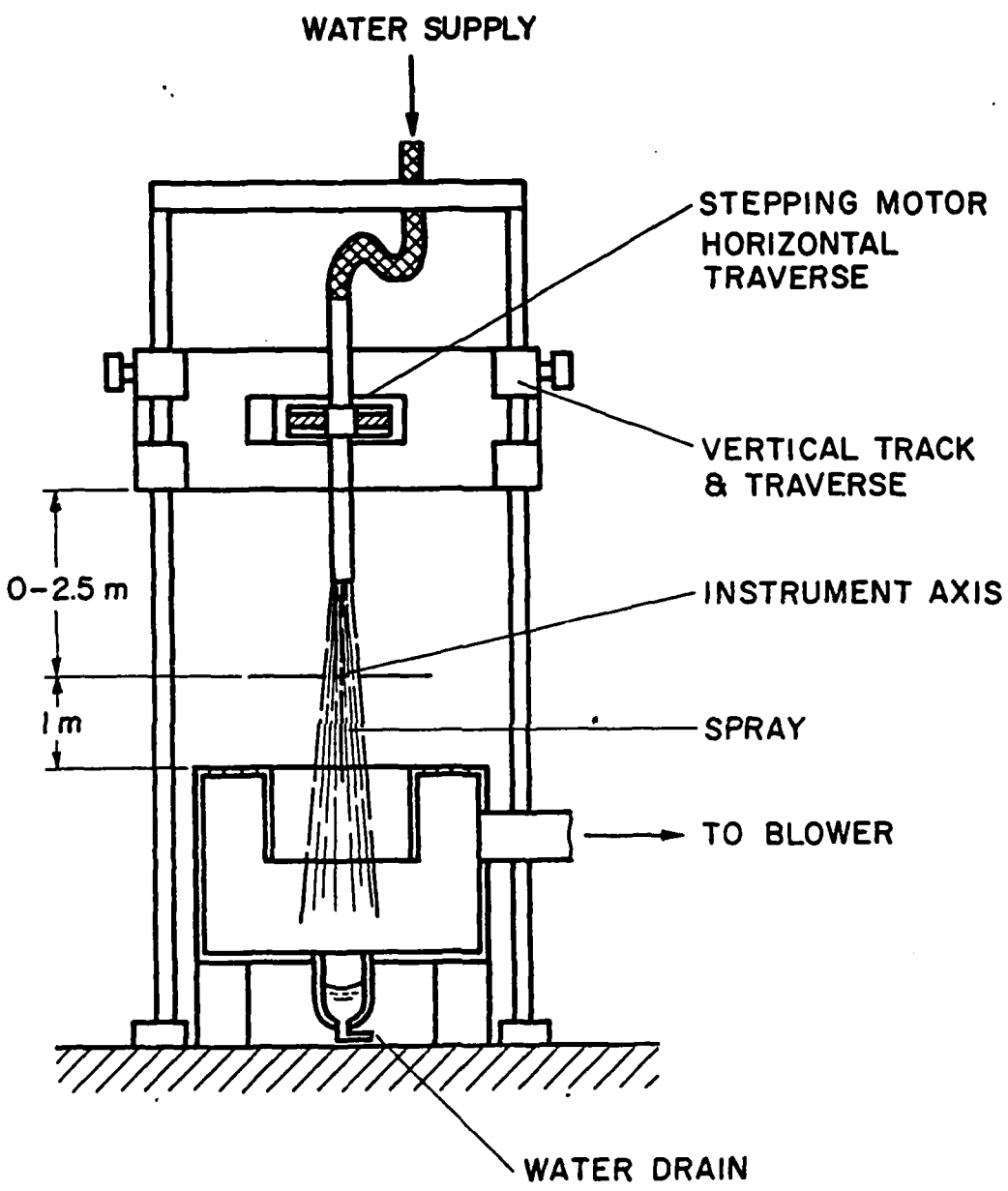


FIGURE 22. Sketch of dense-spray apparatus

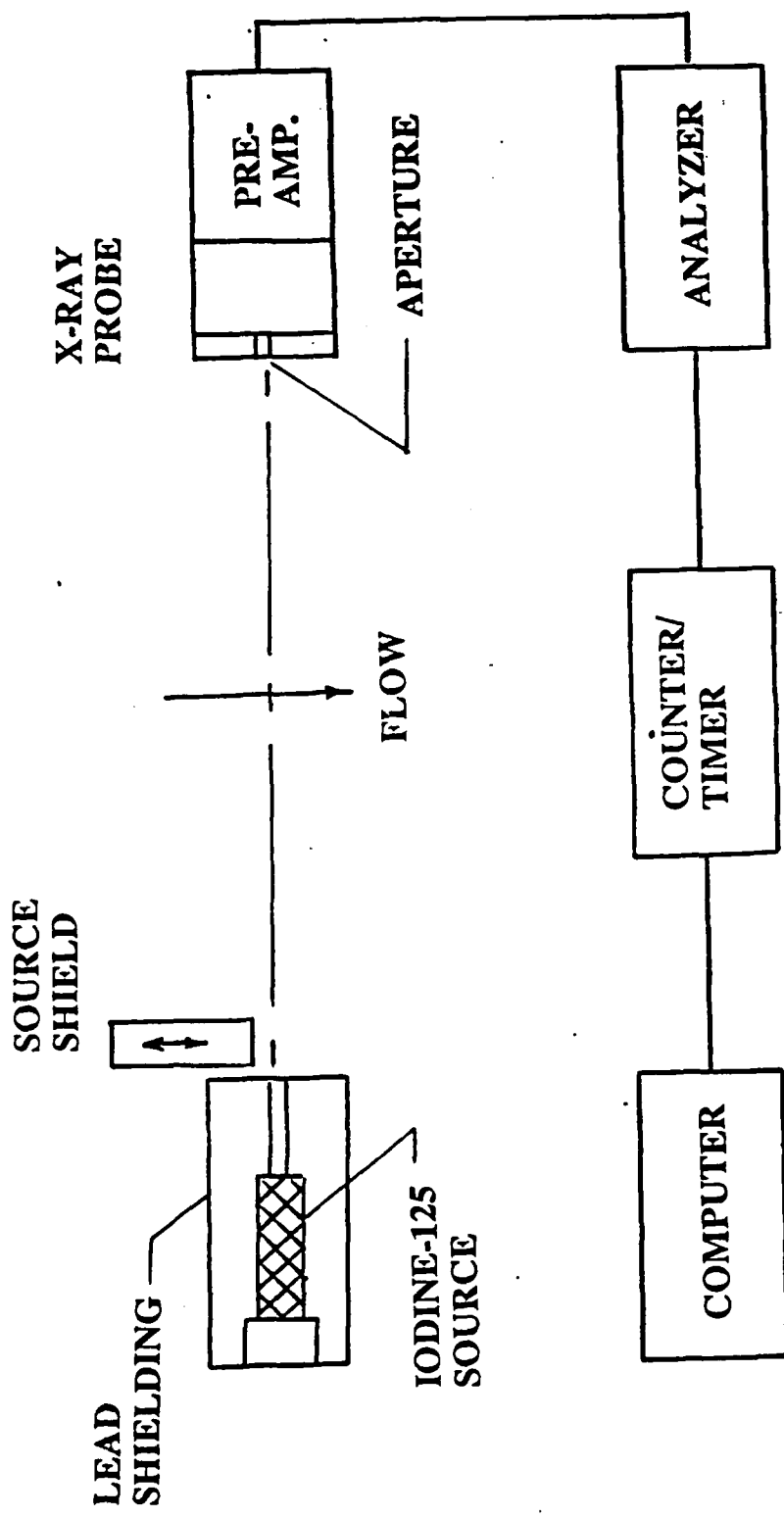


FIGURE 23. Sketch of gamma-ray absorption system

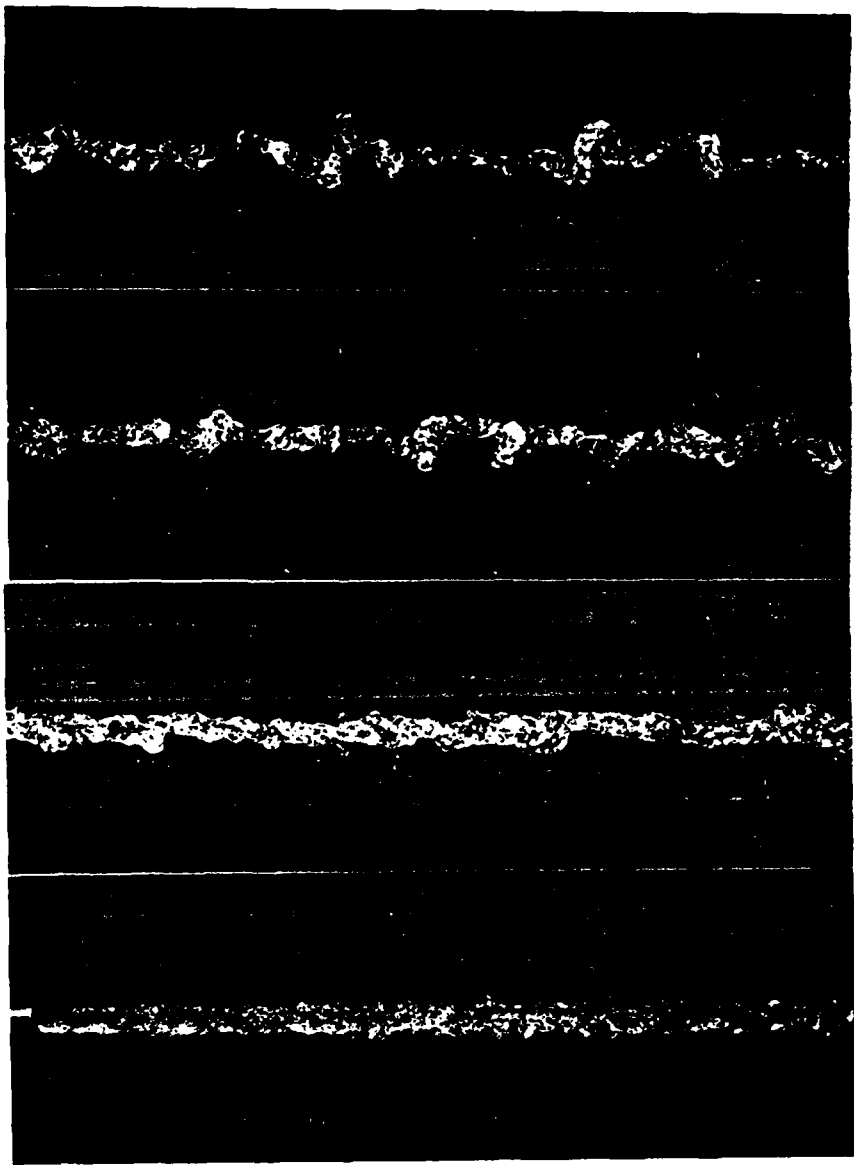


FIGURE 24. Flash photographs of the case I liquid jet

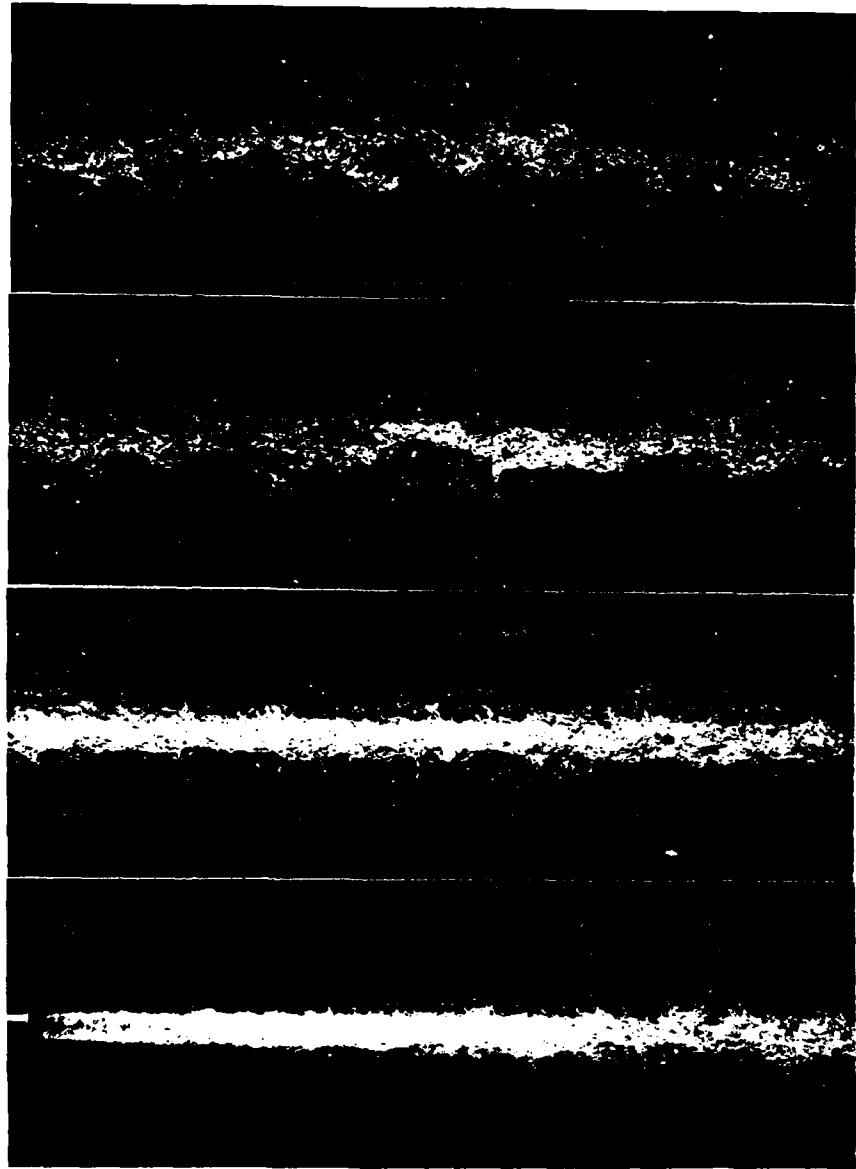


FIGURE 25. Flash photographs of the case 2 liquid jet

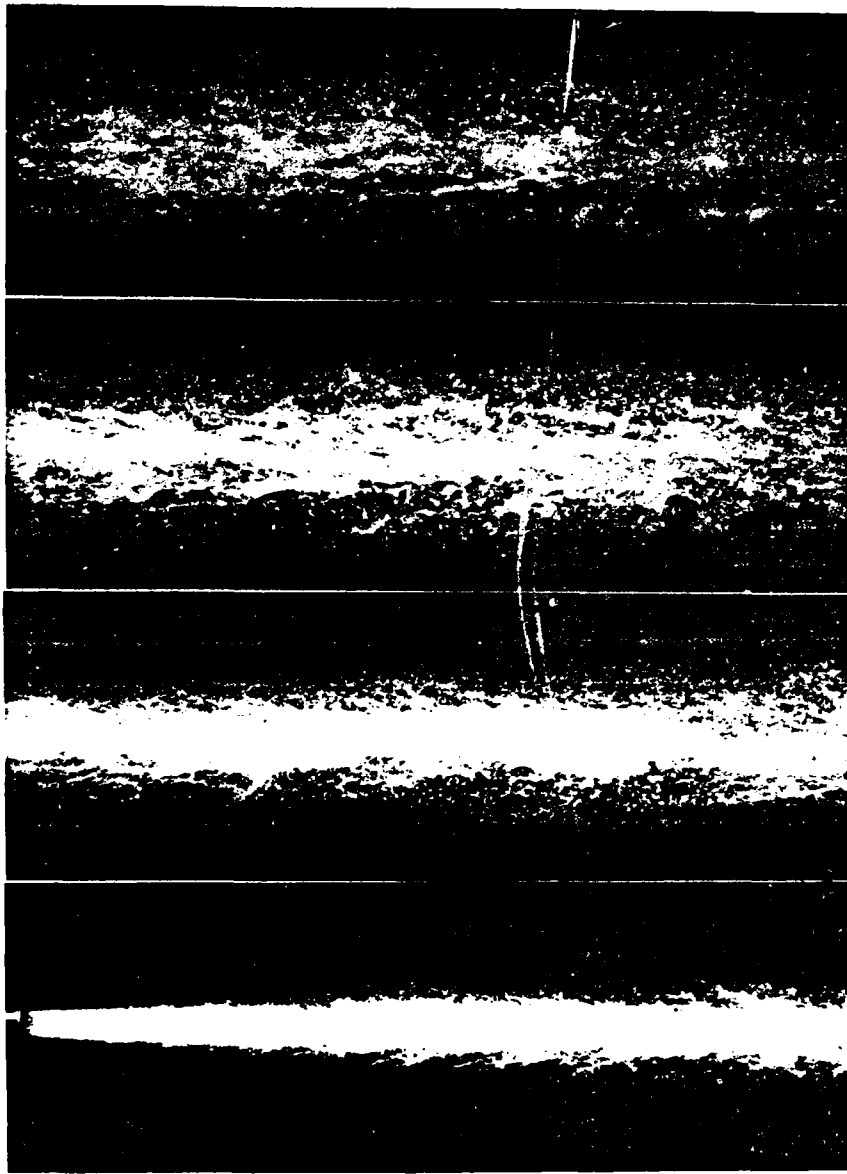


FIGURE 26. Flash photographs of the case 3 liquid jet

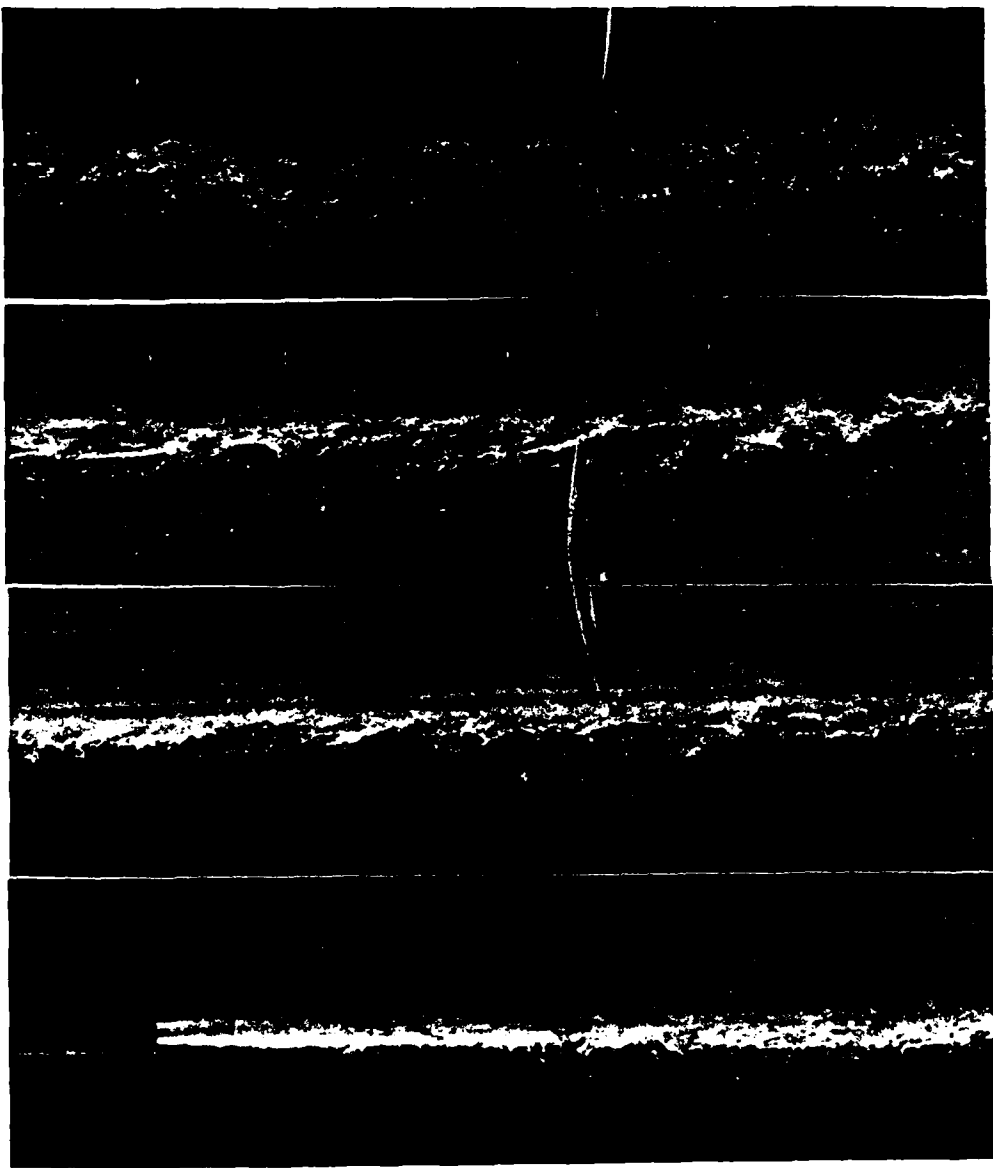


FIGURE 27. Light-sheet photographs of the case 3 liquid jet

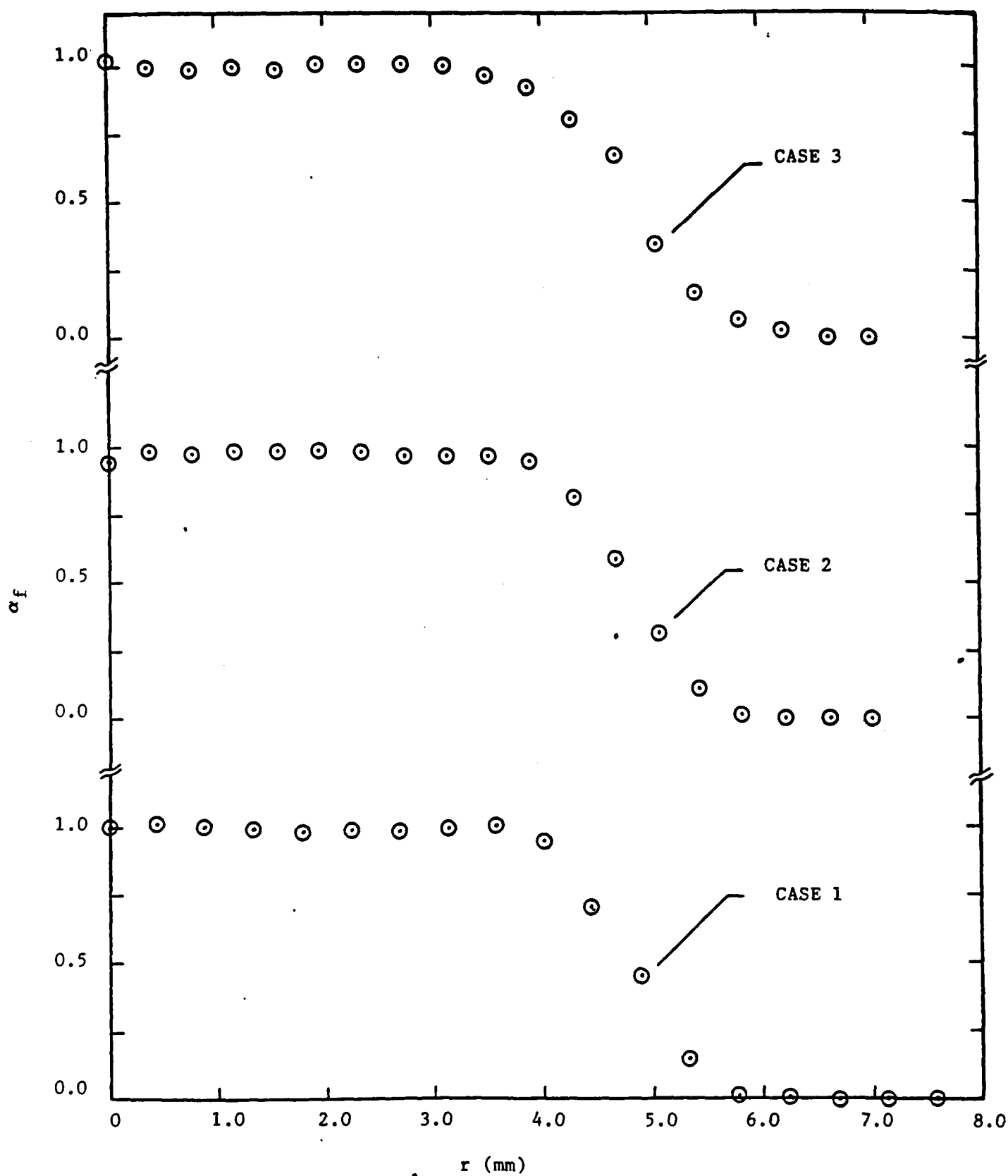


FIGURE 28. Mean liquid volume fractions at $x/d = 1$

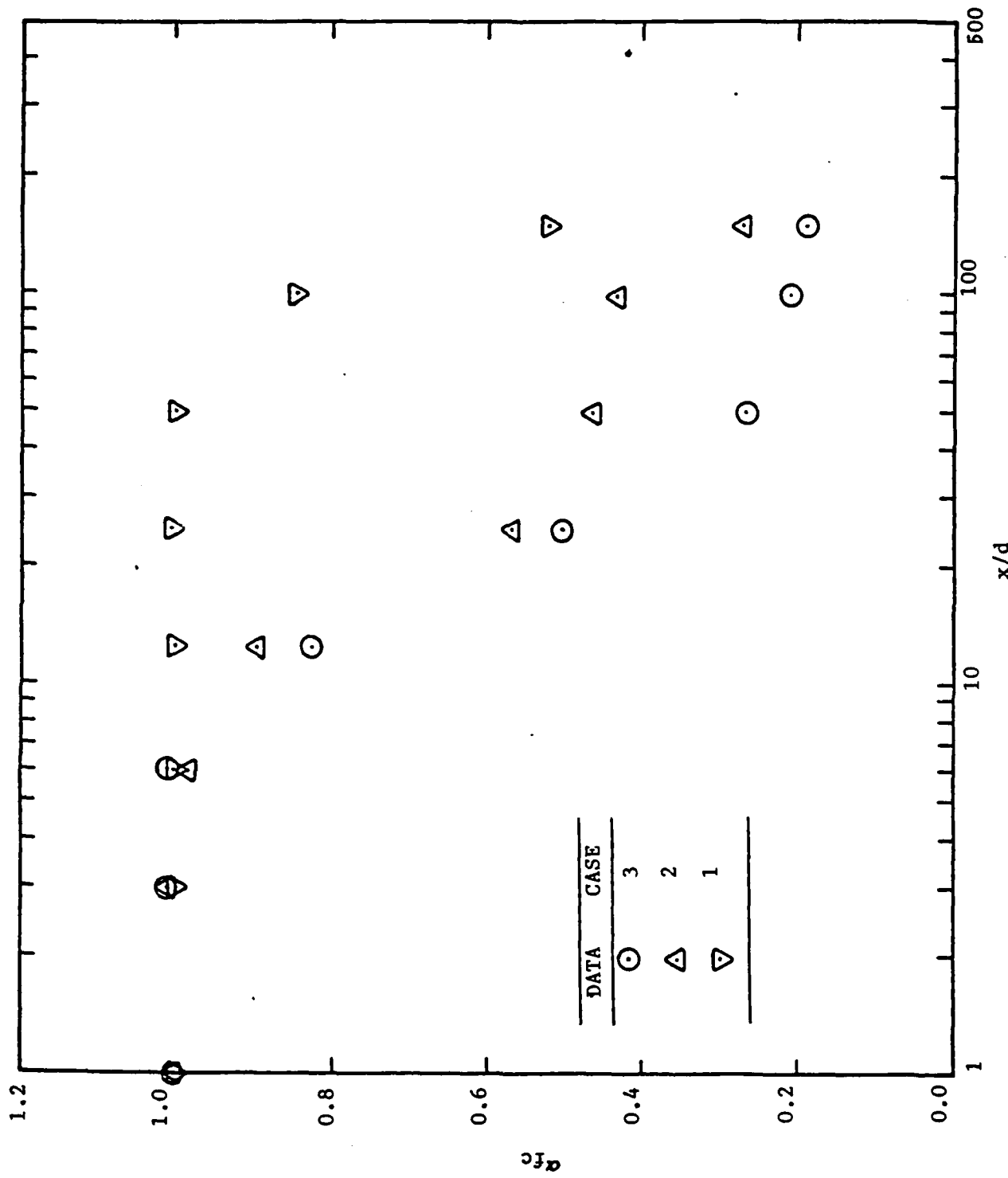


FIGURE 29. Mean liquid volume fractions along axis for the liquid jets

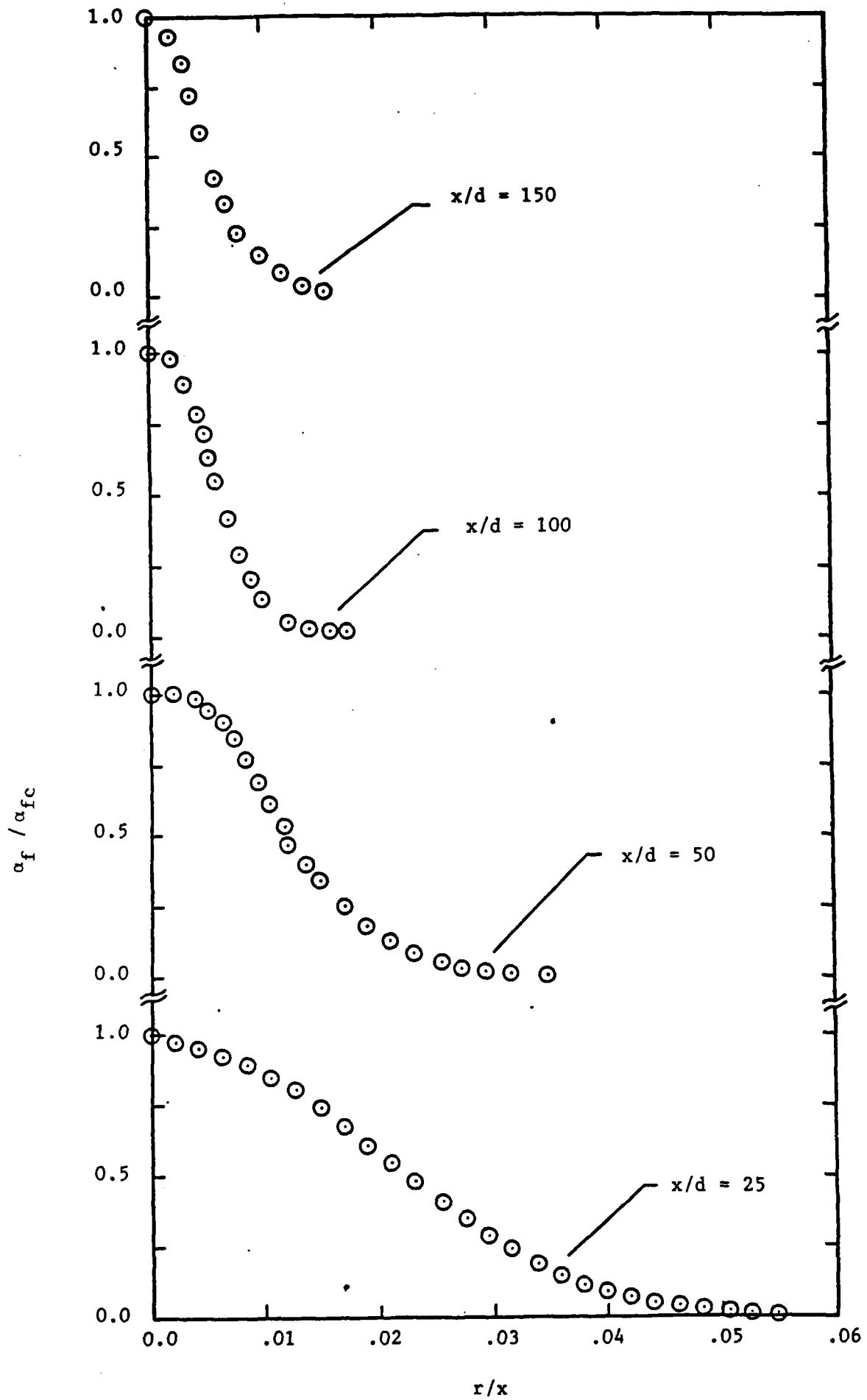


FIGURE 30. Mean liquid volume fractions for the case 2 liquid jet

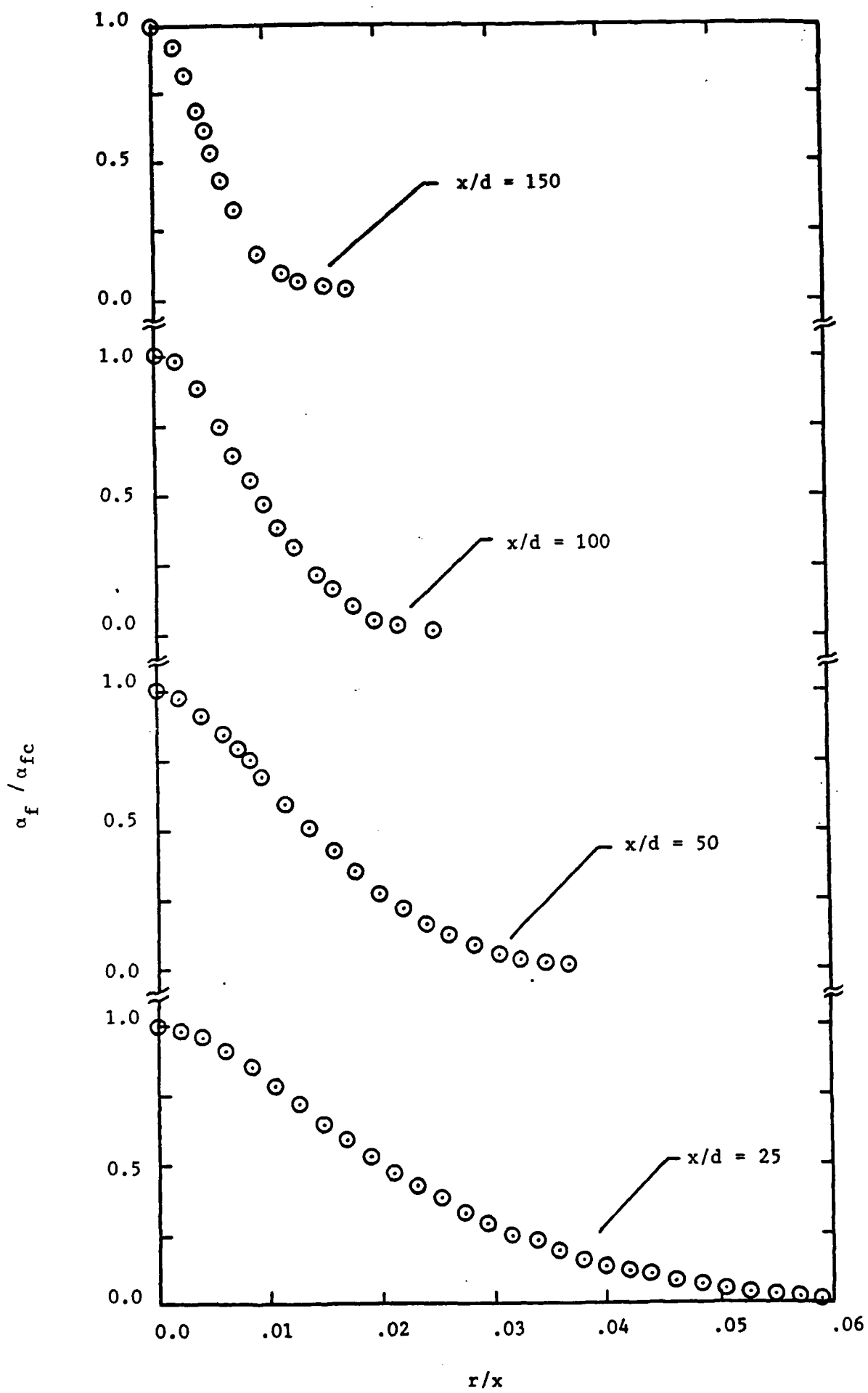


FIGURE 31. Mean liquid volume fractions for the case 3 liquid jet

END

— 87

DTIC